Electrochemical Energy Storage: Carbon Xerogel-Manganese Oxide Composites as Supercapacitor Electrode Materials

Dissertation zur Erlangung des
naturwissenschaftlichen Doktorgrades
der Julius-Maximilians-Universität Würzburg

vorgelegt von

Christian Weber

aus Würzburg

Würzburg 2015

Eingereicht am: 3. August 2015
bei der Fakultät für Physik und Astronomie

1. Gutachter: Prof. Dr. Jens Pflaum
2. Gutachter: Prof. Dr. Jean Geurts
der Dissertation

Vorsitzender: Prof. Dr. Randolf Hanke

1. Prüfer: Prof. Dr. Jens Pflaum
2. Prüfer: Prof. Dr. Jean Geurts
3. Prüfer: Prof. Dr. Wolfgang Kinzel
im Promotionskolloquium

Tag des Promotionskolloquiums: 19. Februar 2016

Doktorurkunde ausgehändigt am:

Abstract

Electrochemical double layer capacitors (EDLC), most commonly referred to as “supercapacitors”, have gained increasing scientific and commercial interest in recent years. Purely electrostatic charge storage processes allow charge- and discharge cycles in the second-time scale, exhibiting a theoretical capacitance in the order of 100 F per gram of electrode material, thereby providing efficient recuperation devices for electromechanical processes, for example. Introducing electrochemically active materials such as manganese oxides into the supercapacitor electrode, allows to combine the double-layer storage with a battery-like storage process, leading to capacitance that can be up to two orders of magnitude larger than those in EDLC.

In the present work, an electroless deposition approach of manganese oxide on a carbon scaffold is adapted and further investigated. The carbon material is derived from an organic xerogel, which in turn is prepared via a sol-gel process, allowing tailoring of the structural properties of the carbon, making it an ideal model system to study the relation between morphology and electrochemical performance in the carbon-manganese oxide hybrid electrode.

In the first part of this thesis, a variation of manganese oxide deposition time at a low concentration of precursor solution is analyzed. Mass uptakes reach up to 58 wt.%, leading to an increase of volumetric capacitance by a factor 5, however reducing the dynamic performance of the electrode. The structural characterization gives hints on the deposition location of the active material either in the intra-particular pores of the carbon backbone or on the enveloping surface area of the particles forming the backbone.

In order to comprehensively answer the question of the location of the active material within the hybrid electrode, the particle size of the carbon backbone and therefore the enveloping surface area of the carbon particles was varied. For samples with high mass uptakes, scanning electron microscopy (SEM) images show a layer thickness of 27 nm of active material around the carbon particles. In order to quantitatively investigate this layer morphology, even for low mass uptakes where no layer is visible in SEM images, a model interpreting data from anomalous small angle X-ray scattering (ASAXS) measurements was developed. The results confirm the presence of a layer around the carbon particles, exhibiting a layer thickness ranging from 3 to 26 nm.

From an electrochemical point of view, carbon backbones with a large enveloping surface area will lead to high mass uptakes in the electroless deposition process and therefore lead to high capacitance of the electrode. However, for future application, electrodeposition approaches should be investigated in detail, since no deposits will form on the interface between carbon backbone and current collector, leading to a better dynamic performance of the hybrid electrode. Furthermore, the ASAXS-method should be promoted and applied on other material systems, since this technique allows to draw important conclusions and allows to deduce integral and quantitative information towards a rational design of high performance electrodes.

Zusammenfassung

In den letzten Jahren haben elektrochemische Doppelschichtkondensatoren, meist als “Supercaps” bezeichnet, wachsendes wissenschaftliches und kommerzielles Interesse erfahren. Rein elektrostatische Ladungsspeicherungsprozesse erlauben Lade- und Entladezyklen im Sekundenregime, bei einer theoretischen Kapazität in der Größenordnung von 100 Farad pro Gramm Elektrodenmaterial. Damit steht beispielsweise ein ideales Bauteil zur Energierekuperation in elektromechanischen Prozessen zur Verfügung.

Die Verbindung der Doppelschichtelektrode mit elektrochemisch aktiven Materialien, wie zum Beispiel Manganoxiden, erlaubt eine Kombination der elektrostatischen Ladungsspeicherung mit batterieähnlichen Ladungsspeicherungsprozessen. Dies führt zu Kapazitätswerten, die bis zu zwei Größenordnungen über den Kapazitätswerten im Doppelschichtkondensator liegen können.

In der vorliegenden Arbeit wurde ein nasschemischer Abscheidungsprozess für die Deposition von Manganoxid auf einem Kohlenstoffgerüst angewendet und weitergehend untersucht. Das Kohlenstoffmaterial wurde aus einem organischem Xerogel hergestellt, welches wiederum durch einen Sol-Gel Prozess dargestellt wurde. Diese Vorgehensweise erlaubt eine gezielte Beeinflussung der strukturellen Eigenschaften des Kohlenstoffes. Dadurch wird das Material zum idealen Modellsystem, um den Einfluss der Morphologie auf die elektrochemischen Eigenschaften der Kohlenstoff-Manganoxid Hybridelektrode zu untersuchen.

Im ersten Teil der Arbeit wurde die Abscheidungsdauer des Manganoxids bei einer niedrigen Ausgangskonzentration in der Vorstufe systematisch variiert und die resultierenden Elektroden analysiert. Die MnO_2 Massenaufnahme erreichte bis zu 58 wt.%, was zu einer Steigerung der volumetrischen Kapazität um einen Faktor 5 führte. Der Preis für diese Steigerung liegt jedoch in einer Reduktion der Lade- bzw. Entladegeschwindigkeit. Die strukturelle Charakterisierung der Hybridelektroden deutet auf eine Abscheidung des MnO_2 in den intrapartikulären Poren der Kohlenstoffpartikel oder auf deren einhüllenden Oberfläche hin.

Um den Abscheidungsort des aktiven Materials innerhalb der Hybridelektrode eindeutig zu bestimmen, wurde die Größe der Kohlenstoffpartikel und damit die externe Oberfläche des Kohlenstoffgerüstes systematisch variiert. Aufnahmen mittels Rasterelektronenmikroskopie (REM) zeigen eine Schicht von MnO_2 um die Kohlenstoffpartikel mit einer Dicke von bis zu 27 nm für Proben mit Massenzuwächsen von bis zu 130 %.

Um die Schichtdicke auch für geringe Massenaufnahmen, bei denen im REM keine Schicht erkennbar ist, quantitativ untersuchen zu können, wurde ein Modell zur Analyse von anomaler Röntgenkleinwinkelstreuung (ASAXS) entwickelt. Die Ergebnisse bestätigen die Existenz einer Schicht um die Kohlenstoffpartikel, deren Dicke zwischen 3 und 26 nm liegt.

Aus elektrochemischer Sicht wird ein Kohlenstoffgerüst mit großer einhüllender Oberfläche zu einer großen Massenaufnahme im nasschemischen Abscheidungsprozess und damit zu hohen Kapazitätswerten führen. Für eine zukünftige Anwendung sollten jedoch auch elektrochemische Abscheidungsprozesse genau untersucht werden, da bei dieser Methode kein Material auf der Kontaktfläche zwischen Stromabnehmer und Elektrode abgeschieden wird. Dadurch ist eine Verbesserung der elektrochemischen Performance der Hybridelektrode zu erwarten. Weiterhin sollte die ASAXS-Methode weiterentwickelt und auf andere Materialsysteme angewendet werden, da diese Technik wichtige Schlüsse erlaubt, sowie die Bestimmung integraler und quantitativer Information, die zu gezieltem Design von hocheffizienten Elektroden führen wird.

Contents

Chapter 1

Introduction

Looking at the amount of CO_2 present in the atmosphere today, the year 2010 reports a CO_2 concentration in the atmosphere of about 390 ppmv (parts per million by volume) [1]. A glance at earth's history reveals that in the last 400000 years (about the time when today's Germany was still covered by glaciers, *homo sapiens* started to walk about 200000 years ago [2, 3]) the concentration of CO_2 alternated between about 180 and 280 ppmv, never exceeding 300 ppmv [1]. These ups and downs in CO_2 concentration were always accompanied by severe changes in the earth's surface temperature, leading to extension of glaciers in times of low concentration and extension of deserts when the CO_2 level was high. The anthropogenic increase of the atmospheric CO_2 concentration will lead to huge consequences in the near future, starting from climate refugees because of land loss due to rising sea levels or because of hunger due to severe droughts [4, 5]. Additionally, the number of climate fluctuation induced catastrophes such as flooding and severe storms might increase, leading to immense economic costs [6].

In his book "Sustainable Energy - without the hot air" David MacKay offers a consistent overview of current energy needs and supply in Great Britain and works out energy scenarios for sustainable supply [7]. He suggests three different ways to cut down CO_2 emissions:

1) less people
2) change lifestyle
3) higher efficiency

While alternative 1) is ethically and morally not feasible, the majority of people in so-called "developed" countries is not willing to change their lifestyle to a pre-industrial standard, which is what would be necessary to balance the CO_2 emissions. Moreover, the majority of mankind, living in the emerging countries, is currently trying to get out of this lifestyle. This only leaves alternative 3) as a possible scenario to cut down CO_2 emissions: make processes more energy efficient.

In 2011, Germany had a total primary energy consumption of 15409 PJ [8]. The primary energy uptake includes energy from coal, oil, gas, uranium; renewable energy sources account for 11.0 % [8]. Figure 1.1 shows the various contributions to the total primary energy consumption. As can be seen, transport accounts for 16.7 % of Germany's primary energy uptake, offering a huge potential for more energy efficiency.

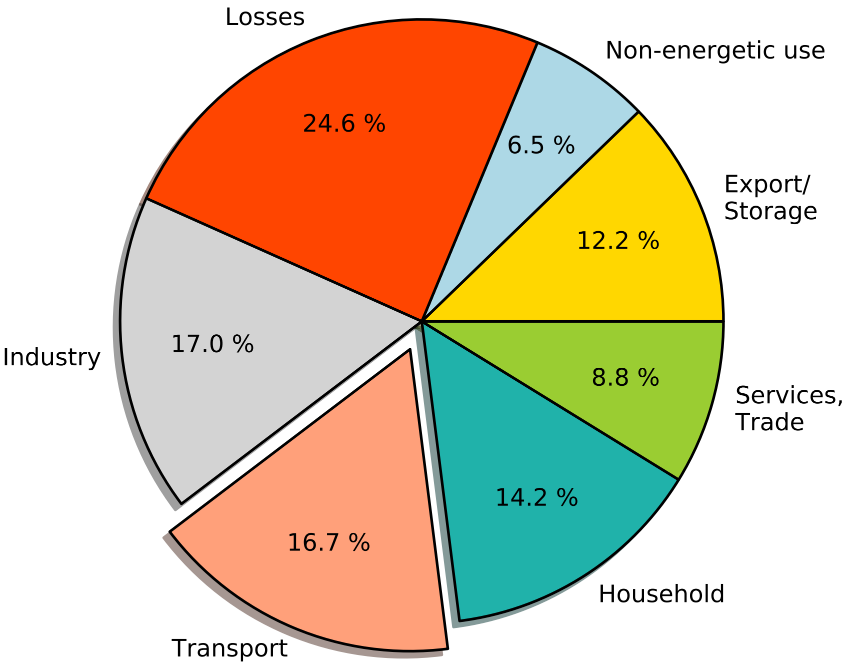

Figure 1.1: Contributions to primary energy consumption of Germany in 2011 [8]. Nearly one forth of the energy is lost in conversion processes (24.6 %). Transport accounts for 16.7 % of the energy consumption.

Electrochemical double layer capacitors (EDLC), widely known as "supercapacitors", have the potential to make electro-mechanical processes more energy efficient, by recuperating kinetic energy in form of electrical energy when motion is decelerated. EDLC use pure electrostatic storage processes, therefore exhibiting almost unlimited cycle life and require little maintenance in final applications.

The capacitance of a plate capacitor is defined as

$$C = \varepsilon \frac{A}{d}, \tag{1.1}$$

where ε is the permittivity, A the surface area of the plate and d the distance between the plates. As will be shown later in Chapter 2.1, the EDLC can be regarded as two plate capacitors in a serial configuration. Using high surface area carbons with specific surface areas up to 1000 m^2/g and aqueous electrolyte solutions, capacitances of 100 F per gram of electrode material can be commonly achieved. The energy stored in a capacitor is given by $W = \frac{1}{2}\, C \cdot E^2$, where E is the operating voltage. Commercial devices containing organic electrolytes reach mass specific energy densities of 5 Wh/kg at a voltage of 2.5 V [1].

Whereas supercapacitors are widely established as backup power sources in consumer electronics or for emergency power supply (e.g. the emergency door mechanism in the airplane "Airbus A380" [9]), transport applications are starting to emerge. For example, a reduction of about 30 % of the diesel consumption of a diesel-electric metro bus was achieved by MAN in their "Lion's City hybrid" bus [10]. A commercially available personal car that uses supercapacitors for energy recuperation is the "Mazda 6 i-Eloop" [11]. In these applications, the supercapacitor acts as fast chargeable, short term storage device, storing the electrical energy collected during the braking process for typically some seconds, before either returning it to the electrical motor for acceleration or slowly charging the battery. Recent advances by Volvo enable the integration of the devices in the chassis of the vehicle, thus allowing to reduce the overall weight of a car by more than 15 % [12].

In order to further increase the capacitance of a supercapacitor, battery-like storage mechanisms can be introduced. In contrast to the electrostatic storage mechanism in EDLC, these storage processes are dominated by faradaic reactions. The theoretical treatment of this charge storage process will be covered in Chapter 2.2. Devices of this type are often referred to as "pseudocapacitors" or "supercabattery", whilst common literature combines both, EDLC and pseudocapacitor, under the term "supercapacitor". The theoretical mass specific capacitance of typical pseudocapacitor materials reaches values of up to 1380 F/g (0.9 V, [13]) for manganese oxides or even 3560 F/g (0.45 V, [14]) for cobalt oxides.

The approach to a pseudocapacitor investigated in the framework of this thesis was developed by Fischer *et al.* [15, 16]. The idea is to create a synergetic device, combining double layer- and pseudocapacitive charge storage. The prerequisite is an electrically highly conductive, large surface area substrate, on which the electrochemically active material can be deposited. The porous backbone of a carbon xerogel provides excellent electronic conductivity and a huge surface area, both for manganese oxide deposition as well as for double layer charge storage (see Chapter 3.1.2). The electroless deposition process proposed by Fischer *et al.* promises big potential for the commercialization of the device, since the process is easily scalable. In their work, they infiltrated commercially available fiber reinforced carbon xerogel paper with manganese oxide and varied the deposition time, $NaMnO_4$ and pH concentration in the precursor solution. Deposition from neutral precursor solutions was reported to yield the best results, with gravimetric capacitances reaching up to 130 F/g for MnO_2 mass loadings of 57 %, normalized to the total electrode mass. The deposition process from neutral precursor solution was claimed to be self-limiting in nature. However, the question on the exact location of the manganese oxide deposits remained unclear. They noted that the neutral deposition approach renders manganese deposition to be homogeneous throughout the three-dimensional structure, however the question whether the manganese oxide is deposited in small micropores (< 1 nm [17], see also Figure 1.2) within the particles forming the carbon xerogel backbone, or rather on the enveloping surface area of the particles, remained elusive.

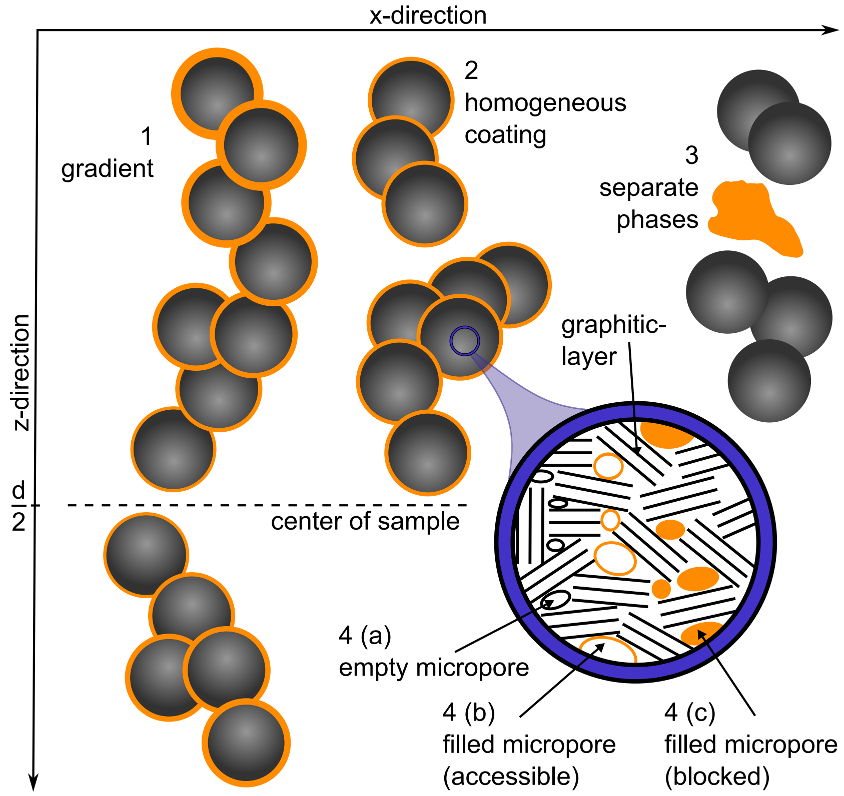

Figure 1.2: Schematic model of the possible deposition locations of MnO_2 and the resulting configuration of the hybrid structure.

A deposition of the active material in the micropores allows significantly higher mass uptakes than a deposition on the enveloping surface area. However, the active material must remain accessible for the electrolyte ions in order to increase the capacitance of the electrode. The main goal of this present work therefore is to locate the manganese deposits within the hybrid electrode structure prepared via the electroless deposition process. To reach this goal, a model system of resorcinol-formaldehyde derived carbon xerogels was investigated and tools to quantitatively characterize the system were developed and applied, motivated by the overall perspective that these techniques can be transferred also to similar material systems.

Possible scenarios for the location of MnO_2 in the carbon scaffold are depicted schematically in Figure 1.2. The black spheres represent the carbon xerogel particles, forming a porous network with meso- and macropores, with diameters ranging from 2 to 50 nm and diameters greater than 50 nm, respectively [17]. MnO_2 deposits may form mainly on the enveloping (external) surface area of the carbon xerogel particles, forming either a gradient in layer thickness towards the center of the sample (scenario 1) or a homogeneous coating (scenario 2). Also, separate phases of MnO_2 and carbon may be present in the system, as shown in scenario 3. Concerning the micropores of diameters smaller than 2 nm [17] within the carbon xerogel particles, three possible cases might occur: In case 4(a) they remain empty since pathways were blocked before manganese ions were able to reach the inner pores of the particle, but they might still be open for the electrolyte ions and thereby for double layer charge storage. The cases 4(b) and (c) depict the case of MnO_2 deposits in the micropores, being accessible for charge storage in case 4(b) (open pores, pore walls coated), or blocked (e.g. by complete filling) in case 4(c).

In the following, a theoretical background of the electrochemical charge storage processes involved in the model system under investigation is given, including a brief overview of current research approaches (Chapter 2). In the experimental part (Chapter 3) experimental methods are described, together with the respective theoretical background, sample preparation and data evaluation. Chapter 4 presents and discusses the influence of the manganese oxide deposition time on the structural and electrochemical characteristics of the electrode. The location of the deposit is investigated in more detail in Chapter 5 by applying a structural variation of the carbon scaffold. The results of this thesis are finally summarized in Chapter 6.

Chapter 2

Charge Storage in Supercapacitors

In an ideal capacitor, the amount of charges q that can be stored is directly proportional to the applied voltage E. The factor C that relates q and E is commonly referred to as the capacitance of the device [18]:

$$q = C \cdot E. \tag{2.1}$$

For electrochemical double layer capacitors (EDLC) and pseudocapacitance, as will be shown later in this chapter, the capacitance is a measure for the variation of the accumulated charge upon voltage change with time, i.e. the charging/discharging rate. Therefore, the definition of a differential capacitance C_{diff} is useful:

$$C_{\mathrm{diff}} = \mathrm{d}q/\mathrm{d}E. \tag{2.2}$$

This provides an immediate approach to measure C_{diff} by cyclic voltammetry, where the resulting current I at the electrode in response to a voltage change over time $\mathrm{d}E/\mathrm{d}t$ is measured (see also Chapter 3.3.2):

$$C_{\mathrm{diff}} = I/(\mathrm{d}E/\mathrm{d}t), \tag{2.3}$$

where I is defined by $\mathrm{d}q = I \cdot \mathrm{d}t$.

In real capacitors, contact-, bulk electrolyte- and electrode resistances have to be accounted for. It will be shown in Section 3.3.3 that equivalent circuit models can be developed, where the contributions of the individual resistances can be combined to an equivalent series resistance (ESR).

In this chapter, at first the purely electrostatical charge storage process in the electrochemical double layer will be introduced (Section 2.1). Allowing charge transfer across the double layer leads to the rise of so called “pseudocapacitance” under certain conditions. The prerequisites for the appearance of pseudocapacitance and potential materials to be used in supercapacitors are introduced in Section 2.2. Finally, the approach for combining double layer- and pseudocapacitive charge storage adapted in the scope of this thesis is presented in Section 2.3.

2.1 Electrochemical Double Layer

When the surface of an arbitrary solid state material (e.g. a metal or semiconductor) is brought into contact with an ionic solution, in general the chemical potentials of the material and the solution will be different. From a thermodynamic perspective, this is an unstable state and precipitation and dissolution will occur, until the respective chemical potentials are balanced. These reactions cause a potential difference, which in turn attracts ions from the electrolyte solution to balance the potential difference. Due to their hydration shell, ions from the electrolyte solution cannot cross the solid-electrolyte interface and are arranged in the so called “Helmholtz double layer” (see Figure 2.1). Applying an external voltage will increase or decrease the double layer thickness, depending on the amplitude and polarity of the local electrical field [19]. A condition for the validity of the electrochemical double layer models presented in the following is the purely electrostatic behavior of the system, i.e. no charge transfer across the double layer is allowed [20]. This is also referred to as the “non-faradaic” case.

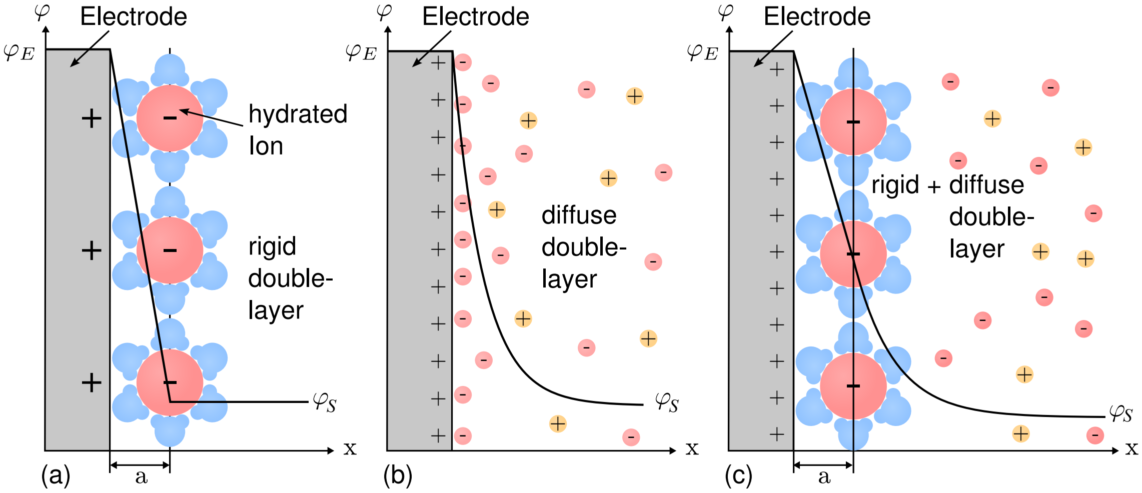

Figure 2.1: Double layer models according to von Helmholtz, Gouy and Chapman and Stern (left to right). The sketch is not to scale, the ions in the rigid double layer are enlarged to show the hydration shell. Figure adapted from [21].

An analytical treatment of the electrochemical double layer was first reported by von Helmholtz in 1853 [22]. His model assumes ions that are kept in a fixed distance a from the electrode surface A by their hydration shell (see Figure 2.1).

The Poisson-equation describes the related potential $\varphi(x)$ at a distance x from the electrode's surface and the related charge density $\rho(x)$ in the Helmholtz layer [19]:

$$\frac{\partial^2 \varphi(x)}{\partial x^2} = -\frac{\rho(x)}{\varepsilon_\mathrm{r}\varepsilon_0}, \qquad 0 \le x \le \infty. \tag{2.4}$$

Here, ε_0 is the dielectric permittivity of the vacuum and ε_r the relative permittivity of the Helmholtz layer, which can be combined to $\varepsilon = \varepsilon_r \varepsilon_0$. The equation can be integrated analytically, considering the space between the electrode surface and the Helmholtz layer in a distance $x = a$ from the surface to be free of charges, i.e. $\rho(x < a) = 0$, and taking into account the boundary conditions for the potential at the electrode $\varphi(0) = \varphi_\mathrm{E}$ and in the electrolyte solution at large distances x from the surface, φ_S (see Figure 2.1a):

$$\varphi(x) = \varphi_\mathrm{E} + \frac{x}{a}[\varphi_\mathrm{S} - \varphi_\mathrm{E}]. \tag{2.5}$$

This relationship corresponds to the potential of a plate capacitor with the capacitance

$$C = \varepsilon \frac{A}{a}. \tag{2.6}$$

However, the validity of the Helmholtz-model is limited because at finite temperatures, the thermal movement of ions has to be accounted for. Gouy introduced the thermal movement by assuming a spatially extended layer of point charges; the mathematical treatment was developed by Chapman, who described the thermal movement by introducing a Boltzmann type energy distribution [23, 24]. Yet, their model overestimates the electrochemical capacitance, since the point charges are allowed to come infinitesimally close to the electrode surface.

This was considered by the model of Stern in 1924, who combined the two theories and added a diffuse layer of finite size ions to a rigid, Langmuir-type (see Equation C.3) adsorbed layer of ions at the electrode's surface [25]. The total capacitance C of the electrochemical double layer finally is found to behave like a serial configuration of the capacitance C_HH of the rigid Helmholtz double layer and the capacitance C_di caused by the diffuse charge layer:

$$\frac{1}{C} = \frac{1}{C_\mathrm{HH}} + \frac{1}{C_\mathrm{di}}. \tag{2.7}$$

Therefore, the smaller contribution of either C_HH or C_di will dominate the overall capacitance.

For all pure double layer electrodes, the surface is considered to be electrochemically inactive and the double layer forms solely due to electrostatic interaction. In particular, no adsorption of electrolyte ions to or redox-reactions will take place at the electrode interface with the electrolyte, since by definition no current is allowed to pass through the double layer. The process therefore is called "non-faradaic" [21]. This is the case for an ideally polarizable electrode. In general, for real electrodes, a small leakage current has to be considered [20].

In recent years, more detailed theories to describe the electrochemical double layer have been developed, including e.g. field dependent orientation of solvent dipoles [26–28] and spatially varying electron-densities reaching from the electrode surface into the double layer because of the de-localized nature of the electron wave functions at the electrodes [29–31]. A comprehensive description of the double layer charge storage in porous carbon electrodes also includes the behavior of the ions in micropores [32–34]. For electrolyte solutions with high ion concentrations (i.e. $c >1$ M), as used for example in the cells investigated in this thesis, the electronic charge accumulating on the (microporous) electrode surface is immediately compensated by ions in the vicinity of the interface and a rigid layer of ions is formed, avoiding the need for compensation by a diffuse layer [21]. The double layer capacitance of carbon electrodes has been estimated of the order of 15-50 $\mu\mathrm{Fcm}^{-2}$, depending on the structure of the carbon surface and the size of the hydrated ions [35, 36].

2.2 Pseudocapacitance

The previously described models explicitly excluded the possibility for ions to cross the double layer and to react with the electrode surface. An utterly different type of charge storage mechanism arises if ions can pass through the double layer and an electrochemical charge-transfer process occurs. According to Faraday's laws, an electron transfer causes a change in the chemical or oxidation state of the electrochemically active material, hence these processes are called "faradaic" [21].

Eucken and Webulus [37] as well as Conway and Gileadi [38] used a thermodynamical approach to explain the rise of pseudocapacitance, which is summarized in Appendix C. They show that for typical electrochemically active materials, a quantity C_Φ can be derived from e.g. a fractional surface coverage Θ or the amount of active species reduced/oxidzed, if the charge transfer Δq is a function of applied potential E such that:

$$C_\Phi = q\frac{\mathrm{d}\Theta}{\mathrm{d}E} = \frac{\Delta q}{\Delta E}. \qquad (2.8)$$

This relationship, by definition (see Equation 2.2), has the form of a differential capacitance, since the transferred charge Δq depends linearly on the change of the applied voltage ΔE. Yet, due to its faradaic nature, the origin for this relationship is completely different from the electrostatic case and therefore it is historically referred to as "*pseudo*"-capacitance C_Φ [20, 21]. Similar to the double layer capacitance, the pseudocapacitance in general is voltage dependent, resulting in a broad current peak in the voltammogram. Peaks from several oxidation states, in combination with surface adsorption on the rough surface structure of the faradaic species, lead to an almost rectangular shape of the CV-diagram (see Figure 2.2).

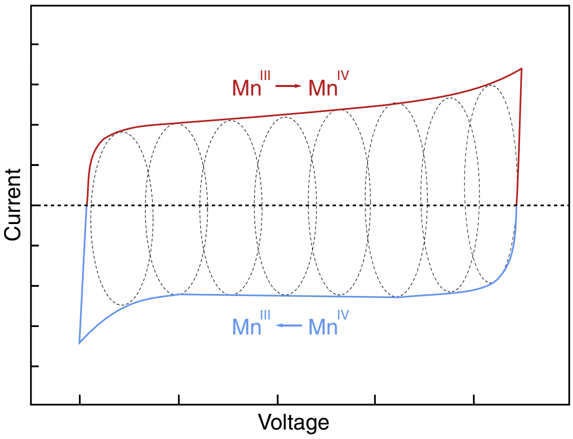

Figure 2.2: Cyclic voltammogram of MnO_2, showing the multiple successive overlapping redox processes forming the typical rectangular shape of the current response. Reproduced from [39].

Several types of faradaic active materials are known to provide a pseudocapacitance that is usable in supercapacitor electrodes, since their faradaic current is significantly extended over the applied voltage window (see also Appendix C): Redox reactions of carbon surface groups with ions from the electrolyte solution [40–42], doping and de-doping of polymers [43–45], redox reactions of transition metal oxides such as RuO_2, MnO_2, as well as oxides of Ni and Co [46–50]. On the huge surface area of nanoporous carbons, the redox reactions of quinone/hydroquinone surface groups have been identified as the main contribution to the pseudocapacitance [40, 51]. Polyaniline, polypyrrole and polythiophene are the most widely used conducting polymers as electrodes for electrochemical capacitors [52–54]. The polymers are either p- or n-doped, therefore they are exclusively applied as the positive (p-doped) or negative (n-doped) electrode. The resulting capacitor therefore is always regarded an asymmetric device, resulting in a higher operational voltage of up to 3.1 V in non-aqueous electrolyte solutions [50]. Ruthenium oxide has been thoroughly investigated in recent years (major publications are for example cited in Chapter 11 of [21]). The charge storage process was here identified to be mainly based on proton intercalation in RuO_2 bulk [21]. Specific capacitances of up to 900 F/g were reported [55]. However, its high toxicity and the high price prohibit the commercial use of RuO_2 in supercapacitors.

For a detailed overview of the abundant configurations of MnO_2 in electrochemical capacitors, the overviews provided by Bélanger *et al.* [56], Wang *et al.* [50] and Zhi *et al.* [57] are recommended. In the scope of this thesis, the focus is especially on the pseudocapacitive charge storage process in amorphous MnO_2 thin films deposited on microporous carbon.

The first report on MnO_2 as supercapacitor material was published by Lee and Goodenough in 1999 [46]. They reported a specific capacitance of 200 F g^{-1} for amorphous MnO_2 in mild alkaline aqueous solutions. The charge storage process was proposed to include cations C^+ being adsorbed at the oxide surface [56]:

$$(\mathrm{MnO_2})_{\mathrm{surface}} + \mathrm{C}^+ + e^- \leftrightharpoons (\mathrm{MnO_2} - \mathrm{C}^+)_{\mathrm{surface}}. \tag{2.9}$$

The charge storage process was further investigated by Pang and Anderson, who postulated proton insertion into the MnO_2 bulk, as well as the insertion of alkali cations [56, 58, 59]:

$$\mathrm{MnO_2} + \delta \mathrm{X}^+ + \delta e^- \leftrightharpoons \mathrm{MnOOX}_\delta, \tag{2.10}$$

where X represents the protons H^+ or the alkali metal cations C^+ and δ is the number of electrons involved. Structural water confined in the bulk of MnO_2 was found to limit the electrochemical performance of MnO_2 [60].

Intensive *in-situ* X-ray photoelectron spectroscopy (XPS) studies on the pseudocapacitance charging of amorphous MnO_2 were performed by Toupin *et al.* [13]. By measuring the Mn 3s core level spectra of MnO_2 in the oxidized and reduced state for MnO_2 film electrodes with film thicknesses ranging from 2 µm to 100 µm, they found that only a thin layer (< 2 µm) was electrochemically active (see Figure 2.3). Also, both alkali cations and protons were shown to take part in the charge storage mechanism, suggesting a reaction consistent with Equation 2.10.

In a study by Kuo *et al.*, crystalline MnO_2 was investigated via *in situ* X-ray absorption near edge structure (XANES) spectroscopy [61]. Together with *in situ* X-ray diffraction, monitoring a reversible expansion and shrinkage of the oxide lattice spacing (about 10 % [61]) upon cycling, they showed that cations are inserted into MnO_2 bulk. Via electrochemical quartz crystal microbalance (EQCM) measurements, they proved the redox reaction to be of one-step character, including cations and oxonium H_3O^+ ions. The proposed charge storage reaction therefore reads:

$$\begin{aligned} &\mathrm{Mn(IV)O_2} \cdot n\mathrm{H_2O} + \delta e^- + \delta(1-f)\mathrm{H_3O}^+ + \delta f \mathrm{C}^+ \leftrightharpoons \\ &\leftrightharpoons (\mathrm{H_3O})_{\delta(1-f)} C_{\delta f} [\mathrm{Mn(III)}_\delta \mathrm{Mn(IV)}_{1-\delta}]\mathrm{O_2} \cdot n\mathrm{H_2O}, \end{aligned} \tag{2.11}$$

where f is the molar fraction of cations involved.

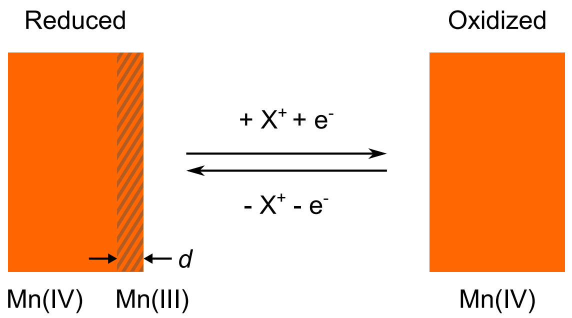

Figure 2.3: Schematic sketch of Mn-reaction processes involving only a thin surface layer ($d < 2$ μm). X^+ represents either protons or alkali ions. Reproduced from [56].

In a recent review by Zhi *et al.*, the pseudocapacitance of MnO_2 is identified to originate from redox centers of weakly attached surface ions, such as surface functional groups or defects, and grain boundaries in the crystal structure of MnO_2 [57].

The different conclusions deduced from these investigations show that the complex mechanisms of charge storage in MnO_2 are not completely understood yet and will require further investigation. However, strong hints for a dominating contribution by surface effects to the faradaic charge storage are found in the majority of publications.

2.3 Hybrid Systems

Before describing the electrode design approach chosen in this thesis, an overview over common material combinations of manganese oxides as supercapacitor materials will be given.

So called "hybrid systems" in electrochemical charge storage aim to combine double layer- and pseudocapacitance charge storage. Many different routes to achieve such a combined system have been investigated in recent years, including many of the pseudoactive materials mentioned in Section 2.2. The approaches can be divided into two major groups:

1) Asymmetric systems, which consist of one battery-type electrode and a carbon double layer electrode , e.g. (amorphous or (poly)crystalline) powder-MnO_2 and activated carbon, respectively [62–64]. Thin film MnO_2 electrodes are produced via sol-gel dip-coating [58, 65] or electrodeposition [66, 67].

2) Symmetric devices, where the active material is present in both electrodes. Symmetric devices usually combine double layer and pseudocapacitive charge storage in each electrode, the capacitance contributions adding up as parallel configuration. High surface area is a fundamental

prerequisite for reaching high double layer capacitances. Simple approaches therefore include mixing of ground MnO_2 powder and carbon black as a conductive agent [68]. The combination of graphene [69, 70], carbon fibers [71] and carbon nanotubes (CNT) [72, 73] with MnO_2 were investigated in detail. A lot of effort was spent on nanostructuring MnO_2 in order to achieve better overall electrical conductivity, material efficiency and higher surface area. However, complex morphologies of MnO_2 tend to be thermodynamically unstable and collapse upon cycling [74].

From the various potentially electrochemical active metal oxides, MnO_2 is the most promising one, due to its low toxicity and natural abundance, even though called "rare earth material" [56]. Manganese oxide occurs in various oxidation states, crystal structures (see Figure 2.4) and morphologies, all influencing its electrochemical properties, such as the ionic- and electronic conductivity [75]. In accordance with literature and for simplicity, in the scope of this thesis, manganese oxide is referred to as MnO_2, regardless of the exact oxidation state, unless explicitly stated otherwise.

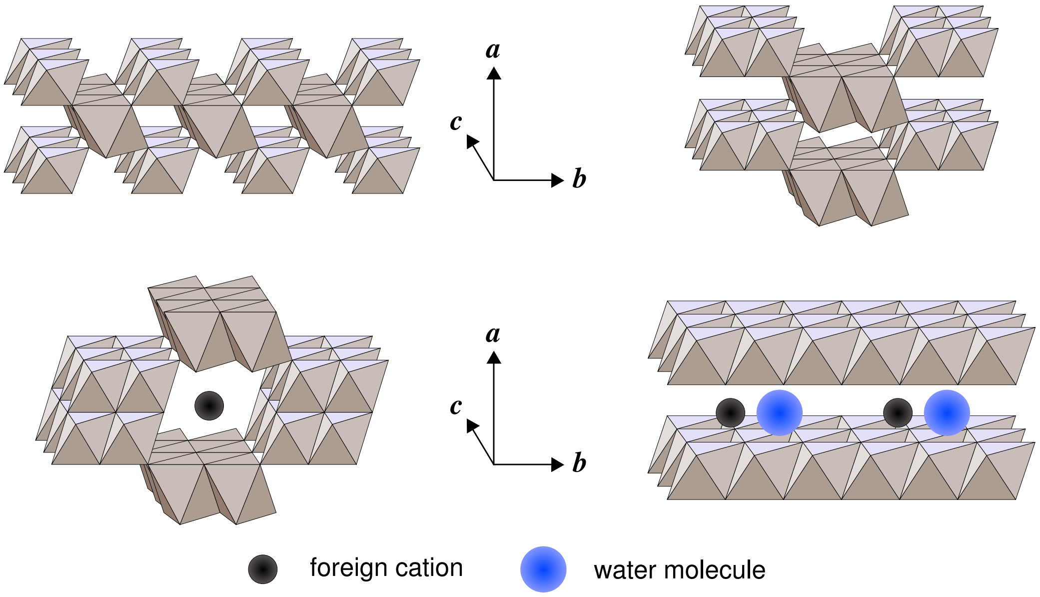

Figure 2.4: Typical crystal structures of MnO_2 with the crystallographic axes. The structures are referred to pyrolusite (β-MnO_2, 1x1), ramsdellite (γ-MnO_2 1x2), hollandite (α-MnO_2, 2x2) and birnessite (δ-MnO_2, 1x∞) in clockwise arrangement, starting at the upper left corner [76].

The idea behind this work is to overcome the drawbacks of bulk MnO_2 such as its low electrical conductivity (typically 10^{-5} to 10^{-6} Scm^{-1} [16]) and low cyclability due to irreversible effects triggered by mechanical stress induced by ion insertion into the volume. Depositing a thin layer of MnO_2 on a well conducting three dimensional scaffold is considered as a possible strategy to overcome these drawbacks.

The preparational approach chosen in this thesis is based on the method described by Fischer *et al.* [15, 16], where MnO_2 is wet-chemically deposited on the large surface area of a carbon xerogel. This special kind of open porous carbon is utilized to provide a maximum surface area for deposition of the active material, while additionally contributing to the double layer capacitance [77]. Due to the layered contact between carbon and MnO_2, the contact resistance that usually arises, e.g. in blended compositions, is minimized.

The carbon xerogel derived by pyrolysis of a resorcinol-formaldehyde organic precursor offers the opportunity to modify the pore and particle structure of the carbon scaffold over a wide range, since the structural parameters can easily be tuned by varying the parameters of the sol-gel transition of the precursor [78]. For example, the target density of the xerogel can be adjusted via the concentration of resorcinol and formaldehyde in the initial solution. The amount of catalyst (Na_2CO_3) in the solvent (water) controls the average size of the particles forming the scaffold. For more details on the preparation of the xerogel, see Section 3.1.1.

The huge surface area of up to 2000 m^2/g [21] generated by micropores with sub-nanometer width ensures a substantial contribution of double layer storage [17]. Additionally, the well interconnected, 3-dimensional networks of meso- and macropores, with diameters ranging from 2 to 50 nm and diameters greater than 50 nm, respectively, provide excellent ion reservoirs and pathways for ion migration [79]. Furthermore, the surface area of the carbon xerogel can easily be decorated with MnO_2 (see Section 3.1.2). Therefore, the chosen hybrid system is an ideal model system to investigate hybrid electrodes composed of carbon and MnO_2.

In this thesis, the approach by Fischer *et al.* is adapted and refined, especially the question where the MnO_2 is deposited within the carbon structure is addressed in detail. Additionally to the systematic variation of the deposition time, a systematic modification of the structure of the carbon backbone was conducted. The microscopic mechanisms determining the deposition process of MnO_2 on the carbon surface will be presented in Section 3.1.2.

Chapter 3

Experimental

In the following chapter, the experimental methods applied and the sample preparation will be described. Theoretical background of the experimental techniques will be given in detail whenever it is necessary for an understanding of the evaluation of the experimental data.

Structural characterization methods include scanning electron microscopy (SEM) to directly probe the microscopic morphology of the sample. The porous structure of the carbon xerogel, on a length scale below 100 nm, is characterized via N_2 gas sorption measurements that allow to quantify the pore structure of the sample and of the (microscopic) surface area. In order to probe the chemical state of the electrode surface, photoelectron spectroscopy (XPS) measurements were performed. Anomalous small angle X-ray scattering (ASAXS) was used to integrally probe the structure of the carbon-manganese oxide ($CMnO_2$) hybrid electrode. Figure 3.1 gives an overview over the energy range involved in the different characterization techniques and their respective spatial resolution or accessible length scale.

The electrochemical methods applied include cyclic voltammetry (CV) for estimating the capacitance and kinetic behavior of the electrode, as well as electrochemical impedance spectroscopy (EIS) to investigate the frequency behavior and thus e.g. the charge transfer resistance of the electrode.

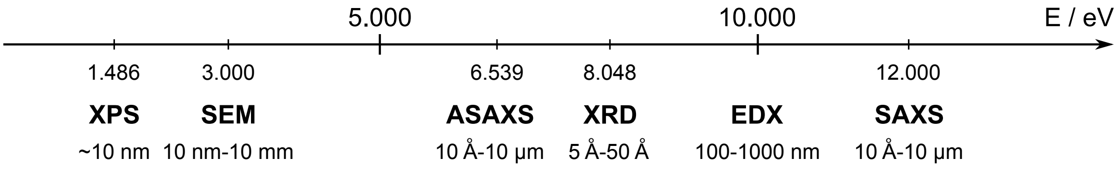

Figure 3.1: Energy ranges for different probing methods applied in this thesis. The lower line gives an estimation for the spatial resolution (SEM, EDX) or the accessible length scale (XPS, (A)SAXS, XRD).

3.1 Sample Preparation

3.1.1 Carbon Xerogel

As already described in the introduction, due to their tuneable pore characteristics, carbon xerogels constitute ideal model systems for investigating electrochemical energy storage devices. Carbon xerogels are prepared via pyrolysis of organic xerogels, that can originate from the sol-gel processes of phenol-formaldehyde [80] or melanin-formaldehyde [81] that have been dried at ambient pressure. The approach chosen in this thesis was the resorcinol-formaldehyde gel, firstly described by Pekala *et al.* [78, 82], a process that was later further developed by Saliger *et al.* [83] and Wiener *et al.* [84].

Two types of carbon xerogels were produced: sheets of carbon fiber reinforced "carbon paper" and monolithic samples. The carbon paper electrodes were used for electrochemical measurements, since they provide higher mechanical stability in case of thin (< 0.3 mm) electrodes. For ASAXS measurements, monolithic samples were applied, in order to avoid parasitic intensity contributions of the carbon fibers.

Figure 3.2 shows a schematic representation of the synthesis steps involved in the preparation of the carbon xerogels. In the first step, resorcinol is dissolved in an aqueous solution of formaldehyde (37 wt.%) at a molar ratio of 1:2. The target density of the resulting gel is adjusted by the mass ratio of resorcinol and formaldehyde with respect to the solvent. Within the framework of this thesis, water was added to reach the mass ratios listed in Table 3.1. The solution was stirred for 30 min at room temperature to ensure complete dissolution of resorcinol.

The size of the "primary" particles forming the gel can be influenced by the molar ratio of catalyst ($NaCO_3$, 0.01 M) to resorcinol. The catalyst provides nucleation centers for the growth of polymer chains. Therefore, the density of nucleation sites controls the amount of particles being built and finally influences the mean particle size. The molar ratios adjusted to obtain different

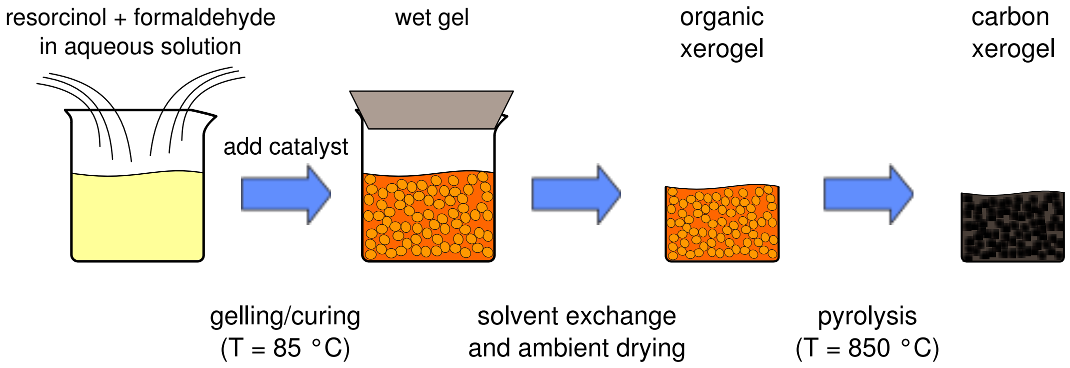

Figure 3.2: Schematic representation of the carbon xerogel synthesis.

particle sizes are given in Table 3.1. In order to produce monolithic samples, the solution was poured into glass vials and sealed airtight. For fiber reinforced carbon xerogels, carbon fiber cloth (SIGRATEX SPL-7011) was placed on glass plates and soaked with the solution, a second plate was placed on top and the package was sealed airtight with cling wrap and duct tape. For gelling, the solution was placed in an oven at 85 °C for 24 h. Next, the samples were allowed to cool down to room temperature and the gel was removed from the glass and immersed into ethanol for solvent exchange. Afterwards, the samples were dried for several days at room temperature and ambient pressure. The conversion to carbon was performed via pyrolysis in argon atmosphere for one hour at a maximum temperature of 850 °C. Directly after pyrolysis, the mass of the carbon xerogel and the samples geometric quantities were determined, in order to evaluate the sample density ρ. The porosity Φ was calculated relating the sample porosity to the carbon bulk density of nonporous carbon $\rho_{\mathrm{C}} = 2.2 \ \mathrm{cm}^3\mathrm{g}^{-1}$ [40]:

$$\Phi = 1 - \frac{\rho}{\rho_{\mathrm{C}}}. \tag{3.1}$$

The respective values for ρ and Φ are summarized in Table 3.1.

Table 3.1: Overview of the preparation parameters of the different carbon xerogel series: C T denotes the series used for the study of deposition times, C EC/G S,M,L and C S,M,L denote the series prepared to provide a particle size variation for electrochemical, gas sorption and X-ray investigations, respectively.

C-series	mass ratio / %	R:C molar ratio	type	ρ / cm^3g^{-1}	Φ / %
C T	30	1500	fiber reinforced	0.31±0.3	86
C EC/G S	28	500	fiber reinforced	0.37±0.4	83
C EC/G M	28	3000	fiber reinforced	0.29±0.3	87
C EC/G L	28	8000	fiber reinforced	0.26±0.3	88
C S	35	3000	monolith	0.53±0.5	76
C M	35	4000	monolith	0.49±0.5	78
C L	35	6000	monolith	0.43±0.4	80

3.1.2 Deposition of MnO_2

Various preparation routes for the deposition of MnO_2 on carbon can be found in literature. Studies by Hibinio *et al.* investigated acetylene black in acetic solutions of $NaMnO_4$ [85, 86]. They claimed ethanol to be involved reducing MnO_4^- to MnO_2 on the carbon surface. A similar composite was prepared by Kawaoka *et al.*, using a sonication method [87, 88]. The effect of sonication, however, was only weakly consolidated by experimental evidence. Graphite electrodes dipped in $KMnO_4$ dissolved in H_2SO_4 were investigated by Wu *et al.* [89]. Their explanation for the reduction mechanism involved CO_2 gas evolution. Fischer *et al.* reported a simpler approach by dipping carbon xerogels in neutral aqueous solutions of $NaMnO_4$, however, they commented only little on the deposition mechanism [15, 16]. Nevertheless, because of the reasonable electrochemical characteristics of the resulting electrodes, the approach of Fischer *et al.* was adapted in the framework of the present study.

The deposition process of MnO_2 on a carbon surface was investigated in detail by Ma *et al.* [90]. A short summary of their findings will be given in the following paragraphs.

In their study, the authors monitored the pH variation of an aqueous solution of 0.01 M $KMnO_4$ when adding acetylene black. Simultaneously, the reduction potential of the solution was recorded. An overview of the involved reaction steps is depicted in Figure 3.3. The process was divided into four stages:

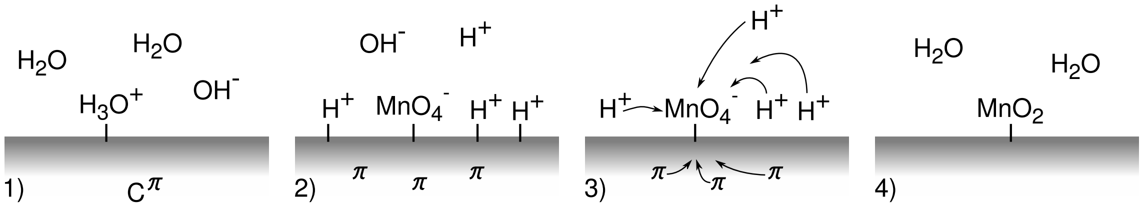

Figure 3.3: Schematic overview of the MnO_2 deposition reaction process from aqueous MnO_4^- solution on the carbon surface (gray bar).

In the first stage, when adding the acetylene black to the aqueous solution, a sharp increase in pH occurs (i.e. OH^- enhancement in the solution). This can be explained by delocalized π-electrons on the carbon surface acting as a Lewis base and adsorbing protons on the carbon surface, forming a complex according to (see also Figure 3.3) [40, 91, 92]:

$$C^\pi + 2H_2O \longrightarrow C^\pi H_3O^+ + OH^-. \tag{3.2}$$

Simultaneously, a sharp decrease in the reduction potential is recorded.

In the second stage, the pH slowly decreases, whereas the reduction potential stays constant. As depicted in Figure 3.3 2), this decrease in pH originates from the adsorption of MnO_4^- on the carbon surface while a proton is released.

The reduction of MnO_4^- to MnO_2 occurs in the third stage, following the reaction:

$$MnO_4^- + 4H^+ + 3e^- \longrightarrow MnO_2 + 2H_2O. \tag{3.3}$$

When all MnO_4^- is consumed in the fourth stage, the reaction ceases.

The reaction (Equation 3.3) preferably takes place at the carbon surface, where adsorbed protons and electrons are available (see Figure 3.3, 3)). This inherently implies a "self-limiting" nature of the deposition process, as mentioned by Fischer *et al.*, since the surface becomes passivated when all H^+, that was adsorbed in the first stage, is consumed [15].

It has to be stressed that in the mechanism proposed by Ma *et al.*, no consumption of carbon is involved in the reduction from MnO_4^- to MnO_2. Furthermore, neither deposition time, nor precursor temperature, nor the amount of carbon added to the solution showed an influence on the *structure* of the resulting MnO_2. The time for complete reduction of MnO_4^-, however, was influenced by temperature and relative amount of carbon in the solution [90]. Therefore, for the deposition on carbon xerogels, equal relative amounts of carbon and a constant process temperature (T = 20 °C) were chosen.

The respective preparation steps were conducted as follows:
The carbon xerogel was immersed into an aqueous solution of 0.05 M Na_2SO_4 and placed under mild vacuum of about 60 mbar for 30 min to ensure removal of residual gas and thus complete wetting of the xerogel pores. Subsequently, the solution was exchanged for a mixture of equal volumetric amounts of aqueous 0.1 M Na_2SO_4 and 0.1 M $NaMnO_4$ solutions at a total volume of 100 ml. The deposition time on fiber reinforced carbon xerogel samples was varied between 1, 4, 10, 16 and 24 h for the series CMnT and was kept constant for 4 h for the series CMn S,M,L (see Table 3.1 and tables in Appendix B). For the X-ray scattering experiments, monolithic carbon xerogels were cut into 0.5 mm thick discs and subsequently infiltrated for 4, 16, 24, 30 and 48 h. After deposition, the samples were washed several times with deionized water until the rinse was clear. Subsequently, the samples were dried in air at 45°C for 24 h and the total mass m_1 of the electrode after deposition was determined via weighting.

The total relative mass uptake Δm_i was determined by:

$$\Delta m_i[wt.\%] := 100 \cdot \frac{m_{MnO_2}}{m_i}, \tag{3.4}$$

where $m_{MnO_2} = m_1 - m_C$ is the mass deposited and m_C is the mass of the carbon electrode prior to deposition. The index i refers to the two possible ways to normalize the mass uptake: the normalization Δm_1 to the total mass of the electrode m_1, which is used for electrochemical analysis, and the normalization Δm_{C} to the mass of carbon in the electrode, i.e. the mass m_{C} of the electrode prior to deposition. The differences that arise from applying these two methods of normalization will be discussed in Section 4.1.1. For structural methods, the normalization to m_{C} will be applied, whereas, in accordance to literature, for electrochemical analysis, the data will be normalized to m_1, unless explicitly stated otherwise.

3.2 Structural Characterization Methods

3.2.1 Scanning Electron Microscopy

The scanning electron microscope (SEM) uses a highly focused electron beam to scan the surface of the sample under investigation, causing the emission of secondary electrons. The detection of secondary electrons allows to probe a depth of 5-50 nm below the sample surface and to reconstruct a representation of the surface structure with a high depth of field, allowing a three dimensional impression [93–95]. Additionally, back scattered electrons can be detected energy selectively using the energy selective backscattering detector (ESB). Due to inelastic scattering, the energy of the back scattered electrons is a measure for the momentum transfer to the scattering atom and therefore is related to the atomic number. Heavier elements cause less momentum transfer, so that the back scattered electrons have a higher kinetic energy and appear brighter in the resulting image. The contrast allows to distinguish between different chemical components in the material, with a spatial resolution on the order of some nanometers.

For the micrographs presented in this work, the acceleration voltage for the electron beam was chosen between 2 and 4 kV. Significantly higher values can lead to irreversible structural changes of the sample surface. If not stated differently, the SEM “InLens” detector was used. The maximum lateral resolution that was achieved with the Zeiss Ultra plus instrument applied in this study is about 5 nm.

The energy dispersive X-ray (EDX) spectroscopy mode of the SEM was employed to analyze the distribution of chemical elements in sample cross sections by investigation of the fractured edges. Inelastic scattering of the incident electrons by inner core level electrons causes an energy transfer that allows the inner electrons to escape from the atom. Electrons in higher energetic levels can relax into this free state, emitting the excess energy as an X-ray photon. Its energy equals the difference in energy of the two electronic states [96]. Therefore, it carries characteristic information on the emitting atom and therefore on the chemical composition of the sample in the beam focus. The spatial resolution of the EDX measurement is a function of penetration depth of the incident electrons and thus on their energy. Depending on the energy and the composition of the sample, electrons originating from an almost spherical volume with typical lateral extensions ranging from several hundred to 1000 nm are detected. Concerning the chemical selectivity, elements with atomic numbers greater than 5 (Boron) can be detected [93].

An excitation energy of 10 keV, i.e. well above the Mn K_α line at 6.5 keV, was chosen for the EDX investigations. For quantitative analysis, the detector was calibrated to a Ni reference sample. The background and matrix corrections as well as the deconvolution of the individual peaks and their quantitative analysis were conducted using the commercial OXFORD-software that was delivered together with the device.

3.2.2 N_2 Gas Sorption

N_2 gas sorption analysis probes the pore volumes of porous media, allowing to gain information on accessible pores with a pore width in the range of 0.3 to 100 nm [93]. Additional to the distribution of pore widths and mass specific pore volume, the specific surface area of the material can be determined.

The method measures the decrease in gas pressure p when a given amount of gas is dosed onto the sample. The difference between the gas pressure drop in each dosing step compared to a measurement without a sample in the measurement chamber is evaluated. Plotting the mass specific adsorbed volume V_{ads} vs. the pressure p relative to the saturation pressure p_0 at constant temperature (T = 77 K) leads to the adsorption isotherm.

Special care has to be taken to completely remove any gas adsorbed in the sample prior to the measurement, since parasitic gas amounts will distort the experimental data. Therefore, the samples were degassed in vacuum at 300 °C for 4 to 24 h prior to each measurement. The duration of the degassing step was determined by the residual pressure during degassing. After the degassing step, the sample mass was determined and the sample holder was cooled to 77.3 K. Special care was taken to let the system reach thermal equilibrium conditions after each pressure change.

Figure 3.4 shows a typical isotherm of a micro- and mesoporous carbon xerogel. At low relative pressures $p/p_0 < 0.1$, condensation in micropores takes place, leading to a sharp increase in adsorbed volume. In the intermediate range, before a hysteresis loop sets in, the isotherm is closely related to the (external) surface area. The external surface area is defined as the enveloping surface area of the carbon xerogel particles. The hysteresis loop between adsorption and desorption branch indicates the existence and accessibility of mesopores within the sample [97].

In case of a plateau in the isotherm at relative pressure values close to 1.0 (see Figure 3.4), the maximum amount of gas adsorbed can be converted into the total sum of the detectable specific micro- and mesopore volume, assuming that the adsorbate forms a liquid state in the pores of the

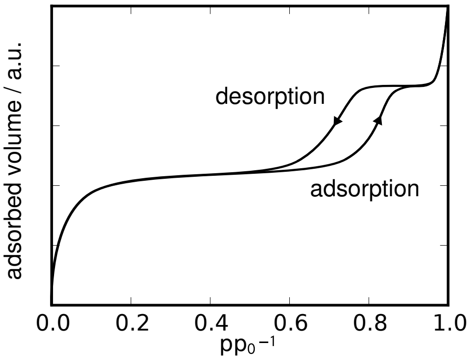

Figure 3.4: Theoretical isotherm of a typical micro- and mesoporous sample.

sample.

The mass specific pore volume V_{pore} can be calculated by the adsorbed gas volume V_{ads} using the density conversion factor $c = 1.546 \cdot 10^{-3}$ cm^3(cm^3(STP))$^{-1}$ for nitrogen at standard temperature $T_{\mathrm{STP}} = 273.15$ K and pressure $p_{\mathrm{STP}} = 1013.25$ mbar, respectively [93]:

$$V_{\mathrm{pore}} = c \cdot V_{\mathrm{ads}}/m, \tag{3.5}$$

where m is the sample mass.

For a non-porous carbon sample without any macropores, the total mass specific volume V_{tot} of the sample refers to its inverse macroscopic density ρ:

$$\frac{1}{\rho} = V_{\mathrm{tot}} = V_{\mathrm{pore}} + \frac{1}{\rho_{\mathrm{C}}}, \tag{3.6}$$

where $\rho_{\mathrm{C}} = 2.2$ g/cm^3 is the density of the solid carbon phase of the xerogel [93, 98].

The total specific surface area of the sample is calculated using the model developed by Brunauer, Emmet and Teller (BET) *et al.* [99], assuming a statistical multilayer coverage of the surface. The model relates the adsorbed specific volume V_{ads} to the respective relative pressure, resulting in the BET equation:

$$\frac{p/p_0}{V_{\mathrm{ads}}(1-p/p_0)} = \frac{1}{C \cdot V_{\mathrm{m}}} + \frac{C-1}{C \cdot V_{\mathrm{m}}} \frac{p}{p_0}, \tag{3.7}$$

where V_{m} is the volume of a monolayer of adsorbed gas molecules and C describes the interaction of the surface with the adsorbate by a Boltzmann-approach:

$$C \approx \exp(\Delta E_{\mathrm{ads}}/RT), \tag{3.8}$$

with the molar gas constant R and the temperature T. The net adsorption energy ΔE_{ads} allows for energy differences in the adsorbed layers [93].

Plotting the left hand side of Equation 3.7 as a function of p/p_0 allows a linear fit to the experimental data and thereby the extraction of V_m and C. Now the BET surface area S_{BET} can be calculated, using a surface area of $S_{\mathrm{N_2}} = 0.162\ \mathrm{nm}^2$ occupied by a single N_2 gas molecule, the Avogadro constant N_A and the molar volume $V_{\mathrm{mol,STP}} = 22414\ \mathrm{cm}^3(\mathrm{STP})/\mathrm{mol}$ [93]:

$$S_{\mathrm{BET}} = \frac{V_\mathrm{m} \cdot S_{\mathrm{N_2}} \cdot N_\mathrm{A}}{V_{\mathrm{mol,STP}}}. \tag{3.9}$$

Because of the simplified assumptions of the BET model, i.e. neglecting the interaction between the molecules in the adsorbed layer as well as the distinction between micro- and mesopores, it is generally recommended for the evaluation of microporous solids to use only data points in the relative pressure range of $0.005 < p/p_0 < 0.15$ [100]. Otherwise, for microporous samples, the C-value will become negative and therefore non-physical. For the BET analysis applied in this thesis, the fit range was shifted to lower relative pressures until the C-value returned to positive values.

In order to separate the micropore contribution from the total surface area, S_{BET}, an approach commonly known as the “t-plot method” was applied [101]. Herein, it is assumed that the fraction of the adsorbed volume, V_{ads}, to the volume of a complete monolayer of adsorbed gas molecules, V_m, equals the ratio of a statistical layer thickness t of the adsorbed layer (including density fluctuations [102]) to the monolayer thickness d_m (= 0.354 nm for N_2 at 77 K)[93]:

$$\frac{V_{\mathrm{ads}}}{V_\mathrm{m}} = \frac{t}{d_\mathrm{m}}. \tag{3.10}$$

An empirical formula suggested by Harkins and Jura describes the relation between t and p/p_0 [103]:

$$t = 0.1\ \mathrm{nm}\sqrt{\left(\frac{13.99}{0.034 - \log(p/p_0)}\right)}. \tag{3.11}$$

Plotting the volume adsorbed vs. t leads to a linear dependence in the intermediate pressure range, showing an offset in y-direction for microporous samples. This offset is directly related to the micropore volume V_{mic}. From the slope, the external surface area S_{ext} can be calculated from V_m (Equation 3.10), in analogy to the calculation of S_{BET} in Equation 3.9.

By calculating S_{BET}, S_{ext} and V_{mic} as described above, several useful quantities characterizing the microporous sample can be deduced. The density of the microporous particles, ρ_{part}, of a carbon xerogel can be estimated using the carbon skeleton density ρ_C and the measured mass specific micropore volume V_{mic} [84]:

$$\rho_{\mathrm{part}} = \frac{1}{\frac{1}{\rho_{\mathrm{C}}} + V_{\mathrm{mic}}}. \tag{3.12}$$

Hence, the interparticular specific pore volume V_{inter}, i.e. the meso- and macropores, can be determined [84]:

$$V_{\mathrm{inter}} = \frac{1}{\rho} - \frac{1}{\rho_{\mathrm{part}}}. \tag{3.13}$$

Here ρ is the macroscopic density of the sample.
Assuming a spherical geometry, the diameter, d_{part}, of the particles of the carbon xerogel can be deduced [84]:

$$d_{\mathrm{part}} = 2 \cdot \frac{3}{S_{\mathrm{ext}} \cdot \rho_{\mathrm{part}}}. \tag{3.14}$$

The experimental error in the analysis of sorption data is mainly influenced by the error in choosing the appropriate pore model (slit- or cylindrical shaped pores) and the error of determining the parameters of the fits. The choice of the model represents a systematic error, influencing the absolute values of the quantities, however, having no influence on the comparability of the individual measurements. Therefore, this contribution to the overall error is neglected. The uncertainty in determination of the fit parameters, however, cannot be omitted, leading to a relative error of about $\pm 10\%$ for specific volumes and surface areas. For quantities derived from S_{ext}, S_{BET} or V_{mic}, such as d_{part} and V_{inter}, the error was determined following the laws of error propagation [104].

3.2.3 X-ray Photoelectron Spectroscopy

X-ray photoelectron spectroscopy (XPS) provides information on the electronic structure on an atomic level and therefore on the chemical state of the sample surface. When high energetic photons of several hundred eV hit the sample, core electrons can be released. This photoelectric effect was first discovered by Heinrich Hertz in 1887 and explained theoretically by Albert Einstein in 1905 [105–107]. For photon energies exceeding the ionization energy E_{I}, the incident photon of energy $h\nu$ is able to ionize an atom M and releases an electron with the kinetic energy E_{kin} [108]:

$$h\nu + \mathrm{M} \longrightarrow \mathrm{M}^{+} + e^{-}(E_{\mathrm{kin}}), \tag{3.15}$$

where the kinetic energy of the electron is

$$E_{\mathrm{kin}} = h \cdot \nu - E_{\mathrm{b}} - E_{\mathrm{I}}. \tag{3.16}$$

The ionization energy E_{I} is the lowest energy necessary to lift an electron from the highest occupied state (E_{hos}) to the vacuum level E_{vac}. The binding energy E_{b} is the difference between the energy of the highest occupied state E_{hos} and the energy E_i of the state the electron initially originated from, as depicted in Figure 3.5.

In the simplest case of non-interacting photoelectrons, the current $I(E_i, h\nu)$ of emitted photoelectrons can be calculated using Fermi's golden rule:

$$I(E_i, h\nu) \sim \sum_{f,i} |M_{fi}|^2 \, \delta(E_f - h\nu - E_i). \tag{3.17}$$

Here, the delta function ensures energy conservation between the energy of the initial state E_i and the energy of the final state $E_f = E_i + h\nu$. The transition matrix element $M_{fi} = \langle \Psi_f | \vec{A}\vec{p} | \Psi_i \rangle$ describes the probability of the transition of an electron from the wave function in state Ψ_i to the state Ψ_f. $\vec{A}$ is the effective vector potential and $\vec{p}$ the momentum of the electron [109].

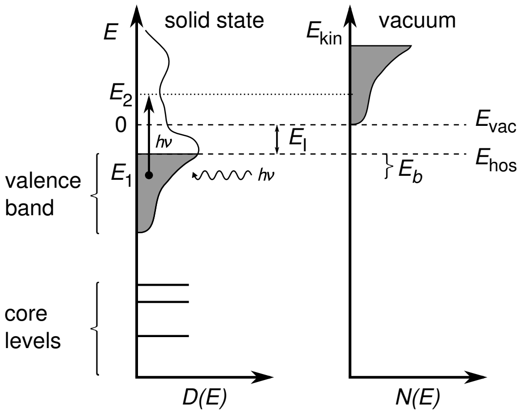

Figure 3.5: Scheme of the energy levels involved in photoelectron spectroscopy. E_1, E_2 are the energy levels of the electron before and after the excitation by the incident photon, respectively. E_{hos} is the energy of the highest occupied state and E_{I} the ionization energy. $D(E)$ is the density of states in the solid, $N(E)$ is the number of photoelectrons with the energy E. Redrawn after [107].

On their way to the surface, the photoelectrons interact with the bound electrons via inelastic scattering (e.g. creating plasmons) and therefore loosing part of their energy, which in turn leads to a finite mean free path. This is the main reason for XPS being surface sensitive with a probing depth of up to 3 nm [107].

Atoms in solid state will show no discrete energy values for the valence states, since the energy is dispersed because of next-neighbor interaction (overlapping wave functions) leading to the formation of energy bands (see Figure 3.5). Valence states are found at low binding energies of $0 < E_{\mathrm{b}} < 20$ eV with respect to the vacuum level. Deeper lying core-level states, however, remain discrete but may change their absolute value with respect to the atom in the gas phase, because of the local chemical environment in the solid [107].

The spectra were acquired using monochromatic Al-K$_\alpha$ excitation at 1486.6 eV and an Omicron

EA 125 electron energy analyzer with an experimental line broadening of 1.1 eV. The spectra are normalized to the C1s peak and a standard Shirley background correction has been carried out. For calculating peak areas, the peaks are fitted by a Gaussian distribution:

$$f(E) = \frac{1}{\sigma\sqrt{2\pi}} \exp\left(-\frac{1}{2}\left(\frac{E-\mu}{\sigma}\right)^2\right), \tag{3.18}$$

where σ^2 is the variance and μ the center of the peak. The peak area $\int f(E)dE$ can be used to quantify the relative peak contributions of each chemical species.

The XPS sample preparation, measurements, data reduction and analysis was carried out at AK Claessen, Experimental Physics IV.

3.2.4 Anomalous Small Angle X-ray Scattering

Small angle X-ray scattering (SAXS) is widely used in material science, e.g. for probing phase-separated alloys [110] or, in biological science, to investigate the shape of molecules [111]. For the characterization of porous solids, it is a well established method, e.g. for silica and carbon aerogels [112, 113]. Due to the reciprocal space relation, large structures, e.g. the size of colloidal particles up to several hundred nm, are resolved at small angles ($0.001° < 2\theta < 10°$) [93]. The scattering at larger angles ($2\theta > 5°$) is commonly known as X-ray diffraction (XRD), where Bragg diffraction peaks can be used to analyze the lattice structure of crystals.

For SAXS experiments, the energy of the incident photon is of the order of 10 keV, which is considerably higher than the binding energies within the atom. The electrons can therefore be considered quasi-free and the scattering occurs quasi-elastic. The major scattering mechanism for SAXS is the scattering of the photon by an electron density distribution. The scattering intensity therefore is sensitive to the number of electrons or the atomic number Z, and their spatial distribution. In contrast, small angle neutron scattering (SANS) is sensitive to isotopes of an element, since the scattering mechanism of the neutron is governed by the interaction of the neutral neutron with the nucleus. From an electrodynamical point of view, the incident monochromatic X-rays with a wavelength λ excite electrons of the atoms to oscillate, thereby emitting spherical waves of – in the elastic case – the same wavelength λ. This coherent scattering is also referred to as Rayleigh scattering [114].

The reciprocal space relation is easily understood when looking at Figure 3.6. In Figure 3.6a, a spherical particle acts as scattering center for a monochromatic coherent plane wave of wavelength λ and wave vector $\vec{k}$ [115]. Assume the scattered wave from two arbitrary points within the sphere at relative distance $\vec{r}$, with a path difference λ and a wave vector $\vec{k}'$ in the direction of

2θ. The corresponding scattering vector or momentum transfer $\vec{q} = \vec{k}' - \vec{k}$ is of the magnitude $q = (4\pi/\lambda)\sin(2\theta/2)$ (see Figure 3.6).

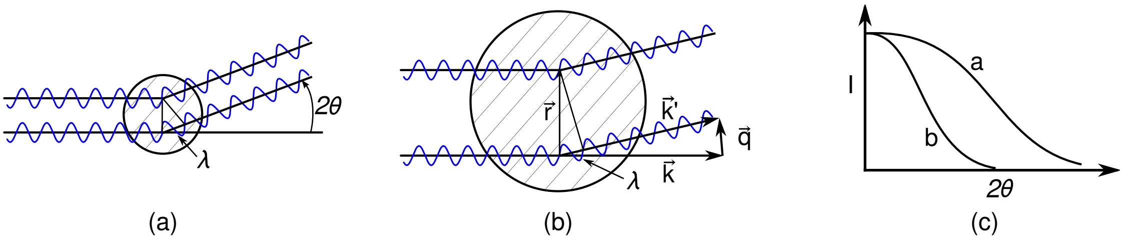

(a) (b) (c)

Figure 3.6: Schematic representation of the scattering geometry and the resulting scattering intensity (c) for small (a) and large particles (b), respectively. Graphic reproduced from [115].

The qualitative trend of the resulting scattering is depicted in Figure 3.6c). For larger particles (Figure 3.6b)), at the same incident wave length λ, scattering results in a more narrow scattering curve (curve b in Figure 3.6c)).

At large scattering angles, the intensity vanishes, and only constructive interference of the scattering at atomic layers with a layer distance d_{hkl} survives, leading to peaks, if the Bragg-condition

$$n \cdot \lambda = 2 \cdot d_{hkl} \cdot \sin(2\theta/2) \tag{3.19}$$

is fulfilled. Here, n is the order of the peak and the Miller-indices hkl indicate the scattering lattice plane.

The scattering of electrons by an atom can be calculated by the Fourier transformation of the electron density distribution within the atom. For Mn, C and O the results are shown in Figure 3.7 (a). The atom form factor f depends on the atomic number Z and the Bragg scattering angle 2θ. As is shown in Figure 3.6, major contributions to the scattering intensity only occur at 2θ=0, where the scattering factor equals the number of electrons Z. Therefore, in the common SAXS experiment, f can be assumed independent of the incident photon energy E and also of the scattering vector q, since only small angles ($q < 1$ nm^{-1}) are considered and f is approximately constant in that region.

At an element's absorption edge, however, the atomic form factor turns complex and shows a strong energy dependence, therefore deviating strongly from the number of electrons $Z_i := f_i^0$ [116]:

$$f_i(E) = f_i^0 + f_i'(E) + i f_i''(E). \tag{3.20}$$

Here, $f_i'(E)$ and $f_i''(E)$ are the anomalous scattering factors that are tabulated in reference [117] or that can be obtained by the Cromer-Liberman calculations [118, 119] (see also Figure 3.7 (b)). This specific energy dependence led to the use of the term "anomalous", however, since all elements show this kind of energy dependence, the term can be regarded inappropriate. To more precisely reflect the physical circumstances, the term “resonant small angle X-ray scattering” (RSAXS) was suggested to be used instead [120]. However, since “ASAXS” is more frequently used in literature than “RSAXS”, the nomenclature “ASAXS” will be kept in the following.

For continuous media, the total scattering amplitude $F(\vec{q},E)$ constituted by all atoms i in the exposed volume V reads

$$F(\vec{q},E) = \int_V \sum_i f_i(E)\rho_i(\vec{r})e^{-i\vec{q}\vec{r}}\mathrm{d}\vec{r}, \tag{3.21}$$

which is the integrated 3D Fourier transform of the scattering length density $\rho_i(\vec{r})$ and therefore includes all structural information of the material in the irradiated volume.

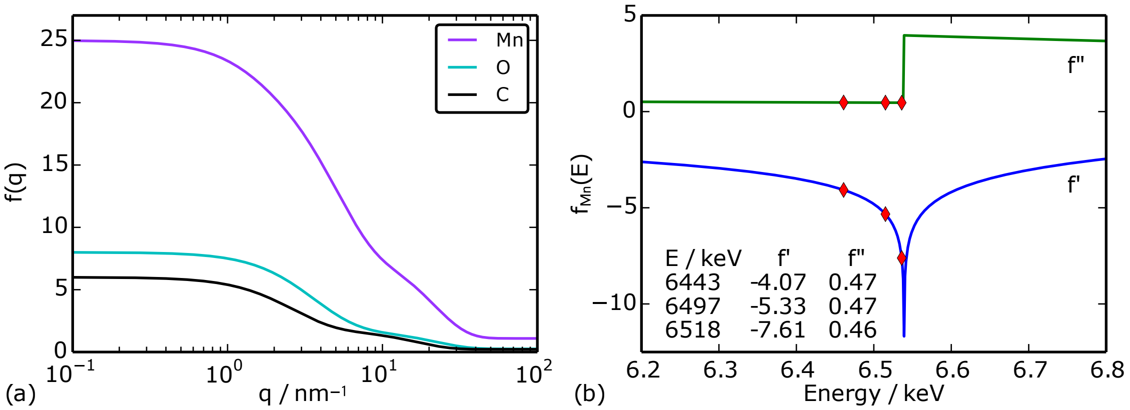

Figure 3.7: (a) Atomic scattering factors for Mn, C and O atoms, respectively, calculated by the formula given by Doyle and Turner as described by Waasmeier *et al.* [121–123] (semilogarithmic). (b) Energy dependence of the atomic scattering factor at the K-edge of Mn, calculated by the Cromer-Liberman equations [118, 119]. Diamond markers indicate the energies listed in the legend, at which the ASAXS measurements were performed in this thesis.

The scattered intensity measured by the detector in the SAXS experiment is the square of the absolute value of the scattering amplitude:

$$I(\vec{q},E) = F(\vec{q},E)F(\vec{q},E)^* = |F(\vec{q},E)|^2 = \left| \int_V \sum_i f_i(E)\rho_i(\vec{r})e^{-i\vec{q}\vec{r}}\mathrm{d}\vec{r} \right|^2 . \tag{3.22}$$

Therefore, the phase information of the scattering amplitude is lost and the direct re-transformation of Equation 3.21 into the real space structure is not possible. In contrast to SAXS measurements, where incoherent Compton- and Raman-scattering can be neglected, ASAXS requires a careful treatment of the isotropic background scattering. The treatment will be discussed in detail in the experimental conditions described later in this section.

Using the expression

$$S_i(\vec{q}) = \int_V \rho_i(\vec{r}) e^{-i\vec{q}\vec{r}} \mathrm{d}\vec{r}, \tag{3.23}$$

the energy- and $\vec{q}$ dependence can be separated [116]:

$$I(\vec{q},E) = |F(\vec{q},E)|^2 = \left| \sum_i f_i(E) S_i(\vec{q}) \right|^2 . \tag{3.24}$$

This general formula can be used to derive the scattering form factor $S_i(q)$ of one kind of element i present in a composited material, if measurements at the absorption edge of one of the components are experimentally feasible. Several ways of treatment have been proposed to deduce the form factors. Here, the approach of Goerigk *et al.* will be described [124, 125].

For the $\mathrm{CMnO_2}$ hybrid material under investigation, the scattering amplitude, according to Equation 3.21, reads

$$F(\vec{q},E) = \int_V f_{\mathrm{Mn}}(E)\; \rho_{\mathrm{Mn}}(\vec{r})\; e^{-i\vec{q}\vec{r}} \mathrm{d}\vec{r} + \int_V f_{\mathrm{C}}\; \rho_{\mathrm{C}}(\vec{r})\; e^{-i\vec{q}\vec{r}} \mathrm{d}\vec{r}. \tag{3.25}$$

The atomic scattering factor f_{C} of carbon is nearly constant for energies E close to the absorption edge of Mn, whereas $f_{\mathrm{Mn}}(E)$ shows a strong energy dependence according to Equation 3.20 (see Figure 3.7 (b)). Applying Equation 3.24 leads to a sum of three contributions:

$$I(q,E) = |F_{\mathrm{Mn}}(q,E)|^2 + |F_{\mathrm{mix}}(q,E)|^2 + |F_{\mathrm{C}}(q)|^2 , \tag{3.26}$$

where, for isotropic media,

$$|F_{\mathrm{Mn}}(q,E)|^2 = 4\pi |f_{\mathrm{Mn}}(E)|^2 \int_V \int_V \rho_{\mathrm{Mn}}(\vec{r}) \rho_{\mathrm{Mn}}(\vec{r}') \frac{\sin(q|\vec{r}-\vec{r}'|)}{q|\vec{r}-\vec{r}'|} \mathrm{d}\vec{r}\mathrm{d}\vec{r}', \tag{3.27}$$

$$|F_{\mathrm{mix}}(q,E)|^2 = 4\pi |f_{\mathrm{Mn}}(E)|\, |f_{\mathrm{C}}| \int_V \int_V \rho_{\mathrm{Mn}}(\vec{r}) \rho_{\mathrm{C}}(\vec{r}') \frac{\sin(q|\vec{r}-\vec{r}'|)}{q|\vec{r}-\vec{r}'|} \mathrm{d}\vec{r}\mathrm{d}\vec{r}', \tag{3.28}$$

$$|F_{\mathrm{C}}(q)|^2 = 4\pi |f_{\mathrm{C}}|^2 \int_V \int_V \rho_{\mathrm{C}}(\vec{r}) \rho_{\mathrm{C}}(\vec{r}') \frac{\sin(q|\vec{r}-\vec{r}'|)}{q|\vec{r}-\vec{r}'|} \mathrm{d}\vec{r}\mathrm{d}\vec{r}'. \tag{3.29}$$

The first term, $|F_{\mathrm{Mn}}(q,E)|^2$, describes the resonant scattering of Mn atoms, therefore including the information of the Mn scattering form factor. The second term is the so called “cross term”, $|F_{\mathrm{mix}}(q,E)|^2$, resulting from the superposition of the resonant and non-resonant scattering of both elements present. The non-resonant scattering of the carbon atoms is described by the third term, $|F_{\mathrm{C}}(q)|^2$.

Separated Intensity

The non-resonant term can be removed by measuring the scattering intensity at two different energies E_1, E_2 close to an absorption edge and subtracting the corresponding intensities:

$$\Delta I(q, E_1, E_2) = I(q, E_1) - I(q, E_2), \tag{3.30}$$

yielding

$$\begin{aligned}\Delta I(q, E_1, E_2) &= 4\pi \cdot 2 f_{\mathrm{C}}(f'_{\mathrm{Mn}}(E_1) - f'_{\mathrm{Mn}}(E_2)) \int_V \rho_{\mathrm{Mn}}(\vec{r})\rho_{\mathrm{C}}(\vec{r}\,') \frac{\sin(q|\vec{r} - \vec{r}\,'|)}{q|\vec{r} - \vec{r}\,'|} \mathrm{d}\vec{r}\mathrm{d}\vec{r}\,' + \\ &+ (|f_{\mathrm{Mn}}(E_1)|^2 - |f_{\mathrm{Mn}}(E_2)|^2) \int_V \rho_{\mathrm{Mn}}(\vec{r})\rho_{\mathrm{Mn}}(\vec{r}\,') \frac{\sin(q|\vec{r} - \vec{r}\,'|)}{q|\vec{r} - \vec{r}\,'|} \mathrm{d}\vec{r}\mathrm{d}\vec{r}\,'.\end{aligned} \tag{3.31}$$

This so called “separated intensity” includes only contributions by resonant scattering, however, the carbon scattering is still present due to $\rho_{\mathrm{C}}(\vec{r}\,')$. By means of an additional measurement at a third energy, subtracting the separated intensity $\Delta I(q, E_1, E_3)$ from Equation 3.31 leads to the squared Fourier transform of the form factor $\tilde{S}_{\mathrm{Mn}}(q)$, after normalizing to the anomalous dispersion corrections:

$$\begin{aligned}|\tilde{S}_{\mathrm{Mn}}(q)|^2 := S_{\mathrm{Mn}}(q) &= \left[\frac{\Delta I(q, E_1, E_2)}{f'_{\mathrm{Mn}}(E_1) - f'_{\mathrm{Mn}}(E_2)} - \frac{\Delta I(q, E_1, E_3)}{f'_{\mathrm{Mn}}(E_1) - f'_{\mathrm{Mn}}(E_3)}\right] \cdot \frac{1}{F(E_1, E_2, E_3)}, \\ F(E_1, E_2, E_3) &= f'_{\mathrm{Mn}}(E_2) - f'_{\mathrm{Mn}}(E_3) + \frac{f''^2_{\mathrm{Mn}}(E_1) - f''^2_{\mathrm{Mn}}(E_2)}{f'_{\mathrm{Mn}}(E_1) - f'_{\mathrm{Mn}}(E_2)} - \frac{f''^2_{\mathrm{Mn}}(E_1) - f''^2_{\mathrm{Mn}}(E_3)}{f'_{\mathrm{Mn}}(E_1) - f'_{\mathrm{Mn}}(E_3)}.\end{aligned} \tag{3.32}$$

This equation directly relates to the spatial distribution of the Mn atoms within the sample. For convenience and in accordance with the literature, Equation 3.32 will be referred to as the scattering form factor $S_{\mathrm{Mn}}(q)$ of the Mn atoms [125].

Hollow Sphere Model

Within the framework of this study, the approach has been developed to describe the Mn form factor by the scattering of a hollow sphere (Hsph) with shell thickness h_{x}, inner radius R_{i} and outer radius $R_{\mathrm{a}} = R_{\mathrm{i}} + h_{\mathrm{x}}$ [115]:

$$S_{\mathrm{Hsph}}(q, d, R_{\mathrm{i}}) = \frac{1}{V_{\mathrm{sphere}}} \cdot 16\pi^2 \Delta\rho^2 \left(R_{\mathrm{a}}^3 \Phi_{\mathrm{sph}}(q, R_{\mathrm{a}}) - R_{\mathrm{i}}^3 \Phi_{\mathrm{sph}}(q, R_{\mathrm{i}})\right)^2 + C_{\mathrm{bg}}, \tag{3.33}$$

where $\Delta\rho = \rho_{sph} - \rho_{void}$ is the scattering contrast between the sphere and the void (pore) and $\Phi_{\mathrm{sph}}(q,r)$ is the scattering amplitude of a sphere of radius r:

$$\Phi_{\mathrm{sph}}(q,r) = \left(\frac{\sin(qr) - qr\,\cos(qr)}{(qr)^3} \right). \tag{3.34}$$

The term C_{bg} allows to include a (constant) background scattering contribution, e.g. by fluorescence. The scattering intensity is normalized to the single particle volume $V_{\mathrm{sphere}} = \frac{4\pi}{3} R_{\mathrm{a}}^3$.

Experimental Conditions

The ASAXS measurements were performed at beamline B1 at the HASYLAB (Hamburger Synchrotronstrahlungslabor) at DESY (Deutsches Elektronen-Synchrotron). The samples were degassed for several hours in vacuum at 100 °C prior to transfer into the measurement chamber. The experiments were performed at the K-edge of Mn (6539 eV [117]) at energies of E_1 = 6443, E_2 = 6497 and E_3 = 6518 eV (calibrated to the Mn K-edge, see also Figure 3.7 (b)). The incident X-ray intensity was of the order of $2{\cdot}10^7$ photons/(s mm^2). Data sets were obtained at two detector distances of 666 and 3585 mm, thus covering a total range in the scattering vector q from 0.06 to 3 nm^{-1}. In order to correct the spectra for Raman scattering and fluorescence, the intensities $I(q,E_2)$ and $I(q,E_3)$ were modeled by varying the constant background term to yield the same slope at q-values $q > 2$ nm^{-1} as for the curve $I(q,E_1)$, which refers to the intensity at the lowest energy and therefore is expected to show the lowest luminescence.

3.3 Electrochemical Methods

In order to characterize the electrochemical behavior of the electrodes, cyclic voltammetry and electrochemical impedance spectroscopy measurements were conducted by means of an electrochemical cell. The setup and the major steps to evaluate the data are described in the following sections.

3.3.1 Electrochemical Cell

Electrochemical measurements were conducted in a three-electrode sandwich cell. The cell consists of two polytetrafluoroethylene (PTFE, “Teflon”) blocks, held together by four titanium screws. Titanium plates act as current collectors, working- and counter- electrode are separated by a sheet of glass fiber paper. The working electrode is the supercapacitor electrode under investigation. The counter electrode is necessary to complete the electrical circuit. Voltages are measured against a reference electrode defining a constant reference potential. An Ag/AgCl (3 M NaCl) reference

electrode with a potential of 0.286 V vs. the normal hydrogen evolution (NHE) potential was used in the experimental setup [126]. Special care was taken to monitor the reference electrode potential versus the “lab-master“ electrode, a commercial reference electrode (Sensortechnik Meinsberg, KE 11) that is exclusively used for calibrating the reference electrodes. If deviations greater than 50 mV compared to the ”lab-master“ electrode occurred, the reference electrode was renewed, following the steps given in [127]. All potentials presented in this thesis are given in relation to the potential of the Ag/AgCl reference electrode, if not explicitly stated otherwise.
For characterization of powders, a cavity micro electrode (CME) was applied. The electrode was prepared following the description in the literature [34, 128]. In short, a Pt-wire with a diameter of $d_{\mathrm{Pt}} = 100$ µm was sealed into a glass capillary. Via electrochemical etching, a 80 µm deep cavity was created. In order to fill the CME cavity, small parts of the samples were broken off and lightly ground with a mortar. After careful cleaning with ethanol and distilled water in an ultrasonic batch, the cavity was filled by pressing and rubbing the CME onto the powder.

For all experiments a 1 M Na_2SO_4 aqueous electrolyte solution was used. The electrolyte was degassed by bubbling with N_2 for 10 min prior to each measurement to remove oxygen from the electrolyte. The electrodes were 19 mm in diameter with an average thickness of about 0.2 mm. For each measurement the CV cycle was applied three times, in order to ensure stable conditions. Deviations between the 2. and 3. cycle were below 3 %.

A potentiostat and frequency analyzer (Ivium n-Stat), operated with the supplied commercial software was used for controlling the experiments (for circuitry see Figure 3.8). The data were processed using a *SQLite*-database and *python*-analysis scripts developed by our group (V. Lorrmann and C. Weber).

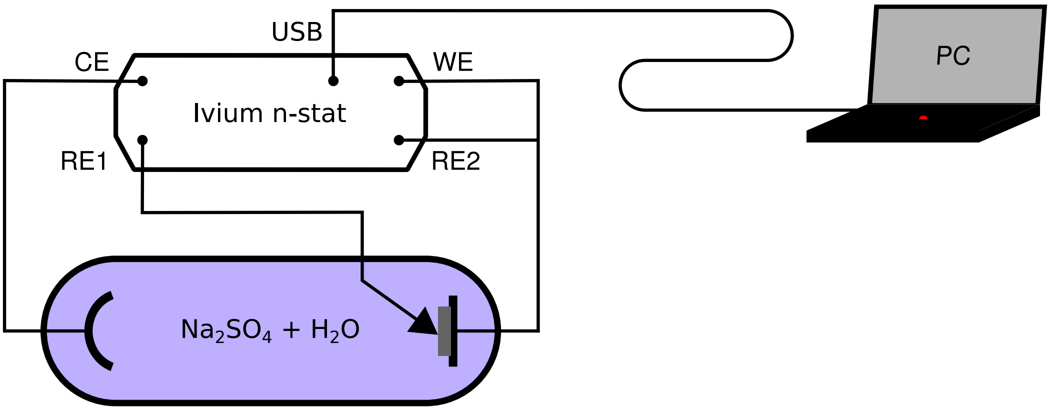

Figure 3.8: The figure shows a schematic of the setup for the EC experiments. The reference electrode (RE1), working electrode (WE) and counter electrode (CE) are connected to the Ivium n-Stat potentiostat and frequency analyzer. The second sense input (RE2) is connected to the WE. Via an USB connection the experiments are controlled by a PC, operated with commercial software.

3.3.2 Cyclic Voltammetry

As mentioned before, the capacitance of electrochemical capacitors strongly depends on the applied voltage. Thus, Equation 2.2 provides a direct approach to measure the differential capacitance C_{diff} of a given electrode [19, 20].

In a typical electrochemical cyclic voltammetry (CV) experiment, the potentiostat measures the current response $I = \mathrm{d}q/\mathrm{d}t$ of the working electrode to an applied constant potential sweep rate $\mathrm{d}E/\mathrm{d}t$ when the electrode is cycled between the two potentials E_{start} and E_{end}:

$$C_{\text{diff}} = \frac{\mathrm{d}q}{\mathrm{d}E} = \frac{I}{\mathrm{d}E/\mathrm{d}t}. \tag{3.35}$$

Figure 3.9 shows the current answers of an ideal capacitor, an RC-circuit and a real double layer electrode with a comparable differential capacitance at a voltage E_0. For the ideal capacitor, C does not depend on the voltage and therefore, when the potential sweep is reversed, the current follows instantaneously. In a real capacitor, contact- and bulk-electrode resistances have to be considered. Additionally, self-discharge of the capacitor by leakage currents can be included by a resistance parallel to the capacitance, when modeling the corresponding circuit (see also Figure 3.10 (a)). These resistive contributions are summarized as an equivalent series resistance (ESR). As a consequence of this ESR, the corners of the CV-diagram become curved. In the double layer capacitor, an additional slope in the formerly horizontal part and sharp edges at the turning potentials of the sweep can occur because of the charging behavior of the porous electrode. A network of RC-circuits that represents the porous framework can be introduced to describe this behavior (see Section 3.3.3).

For obtaining the total capacitance C, the resulting current response is integrated over the time $(t_{\text{start}}, t_{\text{end}})$ required for one sweep between the potentials $E_{\text{start}}, E_{\text{end}}$ and divided by the applied voltage window $\Delta E = E_{\text{end}} - E_{\text{start}}$:

$$C = \frac{1}{\Delta E} \int_{t_{\text{start}}}^{t_{\text{end}}} I \, \mathrm{d}t = \frac{Q}{\Delta E}. \tag{3.36}$$

In order to compare electrodes supplied from different production series, it is useful to normalize the capacitance to the electrode mass m or to the electrode volume V, resulting in the gravimetric capacitance C_{grav} or the volumetric capacitance C_{vol}, respectively:

$$C_{\text{grav}} = C/m, \tag{3.37}$$

$$C_{\text{vol}} = C/V = C\rho/m, \tag{3.38}$$

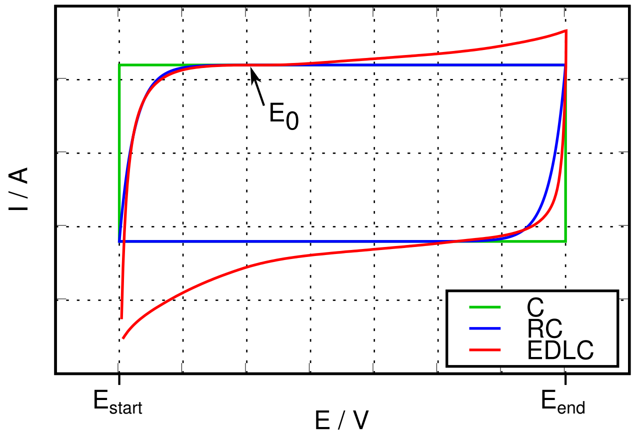

Figure 3.9: Current response of an ideal capacitor (C), an RC-circuit and an electrochemical double layer capacitor (EDLC) with a comparable differential capacitance at a voltage E_0. $E_{\text{start}}, E_{\text{end}}$ represent the start and end of the applied voltage window, respectively.

where ρ is the electrode mass density.

3.3.3 Electrochemical Impedance Spectroscopy

Electrochemical impedance spectroscopy (EIS) is a powerful tool to investigate the frequency behavior of an electrochemical system. At a certain DC bias voltage, E_b, an alternating voltage $\Delta E(\omega) = E_0\ \mathrm{e}^{i\omega t}$ is superimposed to E_b, with a typical amplitude of $E_0 = 5$ mV and a frequency, f, generally ranging from the mHz to the kHz regime. The applicable frequency range is limited by cell- and reaction-stability (lower limit) and inductive behavior of the cables (upper limit). In the general case, the current response of the electrode is delayed by a phase angle, φ, so that $\Delta I(\omega) = I_0\ \mathrm{e}^{i(\omega t+\varphi)}$, where $\omega = 2\pi f$ is the angular frequency and I_0 is the current amplitude. The electrochemical impedance $Z(\omega)$ is then defined as [129]:

$$Z(\omega) = \Delta E(\omega)/\Delta I(\omega) = |Z(\omega)|\mathrm{e}^{-i\varphi} = Z'(\omega) + iZ''(\omega), \tag{3.39}$$

where $Z'(\omega)$ and $Z''(\omega)$ are the real and imaginary part of the impedance, respectively, and $|Z(\omega)|^2 = Z'^2(\omega) + Z''^2(\omega)$ is the square of its absolute value [129, 130].

In Figure 3.10 (a) the equivalent circuit of a double layer capacitor is shown. The series resistance R_s comprises the sum of bulk electrolyte and bulk electrode resistances. The contact resistance R_c accounts for the resistance between the current collector and the electrode, and additionally contains a capacitive part C_c. The double layer capacitance of the electrode is represented by C_dl. The impedance of the equivalent circuit can be calculated, its real- and imaginary part are shown

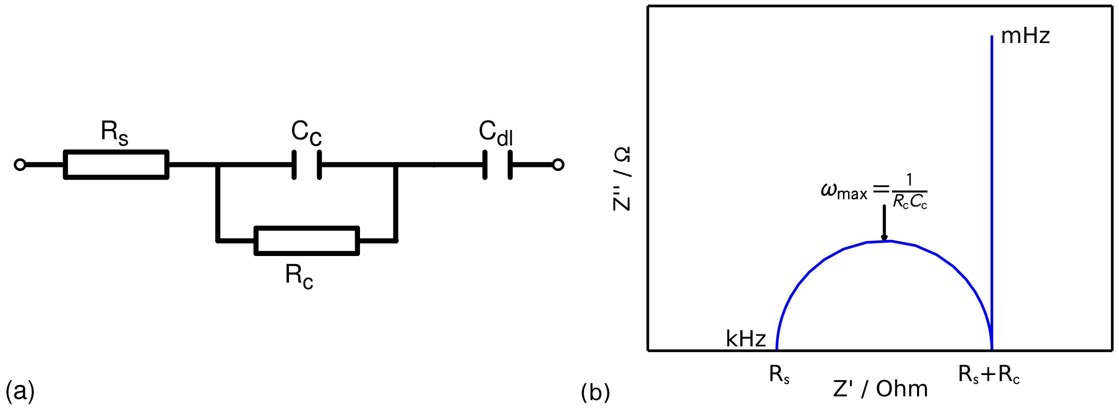

Figure 3.10: (a) Equivalent circuit of a double layer capacitor, including series resistance R_s, contact resistance R_c, current collector capacitance C_c and the double layer capacitance C_dl. (b) Nyquist-plot of the simulated data of the equivalent circuit in a frequency range from mHz to kHz. The semicircle peaks at a characteristic frequency ω_max. The values for R_s and R_c can be found as the intersections with the abscissa.

as a Nyquist-plot in Figure 3.10 (b). For high frequencies in the kHz regime, the current can pass through the capacitances C_c and C_dl and the series resistance R_s is measured. With decreasing frequency, a semicircle appears, peaking at a frequency $\omega_\mathrm{max} = 1/(R_\mathrm{c}C_\mathrm{c})$. From the end of the semicircle R_s +R_c can be derived. For even lower frequencies a steep increase follows, from which the capacitance $C_\mathrm{dl} \overset{\omega\to 0}{=} 1/(i\omega Z'')$ can be calculated. For porous double layer capacitors, C_dl can be replaced by a transmission line model proposed by de Levie, which includes the increasing resistance and capacitance caused by charging of deeper pores at lower frequencies [131].

In an alternative approach, the total impedance $Z(\omega)$ is used to define the capacitance as [132, 133]:

$$C(\omega) = \frac{1}{i\omega Z(\omega)} = \frac{1}{\omega(iZ'(\omega) - Z''(\omega))} = \frac{(iZ'(\omega) + Z''(\omega))}{-\omega|Z(\omega)|^2}, \tag{3.40}$$

where the definition of the absolute value of a complex number was used.

Now the real and imaginary part of $C(\omega) = C'(\omega) + iC''(\omega)$ can be calculated via

$$C'(\omega) = \frac{-Z''(\omega)}{\omega|Z(\omega)|^2}, \tag{3.41}$$

$$C''(\omega) = \frac{-Z'(\omega)}{\omega|Z(\omega)|^2}. \tag{3.42}$$

$C''(\omega)$ includes energy dissipation effects and will peak for real capacitors at a characteristic frequency f_0, thereby defining a characteristic time constant $\tau_0 = 1/f_0$. This time constant is referred to as a dielectric relaxation time of the system [132]. Miller defines τ_0 as a figure of merit for supercapacitors [134].

Distinguishing C_{dl} from C_{Φ} experimentally

The relations of the double layer capacitance C_{dl} and the pseudocapacitance C_{Φ} are easily understood by means of an equivalent circuit, as shown in Figure 3.11. For a pseudocapacitance electrode C_{Φ} is coupled parallel to C_{dl}, but in series with a resistance R_{F} representing the finite charge transfer rate. In an impedance measurement such a circuit is characterized by two different time constants, i.e. characteristic frequencies, and the two components can be separated [20, 21, 35]. However, due to the porous nature of the $\mathrm{CMnO_2}$ electrodes, a distribution of RC-time constants may arise due to charging of pores at different depths, thus making it impossible to extract the individual time constant [35].

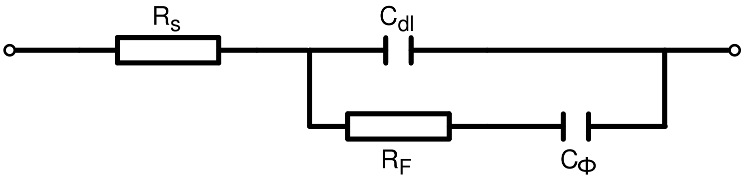

Figure 3.11: Equivalent circuit of a pseudocapacitance electrode with an equivalent series resistance R_{s}, followed by a parallel configuration of double layer capacitance C_{dl} and pseudocapacitance C_{Φ}. In series with C_{Φ}, a resistance R_{F} accounts for charge transfer resistances.

In Figure 3.12, a Nyquist-plot and the real and imaginary part of the total capacitance for the equivalent circuit in Figure 3.11 are shown. While keeping all other parameters constant, C_{Φ} is varied between 0.001 and 30 F. In the Nyquist plot this leads to the evolution of a semicircle, however, even for high values of C_{Φ} it does not intersect the Z_{re}-axis at higher frequencies again. The real part of the total capacitance is close to zero for high frequencies (see Figure 3.12 (b)), at around 0.2 Hz it increases and saturates for lower frequencies. The intersection with the ordinate is a measure for the sum of C_{dl} and C_{Φ}. The imaginary part of the total capacitance reveals the two time constants of the circuit. For low values of C_{Φ} the contribution of C_{dl} dominates, resulting in a broad peak around 0.07 Hz corresponding to a time constant of $\tau = 14$ s. With increasing C_{Φ}, this peak keeps its frequency position, while a second peak evolves at lower frequencies. As noted before, the porous nature of the hybrid electrodes might cause a distribution of RC time constants, broadening both peaks and making their separation difficult.

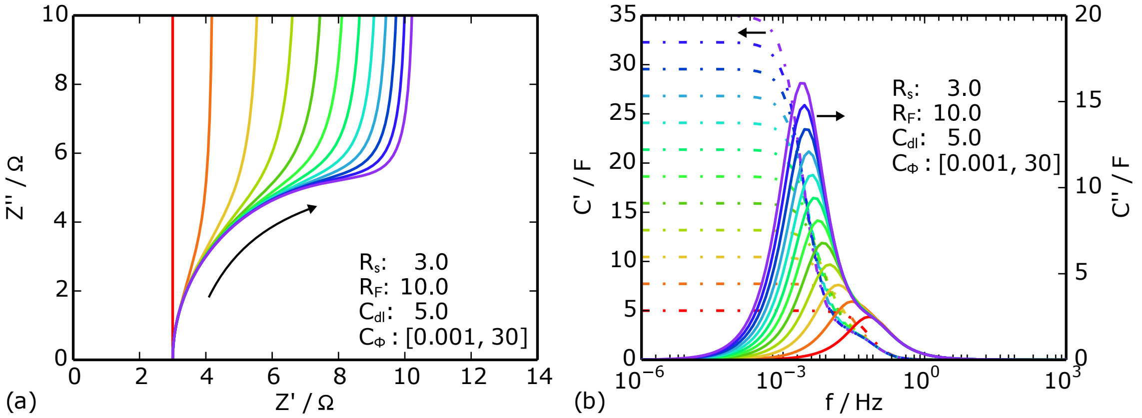

Figure 3.12: Simulation of the equivalent circuit model presented in Figure 3.11, presenting a Nyquist-plot (a) and the real- and imaginary part of the total capacitance in dash-dotted and solid lines, respectively (b). The parameters applied can be read from the inset in Figure (b). C_Φ was varied between 0.001 (red line) and 30 F (violet line).

Chapter 4

Variation of MnO_2 Content

In preliminary works, an extensive study of the C-MnO_2 system was performed [135]. In this context, a fiber reinforced carbon xerogel was impregnated with MnO_2 as described in Chapter 3.1.2. The deposition time and the concentration of $NaMnO_4$ in the precursor solution were varied. It was shown that a low concentration of $NaMnO_4$ in the precursor results in the best electrochemical performance of the CMnO_2 electrodes in terms of charging time and capacitance. The first step within the framework of this PhD thesis therefore was to vary the deposition time for a concentration of 0.05 M $NaMnO_4$ (sample series CMnT).

The series was characterized by means of structural and electrochemical methods. The MnO_2 mass uptake with deposition time was monitored (Section 4.1.1). SEM imaging is used to qualitatively analyze the surface structure of the hybrid electrodes (Section 4.1.2). The analysis of the pore structure using N_2 gas sorption is described in Section 4.1.3. In the following sections, the influence of the structural changes due to MnO_2 deposition on the electrochemical behavior of the electrodes is presented. The influence on the total capacitance is reported in Section 4.2.1, its dynamic behavior is discussed in Section 4.2.2. Finally, impedance spectroscopy analysis is used to quantify the influence of the structural changes on the electrochemical behavior (Section 4.2.3). A conclusion at the end of this chapter summarizes the findings.

4.1 Morphology of Electrodes

4.1.1 MnO_2 Mass Uptake

As already mentioned in the experimental section (Section 3.1.2), the relative MnO_2 mass uptake can be normalized to two different quantities, leading to different results for interpretation:

1) normalizing to the mass of carbon of the electrode: $$\Delta m_C = m_{MnO_2}/m_C, \quad (4.1)$$

2) normalizing to the total mass of the electrode: $$\Delta m_1 = m_{MnO_2}/m_1. \quad (4.2)$$

Here, $m_1 = m_{MnO_2} + m_C$ is the total mass of the electrode. Whereas method 1) is the inherent approach, i.e. normalizing to the quantity that does not change during the experiment, method 2) is widely used when discussing pseudocapacitors, since one is interested in the capacitance in relation to the total mass of the electrode. However, a general application of this normalization has its pitfalls, as will be shown in Figure 4.1.

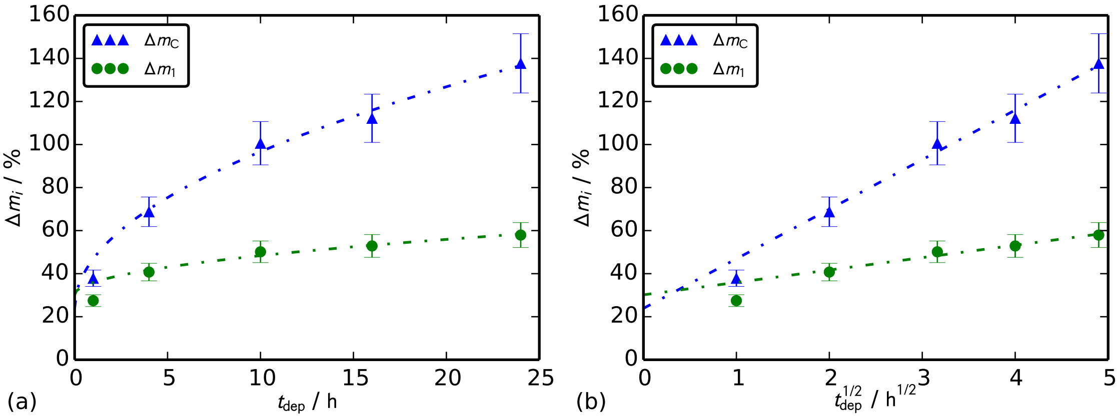

Figure 4.1: MnO_2 mass uptake vs. deposition time t_{dep} (a) and the square root of t_{dep} (b) for series CMnT normalized to m_C (blue triangular markers) and to m_1 (green circular markers). The error bars include the weighting error and an error related to the mass of residual water.

Figure 4.1 (a) shows the relative mass uptake for series CMnT normalized using the two methods mentioned above. The green data points show a strong increase for deposition times shorter than 10 h and seem to saturate around 55 wt.%. This behavior was attributed to a ”self-limiting“ process by Fischer *et al.* [15, 16]. However, this saturation is likely to originate from an artifact due to the normalization applied in their papers (method 2)), since $(x - x_0)/x < 1$, $\forall x > x_0$.

Using method 1) to normalize to the carbon mass of the electrode, the saturation of mass uptake does not appear (blue triangular markers in Figure 4.1 (a)): After a strong increase for deposition times shorter than 10 h, the mass uptake seems to level into a constant slope. Plotting the data vs.

the square root of the deposition time t_{dep} reveals that the data points for $t_{\text{dep}} \geq 4$ h form a straight line. A fit with a square root function confirms the $\sqrt{t_{\text{dep}}}$ dependence (dashed lines in Figure 4.1), therefore hinting at a diffusion limited deposition mechanism for longer deposition times. For deposition times shorter than 4 h, a different mechanism seems to control the early phase of the deposition, most likely exclusively limited by the available carbon surface. This mechanism was proposed by Ma *et al.* and was summarized in Section 3.1.2 [90].

4.1.2 Electrode Surface Structure

Scanning electron microscopy was employed to obtain a qualitative impression of the inner surface of the sample before and after MnO_2 deposition. Figure 4.2 shows representative details of the sample surface of the untreated carbon xerogel and composite samples impregnated for 1 h and 24 h, respectively. The micrographs were taken in the center of a fractured edge of the respective sample, therefore showing the sample surface at an ”inner“ region of the electrode. Possible gradients due to the deposition are discussed in Section 5.1.2. For the samples used in this series however, no gradients were observed.

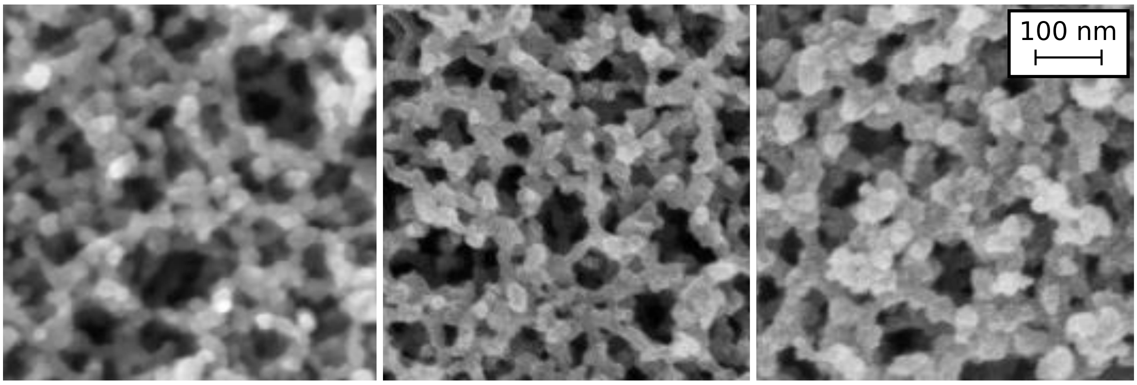

Figure 4.2: SEM micrographs showing the untreated carbon scaffold (left), the composite after 1 h (middle) and after 24 h of MnO_2 deposition (right). All micrographs refer to the same scale shown on the right.

The image of the untreated carbon shows the well interconnected mesoporous network of particles. The average particle size can be estimated to be around 20 nm.

After 1 h of deposition, no significant increase in the particle diameter is visible. Nevertheless, as shown in Figure 4.1, this sample exhibits a significant mass uptake of 38 %. Therefore, MnO_2 must have been deposited either in the micropores of the sample or in a very thin layer on the surface of the carbon particles, which is not visible by SEM.

A significant change in the morphology can be observed after 24 h of deposition: The structure appears more dense and the inter particle pores seem to be smaller. The mean particle diameter increased to about 40 nm. The other samples of the series with deposition times between 4 to 16 hours support the gradual increase in particle diameter (images not shown). No flake- or needle-like surface structure was found, in contrast to literature and to samples with even higher mass uptakes (see Chapter 5).

Summarizing the findings from SEM investigations, low mass loadings of MnO_2 might either be deposited in the micropores of the carbon xerogel or on the external surface area of the carbon particles (cases 2 and 4 in Figure 1.2). For longer deposition times, a deposition on the external surface area is more likely. No domains of MnO_2 clusters were found throughout the sample series. Therefore, case 3 in Figure 1.2 can be excluded, i.e. no significant mass fraction of MnO_2 is present in separate phases within the carbon scaffold.

4.1.3 Surface Area and Porosity

In this section, the influence of the MnO_2 deposition on the porous structure of the sample will be presented. Before the data can be discussed in detail, however, the influence of the thermal degassing step prior to the sorption measurement on the MnO_2 phase has to be investigated, since the crystalline state of MnO_2 is known to change with temperature [136]. To do so, one sample was degassed at 100°C for 20 h, an isotherm was measured and then the same sample was degassed at 300°C for 4 h and a second isotherm was recorded. The result is given in Figure 4.3; no significant change in the isotherm at higher degassing temperature can be observed within the experimental error of about 5%, although the micropore volume is slightly higher for the measurement at higher degassing temperature. Since this behavior might be due to better degassing of residual water in the micropores, the higher degassing temperature of 300°C was used for all following measurements.

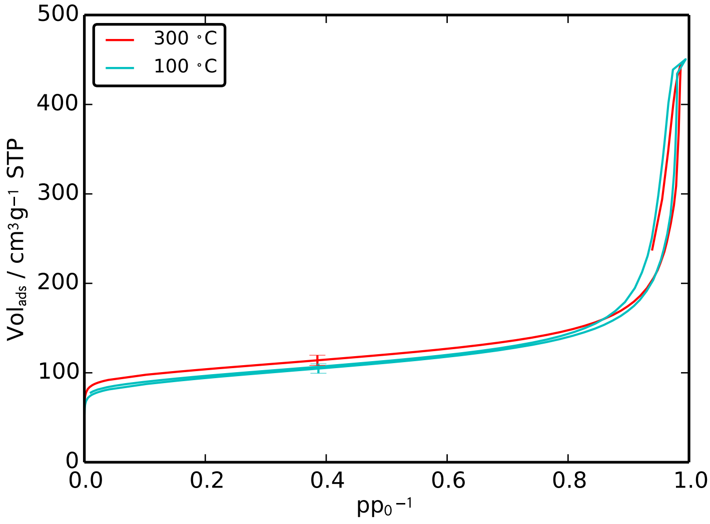

Figure 4.3: Comparison of sorption isotherms taken after degassing a hybrid sample with 14 wt.% MnO_2 at different temperatures. Error bars are drawn exemplarily.

Figure 4.4 (a) shows the N_2 gas sorption isotherms for the sample series CMnT, normalized to the total sample mass, m_1. The untreated carbon xerogel, depicted as ”0 h“ in Figure 4.4, shows a steep adsorption at low relative pressures of $p/p_0 < 0.1$, that is characteristic for microporous samples. For relative pressures above 0.8, a narrow hysteresis loop is visible, hinting at large mesopores and additional macropores being present in the sample.

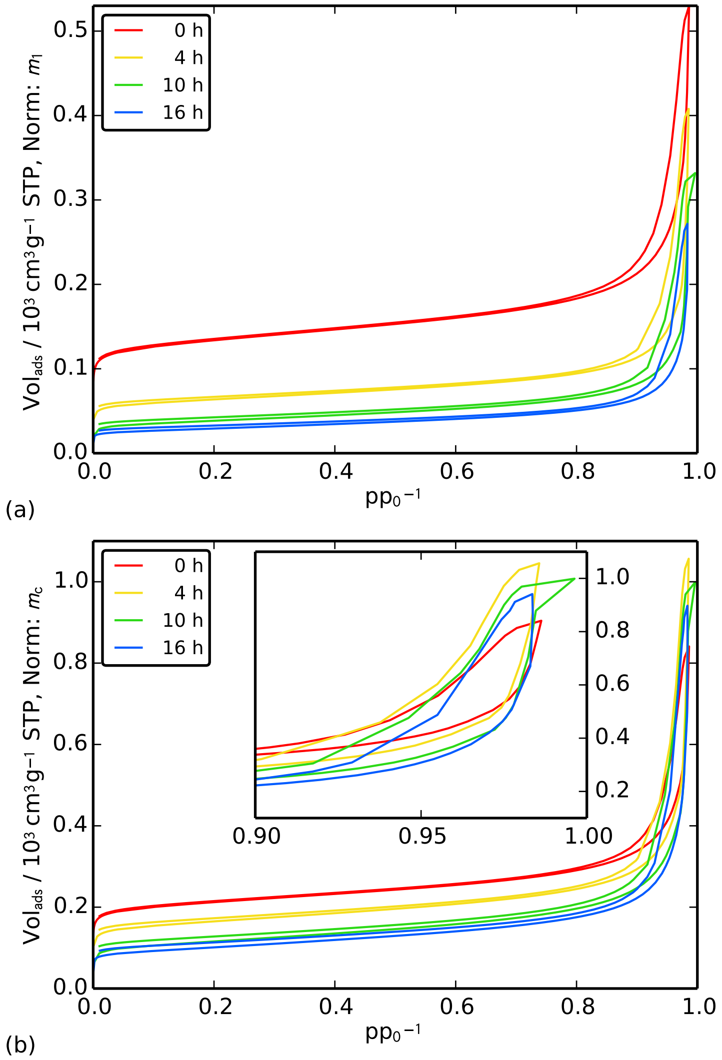

Figure 4.4: N_2 sorption isotherms for series CMnT. The data in the upper graph are normalized to the total sample mass, m_1, the data in the lower graph are normalized to the carbon mass, m_C. The inset shows a magnification of the graph for relative pressures between 0.9 to 1.0.

Exemplarily, the hybrid samples prepared at deposition times of 4, 10 and 16 h were subjected to gas sorption analysis. A first glance at the isotherms unveils that, compared to the carbon xerogel sample, all hybrid samples show a significant decrease in the specific micropore volume and the specific total volume adsorbed (see Figure 4.4 (a)). The MnO_2 deposition process inserts additional mass into the structure. In literature, MnO_2 derived via electrodeposition, but also through the wet-chemical deposition approach used in this work, is often claimed to be microporous in nature and therefore may contribute to the micropore volume of the hybrid sample [16, 60]. Since sorption measurements on bare MnO_2 yield specific micropore volumes around 0.007 cm^3g^{-1} [60], which are of marginal range compared to the specific micropore volumes V_{mic} of about 0.25 cm^3g^{-1} being present in the carbon xerogel, the expected contribution of MnO_2 to V_{mic} appears to be negligible. Therefore, for the qualitative discussion of the sorption isotherms the data have been normalized to the carbon xerogel mass rather than to the total sample mass (Figure 4.4 (b)). This procedure is equivalent to normalizing the isotherms to the macroscopic sample volume, since this quantity does not change upon MnO_2 deposition.

To clarify this normalization, consider a gas sorption measurement of a porous sample with a mass m_s, where you will find an (absolute) adsorbed volume V^1_{ads}. After the measurement, a mass m_2 of a non-porous medium, e.g. a lead sphere, is added to the measurement chamber and the measurement is repeated. It will produce the same absolute value of adsorbed volume, however, the values of the mass specific volume adsorbed will be lower. Therefore, a normalization to the mass of the porous phase in the sample allows to compare the measurements among each other.

In contrast to the results shown later for much larger carbon particles (Chapter 5), the decrease in micropore volume upon MnO_2 deposition is still visible when the data are normalized to the mass of the carbon xerogel. Therefore, in the series CMnT, part of the micropores in the carbon backbone might either be blocked for nitrogen molecules by a layer of MnO_2 on the external particle surface, or filled with MnO_2, as shown in scenario 4 a and c, respectively (see Figure 1.2).

In Figure 4.4 (a), the slope of volume adsorbed at intermediate relative pressures between 0.2 and 0.7 slightly decays with increasing MnO_2 content. In general, this is an indication for an effective decrease of external surface area. When normalized to the carbon xerogel mass (Figure 4.4 (b)) however, the slope is nearly constant for all samples (see also Table 4.1). From the SEM investigation (Section 4.1.2), an increase in particle diameter and therefore decrease of external surface area S_{ext} was expected. Since a corresponding decrease in S_{ext} can not unambiguously be confirmed within the accuracy of the gas sorption data, the deposition of MnO_2 on S_{ext} has to be analyzed by complementary experimental approaches, as discussed in Section 5.3. However, analyzing the total pore volume of the sample can provide further hints on this extent, as will be described in the following.

For all samples subjected to gas sorption analysis, the isotherms do not saturate at relative pressures close to 1 (see Figure 4.4). This means that the pore volume present was not completely filled with the analysis gas, presumably because of macropores or large mesopores being present in the sample but being insusceptible to N_2 sorption. Major cracks in the carbon scaffold, however, can be excluded, since SEM provided no evidence in that perspective.

From the overall sample density and the carbon density, the theoretical (total) pore volume V_{tot} can be calculated using Equation 3.6. The ratio of pore volume detected for the neat carbon xerogel (CMnT 0 h) amounts to $V_{\mathrm{ads}}^{\max}/V_{\mathrm{tot}} = 0.30$, where $V_{\mathrm{ads}}^{\max}$ is the highest point in the sorption isotherm (Figure 4.4 (a)). In order to calculate the pore volume fraction detected in the hybrid samples, the average bulk density

$$\bar{\rho} = \Xi \rho_{\mathrm{MnO_2}}^{\mathrm{x}} + (1 - \Xi)\rho_{\mathrm{part}} \tag{4.3}$$

has to be utilized in Equation 3.6. Here, Ξ is the percentage of MnO_2 in the sample and $\rho_{\mathrm{MnO_2}}^{\mathrm{x}} = 1.62\ \mathrm{gcm^{-3}}$ is the reduced MnO_2 density. The reasons for using $\rho_{\mathrm{MnO_2}}^{\mathrm{x}}$ instead of the MnO_2 bulk density $\rho_{\mathrm{MnO_2}} = 3.00\ \mathrm{gcm^{-3}}$ [137] and its definition will be provided in Chapter 5. Two cases of the particle density, ρ_{part}, can be considered, under the assumption that no MnO_2 was deposited within the micropores:

1) micropores being accessible for the N_2 gas and
2) micropores being inaccessible for the N_2 gas.

In the first case, $\rho_{\mathrm{part}} = \rho_{\mathrm{C}} = 2.2\ \mathrm{gcm^{-3}}$ equals the density of carbon [40], whereas for the second case, the density of a microporous carbon particle $\rho_{\mathrm{part}} = 1.4\ \mathrm{gcm^{-3}}$ can be applied.

The detected proportion of the pore volume for the sample series CMnT in case 1) is then found to be 30, 44, 48, 53 %, respectively, whereas for case 2) one finds 33, 47, 49, 50 %. For both scenarios, the detected pore volume increases. This indicates a shift from macro- to mesopores within the sample with increasing deposition time, which in turn can be regarded as a hint for deposition of MnO_2 mainly on the external surface area S_{ext} of the carbon scaffold, since the interparticular pores between the carbon particles form the meso- and macropores: A deposition of MnO_2 on the particles will increase the particle diameter, and therefore will decrease the interparticular pore diameter, shifting it to a regime that is detectable by gas sorption analysis. This shift is also visible in the hysteresis of the isotherms (see inset in Figure 4.4 (b)). Compared to the bare carbon xerogel (0 h), the area enclosed by the hysteresis loop increases with increasing MnO_2 content. On the other hand, the increase in pore volume fraction detected might result from additional mesopores introduced via rough surface structures of the MnO_2-phase, too.

In order to comprehensively answer the question of the location of MnO_2, carbon xerogels of different particle size and therefore different specific external surface area, yet similar specific micropore volume, were prepared and infiltrated with MnO_2. The results of this investigation are discussed in Chapter 5.

Table 4.1 compiles the quantitative evaluation of the N_2-gas sorption data. The results for S_{ext} are determined by the t-plot method, that was described in Section 3.2.2. For the hybrid samples, however, the values for S_{ext} might be less reliable, since the Harkins & Jura isotherm, which serves

Table 4.1: MnO_2 mass uptake, sample density and structural data derived via N_2 sorption for series CMnT. All mass specific values (S_{BET}, S_{ext}, V_{mic}) are being presented normalized to the mass of the carbon xerogel, rather than the total mass of the hybrid sample. The density ρ includes carbon fibers and structural inhomogeneities of the electrodes.

sample	Δm_C [wt.%]	ρ [gcm^{-3}]	S_{BET} [m^{2}g^{-1}]	S_{ext} [m^{2}g^{-1}]	V_{mic} [cm^{3}g^{-1}]
0 h	0	0.31±0.03	786±79	191±19	0.25±0.03
4 h	63±6	0.51±0.05	595±60	195±20	0.18±0.02
10 h	90±9	0.62±0.06	404±40	207±21	0.09±0.01
16 h	118±12	0.73±0.07	357±36	190±20	0.08±0.01

as reference for the evaluation, does not necessarily apply for the $CMnO_2$ system. For the untreated carbon xerogel, the carbon particle diameter $d_{part} = 22 \pm 2$ nm can be calculated from the specific external surface area, S_{ext}, and the particle density, ρ_{part}, by using equation 3.14. The values are in good agreement with observations by SEM (Figure 4.2). Since the average particle density in the hybrid sample is unknown, the respective particle diameter can not be calculated.

The qualitative decrease in V_{mic} that was discussed above is also reflected in the respective values. E.g. for sample CMnT 16 h, only 32 % of the initial specific micropore volume is accessible to the analysis gas. For double layer capacitors, the huge surface area mainly results from micropores in the carbon xerogel. Therefore, a decrease in double layer capacitance is expected for the hybrid electrodes. The electrochemical measurements in the following section will show whether the pseudocapacitance of MnO_2 can compensate this loss.

4.2 Electrochemical Performance

4.2.1 Capacitance

Figure 4.5 (a) displays the differential gravimetric capacitance for the sample series CMnT at a potential scan rate of 1 mVs^{-1}. The red curve represents the double layer capacitance of the untreated carbon xerogel. The curve shows an almost rectangular shape, which is typical for porous carbon electrodes [21, 77]. The slight asymmetry across the measured voltage range can be attributed to a small sieving effect, that was shown by Lorrmann *et al.* to occur when ions of different sizes, i.e. Na^+ and SO_4^{2-}, are stored in the micropores of the carbon scaffold [34].

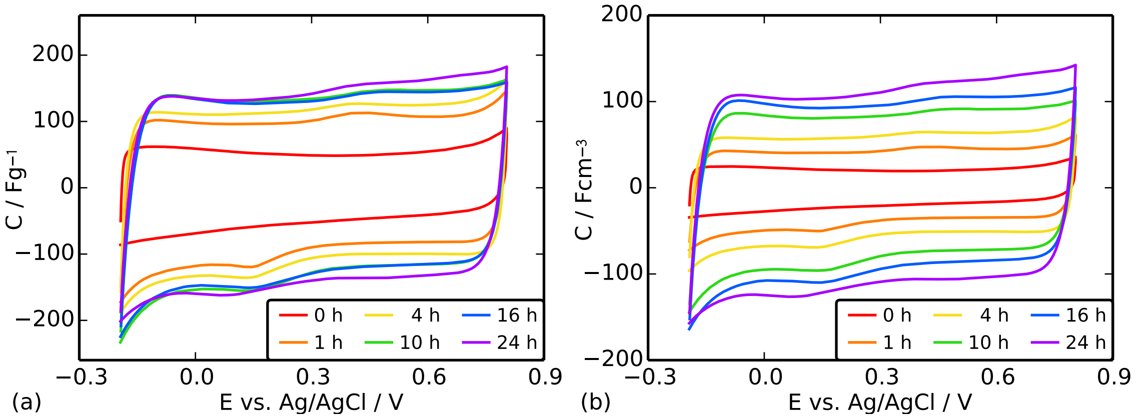

Figure 4.5: Cyclic voltammograms at 1 mV/s scan rate of the sample series CMnT, resulting from different MnO_2 deposition times, with capacitance values normalized to electrode mass (a) and electrode volume (b).

The orange curve for the 1 h sample in Figure 4.5 (a) already reveals a strong increase in capacitance, while the shape of the CV curve remains rectangular. Clearly, the loss in double layer capacitance due to the decrease in micropore volume that was discussed in Section 4.1.3 is overcompensated by the pseudocapacitance of the added MnO_2 phase.

Around 0.1 and 0.4 V vs. Ag/AgCl, shallow "bumps" appear in the voltammogram. These bumps have been identified to originate from intercalation and deintercalation of protons into the bulk of MnO_2 [66, 138]. At the turnabouts of the voltage window, around -0.2 V and 0.8 V vs. Ag/AgCl, respectively, an increase in the capacitance after the plateau can be observed. The contributions have been identified to be side-reactions, resulting from H_2O electrolysis at positive potential and irreversible Mn reduction at the negative end of the potential window [139].

With increasing infiltration time and therefore increasing MnO_2 mass uptake, the capacitance increases further and the rectangular shape is maintained, hinting for little influence of the low MnO_2 conductivity on the equivalent series resistance. After a deposition time of 10 h however, the increase in gravimetric capacitance fades. When plotting the volumetric capacitance C_{vol} of the series (Figure 4.5 (b)), the capacitance continues to increase even for long deposition times of up to 24 h.

This effect becomes even more obvious when observing the total (integral) capacitance derived from the differential capacitance by using Equation 3.3.2. When plotting the gravimetric capacitance vs. deposition time (Figure 4.6 (a)), the values saturate for deposition times longer than 10 h. This saturation, however, might lead to wrong conclusions, since the mass uptake also saturates for long deposition times, if normalized to the total electrode mass, as has been discussed in Section 4.1.1. No saturation effect is evident in the volumetric capacitance.

The gravimetric and volumetric capacitance values are plotted vs. the relative MnO_2 mass uptake, normalized to carbon mass, in Figure 4.6 (b). For C_{grav}, the artifact resulting from the normalization of the capacitance to the total electrode mass is obvious (see comments on normalization in Section 4.1.1). A linear relation is found for C_{vol}, indicating that with increasing mass uptake, equal amounts of active material contribute to charge storage.

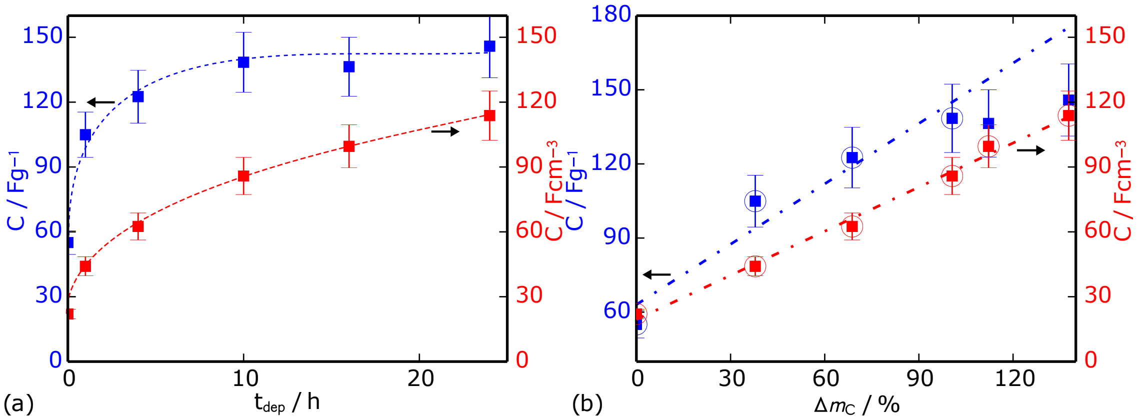

Figure 4.6: Gravimetric (blue) and volumetric (red) capacitances, calculated from CV-measurements at 1 mVs^{-1} scan rate by using Equation 3.3.2 and plotted vs. deposition time (a) and MnO_2 mass uptake (b). In Figure (a) the dashed lines act as a guide to the eye, in Figure (b) the encircled values were used for a linear fit (dash-dotted line).

When considering the volumetric capacitance vs. MnO_2 mass uptake in Figure 4.6 (b), one might expect that the largest MnO_2 mass loadings will result in the highest volumetric capacitance. However, this is only true for very slow potential scan rates and therefore long charging and discharging times, as will be revealed by the examination of the dynamic behavior of the electrodes in the next section.

4.2.2 Dynamic Behavior

In order to probe the charge and discharge performance of the electrodes, CV curves at different scan rates were measured. The capacitance retention is referred to as the capacitance at a certain potential scan rate, normalized to the value obtained at a scan rate of 1 $\mathrm{mVs^{-1}}$.

Figure 4.5 reveals that the initial slope of the CV curve at the turning points of the applied voltage does not decrease monotonously with increasing deposition time, as one might expect for an increased contact resistance with increasing MnO_2 mass uptake (see also a graph in the Appendix, Figure A.2). This trend does not arise from the electrodes themselves, but rather an increased contact resistance of the electrochemical cell due to the individual tightening of the screws is likely. Since the contact resistance has little influence at low scan rates, the values discussed earlier for the total capacitance are considered to be of high reliability. With respect to the dynamic behavior however, the samples CMnT 4 h and CMnT 16 h will be discussed in the following, since they show the lowest influence of the contact resistance in the CV curves.

The volumetric capacitances obtained for the pure carbon xerogel electrode and hybrid electrodes CMnT 4 h and 16 h for various potential scan rates are depicted in Figure 4.7 (a). Their normalized values are displayed in Figure 4.7 (b).

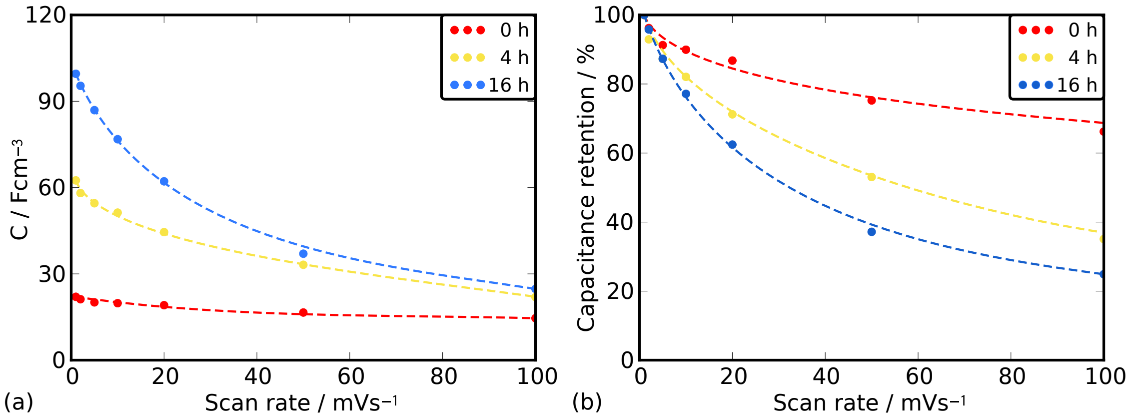

Figure 4.7: (a) Volumetric capacitance of selected electrodes of the sample series CMnT, plotted against the potential scan rate.
(b) Normalized representation of the data shown in part (a).
The dashed lines are added as a guide to the eye.

Pure carbon electrodes show a moderate capacitance retention. When the scan rate is increased from 1 $\mathrm{mVs^{-1}}$ to 100 $\mathrm{mVs^{-1}}$, about 66 % of its initial capacitance is still preserved (Figure 4.7 (b)). Since no faradaic processes are involved in the charge storage in the electrochemical double layer, the capacitance at high scan rates is mainly limited by contact- and electrolyte resistances, i.e. by the ability of ions in the electrolyte to follow the rapidly changing electrical potential [34]. Hybrid electrodes, however, show a very different behavior: Even with a low MnO_2 mass uptake of about 27 wt.%, the retention of the CMnT 1 h electrode decreases significantly faster than for the neat carbon xerogel electrode. With increasing MnO_2 content, this trend proceeds. For high scan rates above 100 mVs^{-1}, the pseudocapacitive contribution is likely to play a vanishing role and the electrodes are mainly characterized by the double-layer capacitance of the external surface area, which is about the same order of magnitude for all electrodes (see Figure 4.7 (a) and compare Table 4.1).

The reason for this behavior can be clarified by analyzing the CV-graphs for these electrodes at the respective potential scan rates (see Figure 4.8). When comparing the initial slope of the CV curves at 1 mVs^{-1} for the carbon xerogel and the hybrid sample CMnT 24 h in Figures 4.8 (a) and (b), respectively, the hybrid electrode shows a more shallow initial slope compared to the bare carbon electrode. When increasing the scan rate, the carbon electrode retains its fairly rectangular shape up to scan rates of 20 mVs^{-1}, whereas the hybrid electrode shows a strong deviation, because of the increasing influence of the equivalent series resistance (ESR, see also 3.3.3).

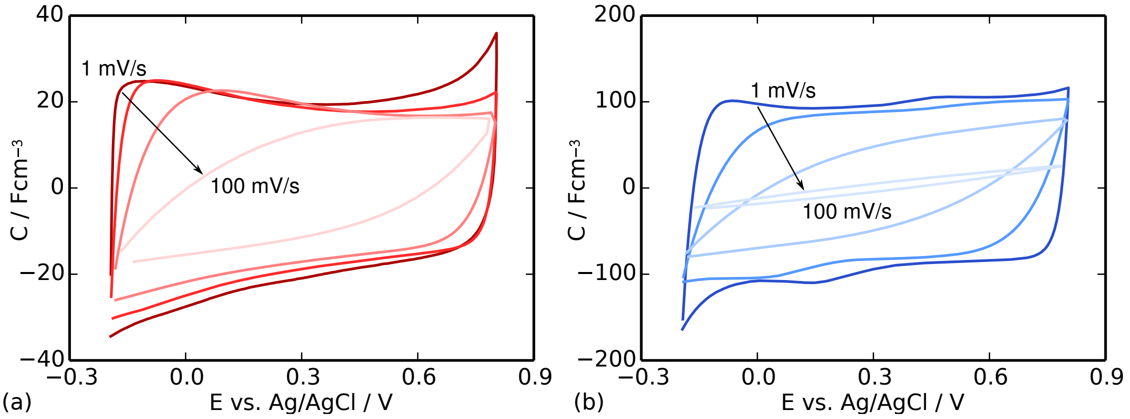

Figure 4.8: Variation of scan rate for bare carbon electrode (left) and the hybrid electrode CMnT 16 h (right).

Two key factors that influence the ESR can be cited: Firstly, the poor conductivity of the MnO_2 phase has a stronger influence at higher MnO_2 mass uptakes, presumably because MnO_2 forms substantially thick cover layers upon deposition (see Chapter 5). This macroscopic effect affects the contact resistance between electrode and current collector, which in turn influences the initial slope of the CV curve. Furthermore, on microscopic length scales, the charge transfer resistance related to the storage process of electrolyte ions in the active MnO_2 layer is increased due to longer intercalation pathways across the MnO_2 phase.

Secondly, the formation of MnO_2 deposits in the carbon xerogel (micro) structure is likely to block or narrow electrolyte pathways, as indicated by the decrease in pore volume in Section 4.1.3. Therefore, the mean free path length of the Na^+ ions within the electrode prior to finding an

MnO_2 reduction site is extended with increasing MnO_2 mass content, resulting in a slower charging behavior.

It is noteworthy that the bumps that appeared at low potential scan rates in the CV curves of the hybrid electrodes disappear towards higher scan rates, which supports the theory of ion intercalation into MnO_2 being part of the charge storage process at slow cycling rates. As will be shown in Section 5.4.2, thick layers of MnO_2 are not beneficial for high rate charge storage, since the intercalation of electrolyte ions in the bulk of MnO_2 is accompanied by large time constants. The surface reactions however occur fast enough, so that even at higher potential scan rates up to 50 mVs^{-1} a significant amount of charges is still stored within the active electrode material (see Figure 4.7 (a)).

4.2.3 Impedance Analysis

For the bare carbon xerogel electrode and the electrodes CMn 1 h, 4 h and 24 h, Figure 4.9 presents the real part $Z'(\omega)$ of the measured impedance vs. the imaginary part $Z''(\omega)$ in a Nyquist-plot. For the carbon electrode, the graph shows the behavior described in the experimental section (see Section 3.3.3): At high frequencies, the impedance curves show a shallow semicircle that can be attributed to an *RC*-element, followed by a steep increase in the low frequency branch, which is due to the double layer capacitance charging [129, 140].

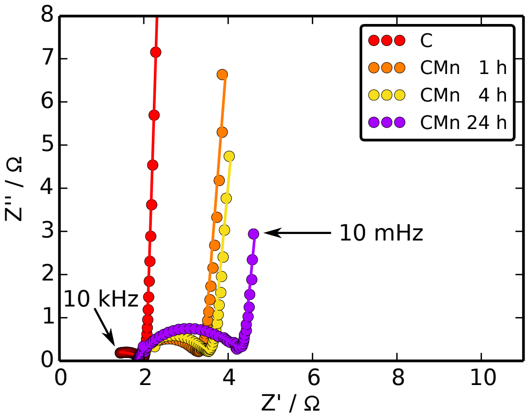

Figure 4.9: Nyquist-plot of selected electrodes of sample series CMnT. The dots indicate the experimental data points, the solid lines represent a fit using an equivalent circuit model.

Although showing a similar shape of the impedance response, the interpretation of the semicircle for the bare carbon electrode and the hybrid electrodes follows different reasoning. As described in Section 3.3.3, for the double layer capacitor, the extension of the semicircle gives a measure of the contact resistance R_c and the current collector capacitance C_c. In contrast, for the hybrid electrode, an equivalent circuit as depicted in Figure 4.10 will be employed to model the data. In order to

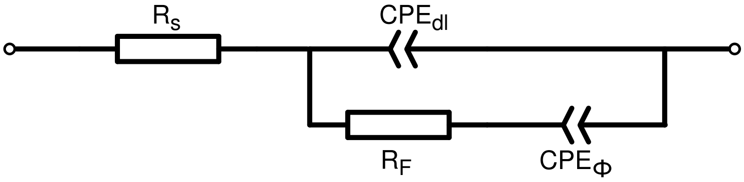

Figure 4.10: Modified equivalent circuit model for the carbon-MnO$_2$ hybrid electrode. The capacitances C_{dl} and C_{Φ} present in the idealized model (see Figure 3.11) have been replaced by constant phase elements CPE_{dl} and CPE_{Φ}, respectively.

be able to fit the measured data, the porosity of the electrodes has to be taken into account, which causes the semicircles in the Nyquist-plot do deviate from the ideal form, leading to "depressed" semicircles. This behavior can be modeled applying constant phase elements (CPE), where the capacitance is replaced by an effective impedance

$$Z_{CPE}(\omega) = \frac{1}{A\omega^n} \cdot \mathrm{e}^{(-i\, n\pi/2)}, \tag{4.4}$$

where A is the CPE magnitude and n the CPE exponent [129]. The value of n governs the nature of the CPE: For values close to 0, the CPE behaves like a resistor, whereas for values close to 1, it is more similar to a capacitance. In this model, the shift of the start of the semicircle at 10 kHz towards higher $Z'(\omega)$ indicates an increased series resistance within the hybrid electrode, whereas the extension of the semicircle to higher $Z'(\omega)$ values results from both, an increased contact resistance R_{c} and the increased charge transfer resistance R_{F}.

The model is fitted simultaneously to the real and imaginary part of the measured impedance. In Table 4.2 the values found for the respective properties are tabulated, normalized to the sample volume. The data show that R_{s} is equal for all samples, whereas R_{F} increases with increasing deposition time. This means that the contact resistance is already influenced by thin layers of MnO$_2$, as becomes obvious when comparing the start of the semicircle in Figure 4.9. With increasing MnO$_2$ mass uptake and therefore thicker layers, R_{F} increases, which might be due to longer intercalation pathways into the MnO$_2$ layer or due to a lower electrical field strength on the surface of the MnO$_2$, resulting from the low MnO$_2$ conductivity.

With increasing MnO$_2$ content the pseudocapacitance, represented by $CPE_{\Phi}\ A$, increases, as expected from CV measurements (Section 4.2.1). The capacitance values for CPE_{dl} are significantly lower for the hybrid electrodes, hinting at double-layer storage is playing a minor role. These findings are strengthened by the results from gas sorption analysis (Section 4.1.3), where major fractions of micropore volume were found to be secluded for the analysis gas, either because of filling of the micropores, or due to seclusion by an MnO$_2$ layer around the carbon particles.

Table 4.2: Overview of the MnO_2 mass uptake for the series CMnT, quantities derived from an equivalent circuit model and the simulated relaxation time τ_0.

sample	MnO_2 [wt.%]	R_s [Ω]	R_F [Ω]	$CPE_{dl}\ A$ [F]	$CPE_{dl}\ n$ [1]	$CPE_{\Phi}\ A$ [F]	$CPE_{\Phi}\ n$ [1]	τ_0 [s]
C	0	0.7	–	6.59	0.98	–	–	15
CMnT 1 h	26	1.8	1.6	0.070	0.71	12.04	0.95	59
CMnT 4 h	35	1.8	1.8	0.066	0.72	15.99	0.94	92
CMnT 24 h	55	1.8	2.5	0.084	0.68	25.87	0.94	189

It is noteworthy that the exponent of CPE_{dl} connected to the double layer capacitance is significantly lower than that of the pseudocapacitance. This again hints at the double layer capacitance being affected by the porous structure of the electrode (both carbon and MnO_2 surface), whereas the pseudocapacitance behaves more like a capacitor. This in turn speaks in favor of a surface-governed charge storage process in MnO_2, which is only slightly hindered by diffusion or intercalation effects.

Unfortunately the model is not sensitive enough to distinguish the proposed microscopic configurations, i.e. particles on the carbon surface or coated particles. In the first case, one would expect an increase in R_F because of the smaller contact area between C and MnO_2. Analogously, for coated particles, lower R_F can be expected. For the real system however, R_F, C_{dl} and C_{Φ} are expected to change with increasing mass loading. The EIS method therefore is not able to distinguish between these configurations, the physical configuration has to be determined by other methods. However, scenario 3 (see Figure 1.2) could already be excluded by SEM analysis in Section 4.1.2.

With the parameters obtained from the fit of the equivalent circuit model, the frequency behavior of the electrodes was simulated over a frequency range exceeding the experimentally available one. The results are depicted in Figure 4.11 for the real and the imaginary part of the frequency dependent capacitance, normalized to sample volume. Due to the use of the constant phase elements, the real part settles into a constant slope at very low frequencies, rather than showing a saturation, as expected for capacitances. With increasing frequency, the capacitance drops sharply and with higher mass uptake, the half-value frequency is lowered. For frequencies above 1 Hz, the capacitance faded for all electrodes under investigation.

The imaginary part of the capacitance shows a distinct maximum. For the carbon sample and the hybrid samples CMnT 1 h and 4 h, this maximum was within the experimentally accessible range, for CMnT 24 h it is only visible in the simulated data. The frequency maximum f_0 of the

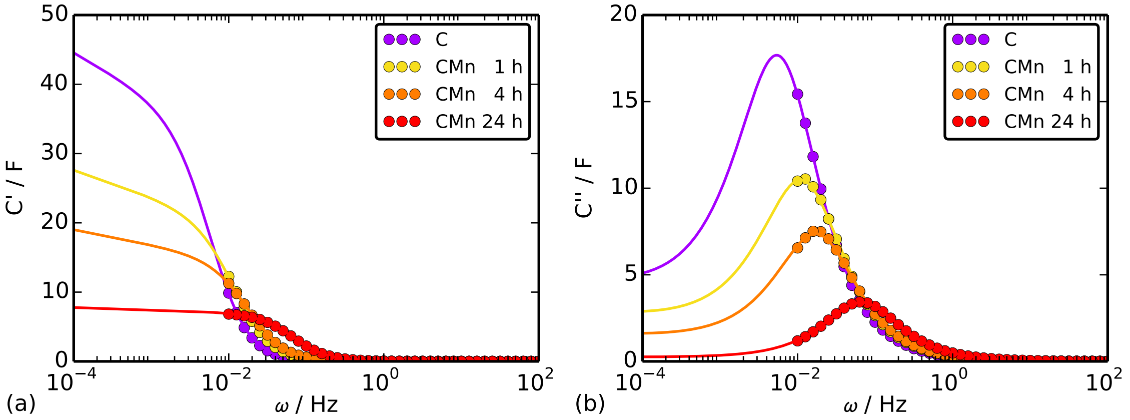

Figure 4.11: Semilogarithmic plot of the volumetric capacitance vs. frequency. The dots represent the measured data points, the solid lines are data from simulations of the equivalent circuit for the hybrid electrodes.

peak can be attributed to a relaxation time τ_0, which is a measure for the power density of the electrode [13, 15]. For the pure carbon electrode, τ_0 = 15 s, for the filled samples the values range between 59 to 189 s, for the 1 h to 24 h electrodes, respectively. This increase in τ_0 originates from both, the additional capacitance in the hybrid electrode as well as the increased ESR due to the incorporated MnO_2. Compared to the values obtained by Fischer *et al.*, these values are higher by a factor of 2, although in their study, the MnO_2 mass uptake and the specific capacitance were higher. However, Fischer *et al.* utilized thinner electrodes, and therefore the ESR might be lower than for the electrodes of the series CMnT.

4.3 Conclusion

The sample series characterized by a variation of deposition time and thus by an increasing MnO_2 content within the electrode showed the successful incorporation of MnO_2 into the carbon scaffold. The mass uptake reached values as high as 58 wt.%. However, a complete saturation of the mass uptake as reported by Fischer *et al.* could not be confirmed. Evidence was presented that the earlier reported saturation effect is likely to originate from an artifact due to the normalization procedure.

An increase in particle diameter due to the MnO_2 deposition was observed via SEM imaging for high MnO_2 mass uptakes. No separate domains of MnO_2 were found, therefore scenario 3 in Figure 1.2, i.e. separate phases of MnO_2 and carbon being present in the electrode in a significant amount, can be excluded.

The surface area and porosity analysis showed a strong decrease in the micropore volume, either due to filling or occluding of micropores upon MnO_2 deposition. The electrochemical results indicate an overcompensation of the expected losses of double layer capacitance due to the reduction of the micropore volume. The additional pseudocapacitance increases the volumetric capacitance of the electrode by more than a factor 5, however for the cost of dynamic performance. The results indicate that the 4 h sample with a relative MnO_2 mass uptake of 63 wt.% yields a good compromise between increased capacitance and dynamic performance. The time constant required to charge this electrode, however, is slowed by a factor 6 (τ_0 = 92 s) compared to the untreated carbon xerogel, which indicates both, higher capacitance and higher ESR due to the incorporated MnO_2.

The investigation provides first hints on the location of the MnO_2 within the carbon scaffold: Major deposits might be found either in the micropores of the carbon xerogel or on the external surface area. Scenarios 2 and 4 in Figure 1.2 will therefore be investigated in more detail. For this purpose, sample series of varying particle sizes were prepared and characterized. The experimental findings and their interpretation will be presented in the following chapter.

Chapter 5

Determination of MnO_2 Deposition Location

The results from the deposition time variation experiments give first hints that the MnO_2 is mainly deposited on the external surface area of the carbon scaffold (see Section 4.1.3). In order to examine this hypothesis further, carbon xerogels of different particle diameter were prepared. The samples are labeled C S, C M and C L for small, medium and large particle diameters, respectively. Fiber reinforced carbon xerogels were used for the N_2 sorption (G) and electrochemical (EC) characterization, monolithic xerogels were applied for the (A)SAXS study. The carbon xerogel was infiltrated with MnO_2 as described in Section 3.1.2. The deposition time was constant 4 h for the EC and G samples (the respective samples being denoted e.g. CMn EC/G S for the hybrid fiber reinforced sample with small particles), whereas for the scattering study, the deposition time was varied additionally. The latter samples are additionally labeled with a figure representing the deposition time, e.g. CMn S 4 corresponds to a monolithic sample with small particles and a deposition time of 4 h. The samples were subjected to the same characterization steps that were presented in Chapter 4. Additionally, the surface chemistry of selected samples was examined via XPS analysis (Section 5.2.2). An extensive (A)SAXS investigation providing a comprehensive structural model of the hybrid system was performed. The respective results are given in Section 5.3 and were published in [141].

5.1 Morphology of Electrodes

5.1.1 Surface Structure of Manganese Layer

The surface structure of the samples was probed using scanning electron microscopy (SEM). Figure 5.1 shows representative SEM micrographs of the samples used in this study. The first row displays the well interconnected network of the bare carbon xerogel backbone consisting of small (S), medium (M) and large (L) particles. Distinct inter-particular meso- and macropores can be observed [17]. The average diameter of the small, medium and large particles can be estimated from the micrographs to about 15, 40 and 400 nm, respectively. The interconnected network of meso- and macropores provides room for a reservoir of electrolyte solution, thus ensuring quick ion transport to the electrochemical double layer [34]. The good electrical conductivity of the three dimensional carbon particle network of about 70 S/cm provides excellent electronic response of the electrode material [77].

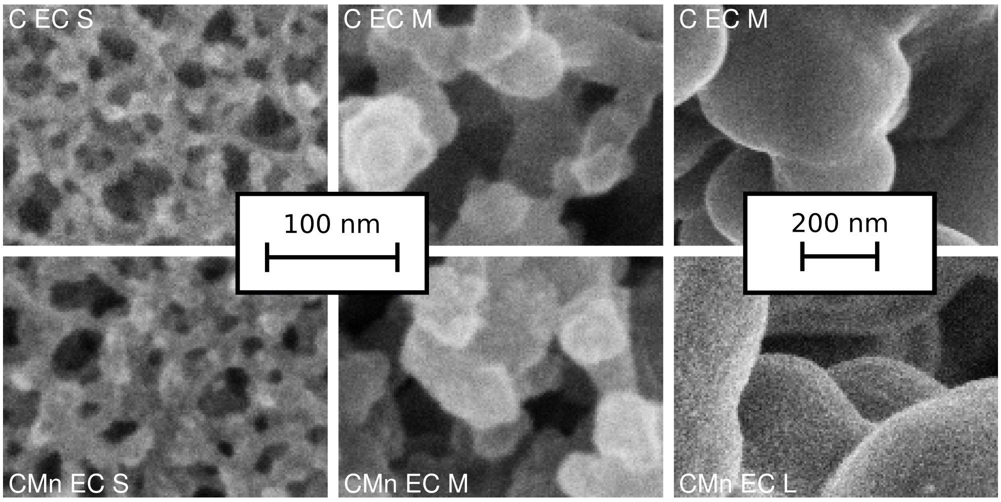

Figure 5.1: SEM micrographs showing in the upper row the carbon scaffold, consisting of well interconnected small, medium and large particles (left to right). The carbon-manganese samples in the lower row show at given resolution no significant change in the surface structure for small and medium particles after 4 h of deposition. For the large particle sample, a fine surface structure is visible. The micrographs show samples of series CEC.

The bottom row of Figure 5.1 shows the respective manganese impregnated samples, prepared by applying a deposition time of 4 h in a solution of 0.05 M $NaMnO_4$. For the CMnEC S and CMnEC M samples, no significant increase in the particle size can be observed on any length scale under investigation, when comparing them to the respective bare carbon xerogel. In particular, the well interconnected interparticular pore network remains open and accessible to electrolytic ion transport. The large particle sample, CMnEC L, seems to show some texture on the particle surface, indicating a flake- and petal structure (see also Figure 5.2), which is typical for manganese oxides

[74, 142, 143]. Because of this particular texture, the density of the MnO_2 layer is expected to be lower than the MnO_2 bulk density [141].

To gain insight into a cross section of the coated backbone structure, selected samples were cooled in liquid nitrogen and then broken into pieces. For the sample CMn L 48, Figure 5.2(a) shows a energy dispersive mapping of a cross section. Because of its higher atomic mass, the MnO_2 phase is indicated by brighter tones, while darker areas represent the carbon phase. Clearly, MnO_2 is preferentially deposited around the carbon particles, no bright spots are visible in the inner (= microporous) region of the particles. This suggests a homogeneous coating of the carbon xerogel particles with MnO_2. Figure 5.2(b) shows a MnO_2 shell, where the carbon particle has been quarried out of the shell. On the outside of the shell, the flake-structure of MnO_2 is visible, considerably more pronounced than for the sample infiltrated for 4 h, as shown in Figure 5.1. From the SEM image, the shell thickness can be estimated to be about 27 nm. However, the SEM is limited to provide insight on selected spots of the sample under investigation. Therefore, X-ray scattering methods were applied, to acquire integral information about the layer thickness (see Chapter 5.3).

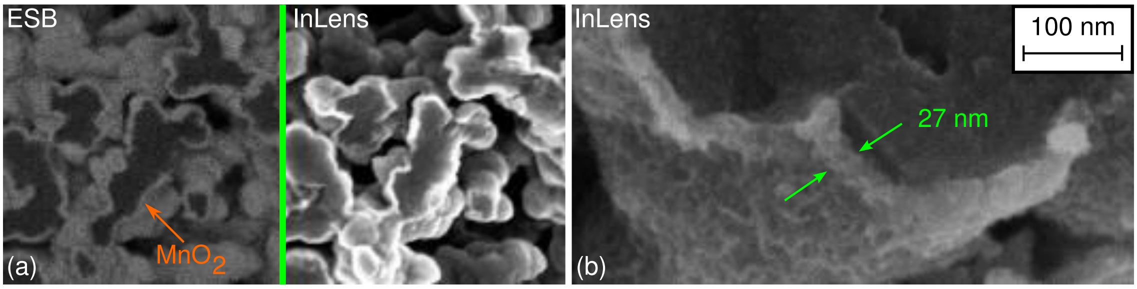

Figure 5.2: (a) Energy selective backscattering (ESB) image of a cross section of the coated carbon backbone of sample CMn L 48 (left) and corresponding image observed by the InLens-detector. Bright areas indicate MnO_2, darker areas represent carbon or pores.
(b) MnO_2 shell with the initially supporting carbon particle broken away.

5.1.2 MnO_2 Distribution

Most samples show a homogeneous distribution of MnO_2 throughout the carbon scaffold, as seen in Figures 4.2 and 5.1. In particular, no clusters of MnO_2 are found regularly. For some samples however, two types of agglomerates can be found occasionally on the macroscopic sample surface, as depicted in Figure 5.3. Sample CMn S 4 shows clusters of MnO_2 particles smaller than the carbon xerogel particles (Figure 5.3(a)). Similar clusters have been reported for sol-gel derived MnO_2 thin films and birnessite MnO_2 [58, 144]. The second type of agglomerates present are big MnO_2 grains, their sizes ranging in the micrometer regime (see Figure 5.3(b)). Presumably, these flakes represent residual undissolved MnO_2 from the precursor. Both types differ from the suggested model of MnO_2 coating the carbon backbone. Even so, these types of deposits form a minor contribution to the overall deposition, since these types are only sparsely found throughout the sample series. Furthermore, irregular deposits are exclusively found on the macroscopic surface of the electrodes, not in cross sections. Therefore, a contamination of the surface can not be excluded and the flakes might also be dust particles.

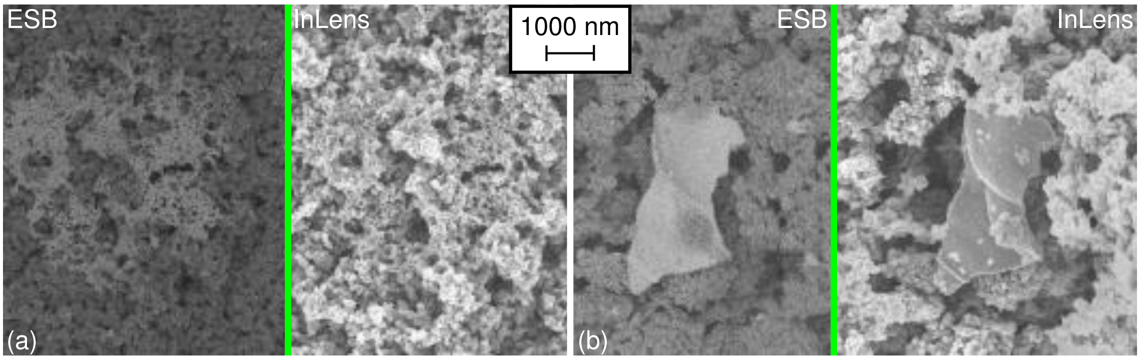

Figure 5.3: (a) ESB and InLens images of the surface of sample CMn S 4. A MnO_2 structure with particle diameters significantly smaller than the carbon particles can be observed.
(b) The image shows an example of a large MnO_2 flake, found in sample CMn S 16.

Using the EDX mode on the SEM, the distribution of Mn and C over a macroscopic cross section of the electrode was analyzed. Because of the low resolution of about 1 µm, no information on the MnO_2 layer thickness can be derived from this approach. However, the EDX mode can be applied to probe the penetration depth of the manganese precursor solution or possible gradients forming during the MnO_2 deposition (Scenario 1 in Figure 1.2). For the EDX measurements, 1 mm thick monolithic samples were impregnated for 4 h with 0.05 M $NaMnO_4$ solution and their cross sections were subjected to EDX analysis. The gray value per pixel in the images in Figure 5.4 is related to the amount of C and Mn found at this position, respectively.

The samples CMn S 4 (26 wt.% MnO_2) and CMn L 4 (17 wt.% MnO_2) of this series are shown exemplarily. For the sample CMn S 4 (Figure 5.4 (a)), a strong gradient is evident from the picture. The gray area at the bottom of the C part of Figure 5.4 (a) originates from the carbon containing adhesive tape that was used to attach the sample to the sample holder. Averaging the gray value over the picture along the cross section allows to plot the average gray value vs. the sample thickness, as shown in Figure 5.4 (b). The graph reveals an almost constant amount of Mn atoms to a certain depth, between 0.2 and 0.4 mm and 1.0 and 1.4 mm, respectively. The constant slope between 1.0 and 1.4 mm is mainly due to an uneven surface of the sample, which is also present in the C signal. After a depth of about 0.4 mm, the Mn signal ceases rapidly towards the middle of the sample. For

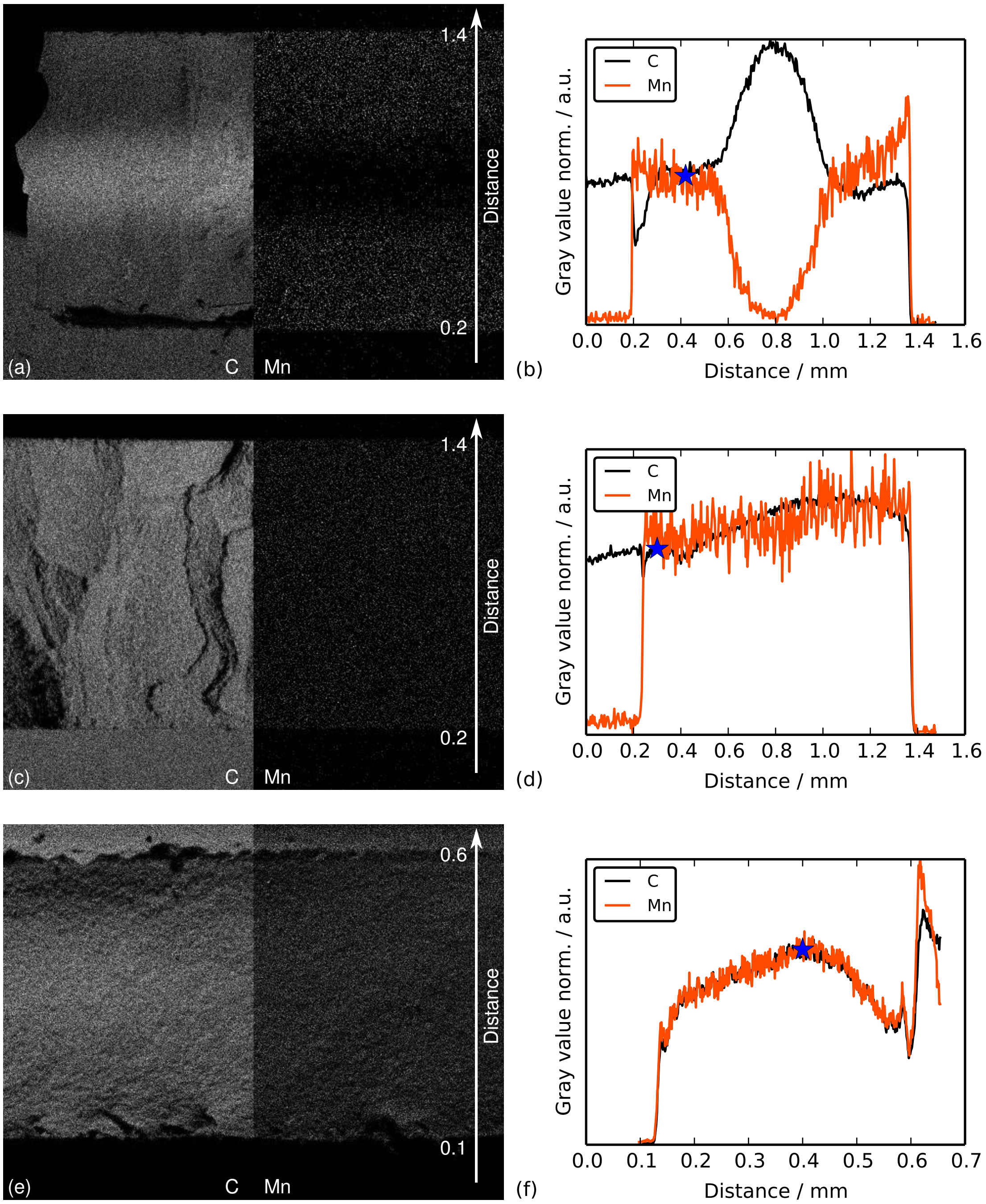

Figure 5.4: The left column shows the C and Mn distribution in cross sections of 1 mm thick discs of impregnated samples CMn S 4, CMn L 4 and CMn S 16 (0.5 mm thick) from top to bottom, respectively. The gray value represents the counts per second, found in the respective pixel, for a C or Mn peak, respectively. The average gray value for C and Mn is plotted against the thickness of the sample in the right column, normalized to the value indicated by the star marker in the respective figure, in order to stress similar behavior in absence of the Mn-gradient. Increased C counts below 0.2 mm result from the sample carrier tape. In graph 5.4 (f), the increase above 0.6 mm results from radiation originating from a plane perpendicular to the cross section (compare to the corresponding image in the left column).

the large particle sample CMn L (Figure 5.4 (d) and (e)), no gradient is found and the Mn signal is perfectly correlated with the C signal, indicating a homogeneous distribution of Mn.

Two different mechanisms can be responsible for the gradient in the samples with the small backbone particles: On the one hand, the precursor solution might be depleted of Mn in the center of the sample, since the small particle xerogels offer a large external surface area for the deposition. Between 55 and 80 % of the Mn atoms available in the solution have been deposited, depending on conversion to a composition of manganese oxides or pure MnO_2, respectively (see Section 5.2.2), indicating a strong dilution of the precursor solution. On the other hand, the pore diameter might also play an important role: in smaller mesopores, the MnO_4^- ions might hit the walls more often and be deposited than in the big pores of CMn L, where the ions diffuse further into the structure before being deposited.

From these findings it can be concluded, that after a deposition time of 4 h, the deposits coat a depth of about 0.4 mm in small particle samples. In order to ensure a homogeneous distribution of MnO_2 throughout the sample, a sample series with an electrode thickness of 0.5 mm was impregnated for the ASAXS measurements. Figures 5.4 (e) and 5.4 (f) show that for the newly prepared sample CMn S 16 (46 wt.% MnO_2) indeed no gradient across the thickness of the sample can be found. When averaging the gray value, the Mn signal is perfectly correlated with the C signal.

The quantitative evaluation of the EDX data gives, within the experimental error range, the same trends as the mass uptake determined macroscopically from the weight changes.

It is noteworthy, that the results derived from the EDX analysis strongly depend on the chosen emission line. Investigations on the sample series prepared for the ASAXS measurements, performed by analyzing the Mn contribution from the Mn K line, always resulted in "white noise", whereas the evaluation of the Mn L line yielded good correlation with the C signal. The reason for this effect can be found in the mean free path of photons when crossing the MnO_2 layer: the high-energy K-photons (E_K^{Mn} = 6.539 keV [117]) have a two orders of magnitude lower attenuation coefficient ($\mu_K = 2.094 \cdot 10^2\ cm^{-1}$) than the low-energy L-photons (E_L^{Mn} = 0.769 keV, $\mu_L = 5.658 \cdot 10^4\ cm^{-1}$ [117]). Accordingly, the free path $\ell \propto \mu^{-1}$ for the K-photons two orders of magnitude longer and the K signal contains contributions from deeper layers of the sample, resulting in a uniform gray value. Therefore, evaluating the L-photons makes the method more surface sensitive.

5.1.3 Crystal Structure

As already stated in Section 2.2, the crystal structure of the active MnO_2 material has a major influence on its electrical and ionic conductivity and therefore the electrochemical performance of the hybrid electrode. In order to determine the crystal structure of the samples, X-ray diffraction (XRD) spectra were measured with a powder spectrometer. However, the spectra exhibited a high amount of noise due to the low scattering intensity of the samples, mainly because of the rough sample surface and poor crystallinity of the MnO_2. Even with big apertures of 1 mm at the detector and long integration times of up to 30 s per 0.1°, the spectra showed a very low signal to noise ratio. Therefore, the wide angle X-ray scattering (WAXS) data that were recorded upon SAXS measurements were evaluated instead.

Figure 5.5 exemplarily shows the scattering for the sample series CMn M. The scattering cross section is normalized to the sample mass. The scattering vector q from the SAXS experiment was converted to the scattering angle 2θ using the relation $2\theta = 2\arcsin(q \cdot \lambda/4\pi)/2\pi \cdot 360°$, where λ is the Cu K_α wavelength of 1.542 Å [117]. This conversion allows direct comparison of the WAXS data with literature data that was collected by applying a Cu K_α X-ray source.

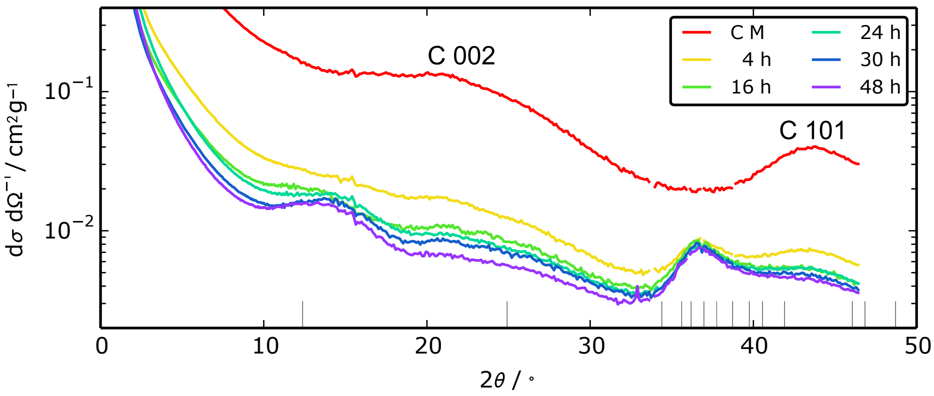

Figure 5.5: Semilogarithmic plot of the WAXS-pattern of the samples from series CMn M. The vertical lines at the bottom indicate the theoretical scattering peaks of a birnessite structure.

The scattering of the pure carbon sample C M exhibits two broad peaks at 2θ = 21.5 and 43.8°, corresponding to the carbon 002 and 101-peak, respectively [145, 146]. As expected, the WAXS characteristics is independent of the particle size (see Figure A.5 in Appendix A).

Within each particle size series, the corresponding hybrid samples show the same trends, therefore series CMn M will be discussed exemplarily (Figure 5.5). In the WAXS data, the carbon peaks remain visible in the spectra of the hybrid samples, even at high MnO_2 mass uptakes. Additionally, broad peaks evolve around 2θ = 14° and 37°.

In order to compare the experimental data to potential MnO_2 phases, the theoretical spectra of birnessite, pyrolysite, ramsdellite and hollandite were calculated. In Figure 5.5, the theoretical birnessite peak positions are indicated by vertical lines at the bottom of the figure, using the C2/m space group with the unit cell dimensions a_0 = 5.1750 Å, b_0 = 2.8500 Å, c_0 = 7.3970 Å and

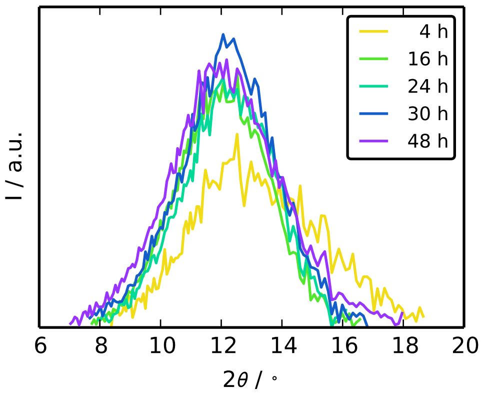

Figure 5.6: Detail of the birnessite 001-peak for the sample series CMn M. The data are corrected for a linear background.

β = 103.180° [147, 148]. A comparison with the other potential configurations revealed the birnessite configuration to be present in the samples. The peak around 14° can be related to the birnessite 001 peak at 12.38°, after the superimposed background is removed (see Figure 5.6) [147, 149]. The birnessite 002 peak is superimposed by the carbon 002 contribution. From 34 to 42°, the birnessite spectrum shows a group of peaks, which in combination form the broad peak located around 37° in the experimental spectrum.

The peaks of the sample series related to the birnessite 001 peak are shown in detail in Figure 5.6, corrected for the superimposed background. The CMn M 4 h peak exclusively shows a pronounced asymmetry, which is generally attributed to mechanical strain in the crystal structure. With increasing deposition time, the MnO_2 peaks grow from 4 h to 16 h, then the signal saturates, as does the width of the peak. This hints for an initial growth of MnO_2 crystallites, whereas for longer times the size saturates. From the position of the peak, the Bragg layer spacing can be calculated using Equation 3.19. The average value for all samples yields 0.68±0.05 nm, in good agreement with literature value of 0.7 nm reported for birnessite [73, 150].

Comparing the spectra for the different carbon particle sizes at comparable MnO_2 mass uptakes, differences exclusively appear for the MnO_2 001 peak (see Figure A.6 in Appendix A). This peak appears at slightly larger angles for the samples of the CMn L series, hinting for a smaller inter-layer distance in the MnO_2 crystallites.

From these findings, the MnO_2 structure can be identified to be of the birnessite type. According to the literature, the bulk density of MnO_2 therefore can be estimated to be 3.0 g/cm^3 [151]. This value will be used for the calculation of the MnO_2 layer thickness in Sections 5.2.1 and 5.3.

For bulk MnO_2 electrodes, the $1 \times \infty$ layers (see Figure 2.4) of birnessite are regarded superior to other configurations for electrochemical charge storage, since they yield high capacitances through proton or small ion insertion into the inter-layer space [75, 152]. For example, Ghodbane *et al.* found a nearly doubled gravimetric capacitance for birnessite MnO_2 compared to ramsdellite MnO_2, which provides a 1x2 tunnel structure (see Figure 2.4) [152]. The low intrinsic electronic conductivity of $58{\cdot}10^{-7}$ Scm^{-1} [152] for birnessites is expected to show little influence on the hybrid electrode performance when a thin layer of MnO_2 is deposited on a carbon surface.

5.1.4 Surface Area and Porosity

In order to quantify the microscopic surface area, particle sizes and porosity, the samples were investigated using N_2 gas sorption at 77 K. The resulting isotherms for the bare carbon xerogels are shown in Figure 5.7, with the data being normalized to the mass of the carbon xerogel. The general form of the isotherm allows to compare samples qualitatively, showing the typical shape of microporous materials [17, 93]. The discussion will be exemplarily conducted for sample CG S in Figure 5.7.

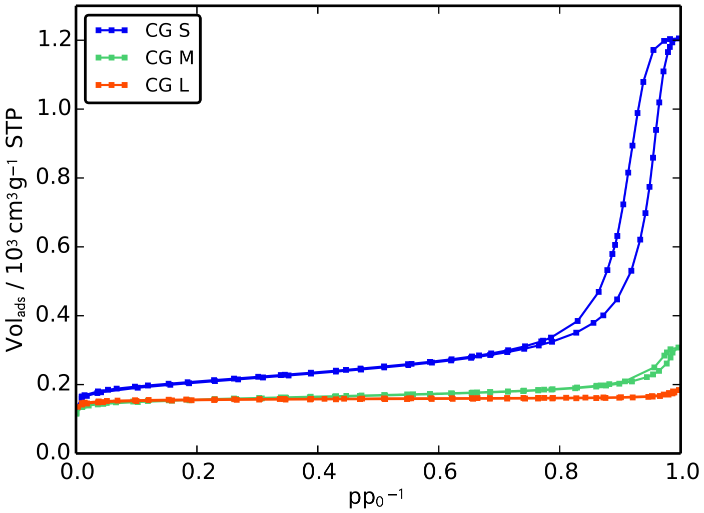

Figure 5.7: N_2 gas sorption isotherms of the carbon scaffold for the three different carbon xerogel (CG) particle sizes (small (S), medium (M) and large (L)). The data are normalized to the carbon xerogel mass.

For relative pressures $pp_0^{-1} < 0.1$, the gas volume adsorbed shows a sharp increase, which generally is attributed to the filling of the micropores in the sample. This feature is almost identical for all three samples (S, M and L), indicating a comparable micropore volume. In the intermediate relative pressure range, the adsorption takes place on the external surface area of backbone particles of the xerogel. The slope declines from sample S to L, showing the systematic decrease of external surface area which corresponds to the desired increase of carbon backbone particle sizes in this series of carbon xerogels. For relative pressures above 0.8, a hysteresis loop is observed, which can be related to condensation and evaporation of N_2 in mesopores. The hysteresis loop is more pronounced for sample S and its enclosed area decreases for larger particles, hinting at a shift in inter-particular pore size from meso- to macropores and thus to a regime that is not detectable by N_2 sorption [93].

The quantitative evaluation of the sorption data was performed using the equations presented in Section 3.2.2. The data for S_{ext}, S_{BET}, V_{mic} and mean particle diameters are compiled in Tables 5.1 and 5.2 for EC and ASAXS-samples, respectively. The isotherms for the carbon xerogel samples which are additionally investigated by ASAXS measurements can be found in Appendix A, Figure A.1. For the errors in the calculation of surface area, the error in determining the fiber content is the main factor, amounting to 10 % for all samples. The decrease in S_{ext} from 308 over 75 to 9 m^2/g for samples CG S, CG M and CG L, respectively, confirms the successful variation in S_{ext} while keeping V_{mic} approximately constant. Direct calculation of the diameter of the carbon backbone particles via Equation 3.14 shows an increase from about 12 to 462 nm with decreasing S_{ext} (Table 5.1).

For the monolithic samples (ASAXS series, Table 5.2), the values for ρ, S_{BET} and V_{mic} show a more narrow distribution. However, samples C S and C M of this series exhibit very similar S_{ext} and therefore d_{part}, showing that the variation of external surface area in this case did not succeed as desired. Nevertheless, the samples were impregnated with MnO_2 and subjected to ASAXS measurements, in order to confirm the reproducibility of the experiment.

Comparing the samples between the two series, sample CG M of the gas sorption series equals samples C S and C M of the ASAXS-series. The CG L sample of the gas sorption series exhibit a smaller S_{ext} and therefore larger particles than the C L sample prepared for the ASAXS-series.

Figure 5.8 shows the influence of the MnO_2 deposition on the N_2 isotherms for samples prepared for gas sorption measurements (G-series). When the data are normalized to the total sample mass (left column of Figure 5.8), the isotherms show a decrease in adsorbed volume in the medium pressure range that is in the order of the weight percentage of the deposited MnO_2, which is 48, 29 and 3 wt.% for small, medium and large particle samples, respectively. When normalized to the carbon xerogel content, the isotherms overlap in the range of experimental error (right column of Figure 5.8). Therefore, assuming a negligible additional contribution to the micropore volume through MnO_2 (see Section 4.1.3), no substantial fraction of pore volume of the carbon backbone detectable by N_2 sorption was secluded or filled with MnO_2, the material deposited is rather contributing solely to the sample mass. Together with the evidence from the energy dispersive SEM micrographs shown in Figure 5.2, a deposition of a substantial amount of MnO_2 in the micropores of the carbon particles seems unlikely.

In contrast to the series of deposition time variation CMnT presented in Section 4.1.3, less micropore volume is inaccessible to the analysis gas after MnO_2 deposition. Comparing the particle diameters shows that the particles of the series C G are all larger. Therefore, series CMnT exhibited

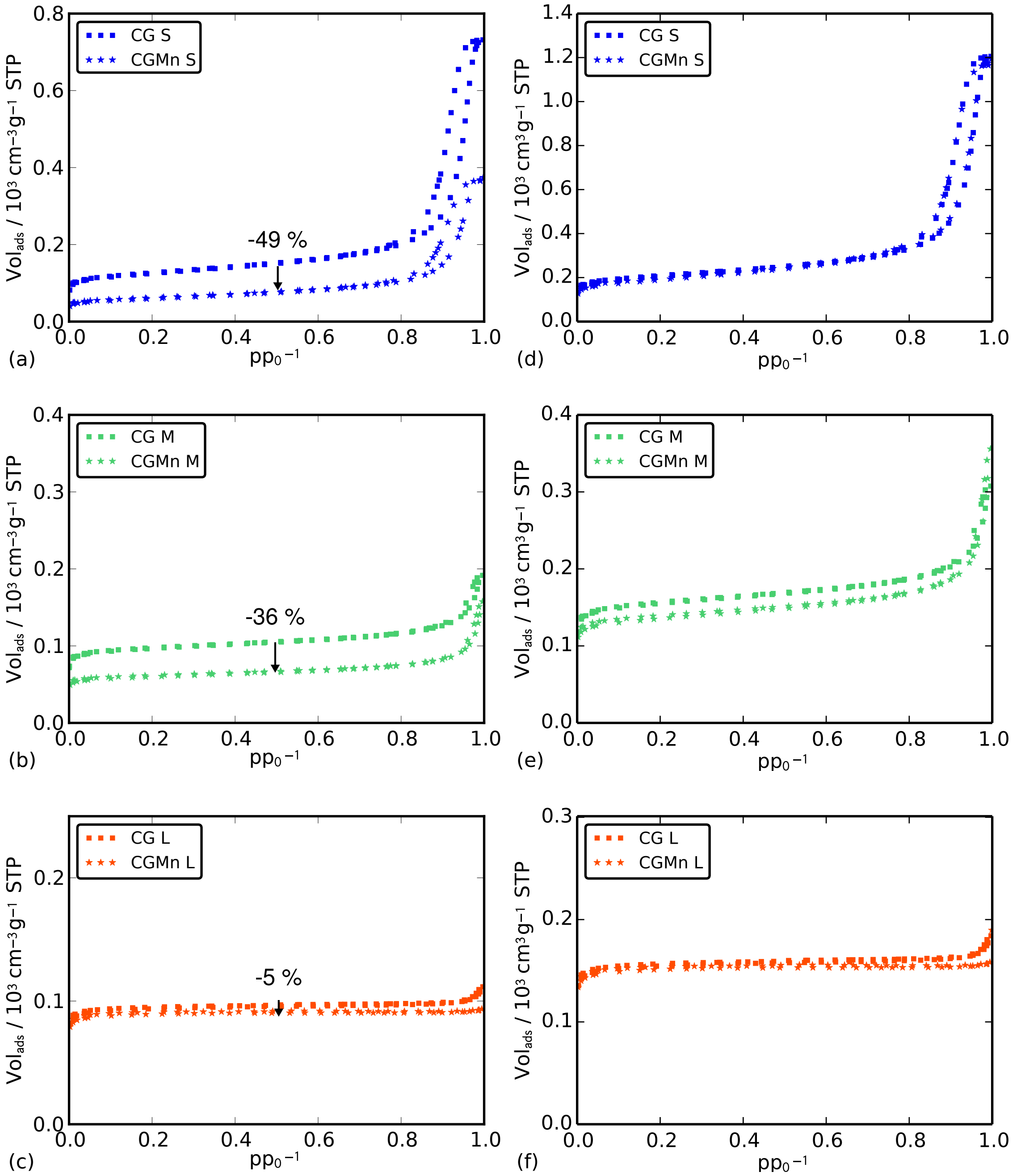

Figure 5.8: N_2 sorption isotherms for samples S, M and L, comparing bare carbon structure (CG, square marker) with MnO_2-filled sample (CMnG, star marker). The data in the left column (a-c) are normalized to the total sample mass, the data in the right column (d-f) are normalized to the carbon xerogel mass.

a larger fraction of micropores that were very close to the enveloping surface area of the particles. These first layers of micropores might have been filled or secluded with MnO_2, hindering diffusion of the precursor deeper into the particle. For larger particles however, a larger fraction of micropores is still accessible for the N_2 gas (see Table 5.1).

The quantitative evaluation of the sorption data for the hybrid samples reveals an increase in S_{ext} for samples CMnG S and CMnG M, when compared to the respective untreated samples (see Table 5.1). Sample CG L does not show this trend, however it has to be noted that for mainly macroporous samples or samples with very large particle diameters, the evaluation of S_{ext} is highly erroneous. The particle diameter of the hybrid samples can not directly be calculated using Equation 3.14, since the particle density ρ_{part} is experimentally inaccessible via N_2 sorption for the two-phase particle. Future experiments applying Hg pygnometry might be able to resolve this issue, since the total pore volume, including macropores, can be measured. From the SEM micrographs in Figure 5.2, an increase in particle diameter due to the MnO_2 deposition was expected. Since for larger particles a smaller S_{ext} is expected, the increase in S_{ext} for the hybrid samples is suspected to originate from the surface structure of MnO_2, as evident in Figure 5.2(b).

Analogously to the steps described in Section 4.1.3, the pore volume fraction detected by N_2 sorption analysis can be evaluated (see page 47). The results are compiled in Table 5.3.

The fact that even for sample CG S only 50-57 % of the total pore volume were detected, indicates either a huge amount of macropores, originating from cracks and fissures, or large mesopores, that are just out of the detectable range (> 40 nm) [93]. Since SEM did not reveal major inhomogeneities on the sample, the latter is more likely. For samples CG M and CG L, macropores also originate from the interparticular pores of the larger particles.

Consistent with the findings for series CMnT, for both cases, the volume detected for the respective sample increases upon MnO_2 deposition. Again, the interpretation of this behavior leaves two possibilities: Firstly, large MnO_2 deposits might have formed in the macropores. However, the SEM overviews showed no evidence for this interpretation (see Section 5.1.1). In fact, SEM revealed that the carbon particles are coated by a layer of MnO_2 thus narrowing the pores and shifting the pore volume from the macropore- to the mesopore regime. Therefore, the increase in mesopore volume detected is a strong hint for deposition of MnO_2 on the external surface area of the carbon xerogel backbone.

It is noteworthy that for the hybrid samples, the ratio of detected pore volume seems to be independent on whether the micropores were filled with MnO_2 or not. However, compared to the findings for series CMnT, the mass loadings were quite low, so the rather small difference might not be detectable for these samples.

To summarize, the N_2 gas sorption measurements revealed a successful variation of the external

Table 5.1: Overview of structural data derived for the fiber reinforced carbon xerogels used for N_2-gas sorption measurements, as well as the corresponding hybrid samples (series CMnG). Mass specific values are normalized to the mass of carbon xerogel, the density ρ includes fibers and structural inhomogeneities in the electrodes.

sample	MnO_2 [wt.%]	ρ [gcm^{-3}]	S_{ext} [m^{2}g^{-1}]	S_{BET} [m^{2}g^{-1}]	V_{mic} [cm^{3}g^{-1}]	d_{part} [nm]
CG S	0	0.37±0.04	308±31	751±75	0.18±0.02	12±1
CG M	0	0.32±0.03	75±8	601±60	0.21±0.02	53±6
CG L	0	0.23±0.02	9±6	623±62	0.24±0.02	462±49
CMnG S	44±4	0.69±0.07	358±36	685±69	0.14±0.02	–
CMnG M	29±3	0.42±0.04	81±8	527±53	0.18±0.02	–
CMnG L	3±1	0.24±0.02	1±5	611±61	0.24±0.02	–

Table 5.2: Overview of structural data derived for the monolithic carbon xerogels used for ASAXS measurements (series CMn S,M,L). Mass specific values are normalized to the mass of carbon xerogel, the density ρ includes structural inhomogeneities in the electrodes.

sample	MnO_2 [wt.%]	ρ [gcm^{-3}]	S_{ext} [m^{2}g^{-1}]	S_{BET} [m^{2}g^{-1}]	V_{mic} [cm^{3}g^{-1}]	d_{part} [nm]
C S	0	0.53±0.02	75 ±8	675±68	0.24±0.02	55±5
C M	0	0.49±0.05	70 ±8	690±69	0.24±0.02	59±5
C L	0	0.43±0.04	16 ±6	697±70	0.27±0.03	263±25

Table 5.3: Comparison of ratio [%] of probed total pore volume, following the two cases of accessible or inaccessible micropores as described in Section 4.1.3.

	CG S	CG M	CG L	CMnG S	CMnG M	CMnG L
accessible	50	11	4	61	13	5
inaccessible	57	12	5	62	14	5

surface area S_{ext} of the carbon xerogel. Due to MnO_2 deposition, a smaller amount of V_{mic} is secluded or filled compared to the samples investigated in Chapter 4, presumably because the fraction of micropores close to the particle surface is smaller for larger particles. Together with the SEM results (Section 5.1.1), a deposition of MnO_2 mainly on the external surface area is likely.

5.2 Chemical Composition

5.2.1 MnO_2 Mass Uptake

Figure 5.9 shows the MnO_2 mass uptake (Equation 4.1) vs. the deposition time for the samples prepared for the particle size variation series. The graph shows the values for the small (S), medium (M) and large (L) particle samples in blue, green and orange markers, respectively. For the ASAXS measurements, a variation of deposition time was performed additionally to the variation in particle size (series CMn S,M,L). The respective relative mass uptake is represented by star markers in Figure 5.9. The samples CMnEC (square marker) and CMnG (diamond marker) were infiltrated for 4 h for the use in electrochemical- and gas sorption measurements, respectively. In the range of experimental error, the corresponding samples of these sub series show the same relative MnO_2 mass uptake.

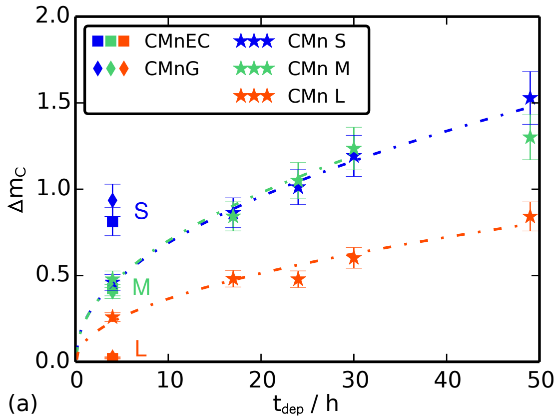

Figure 5.9: The graph shows the relative MnO_2 mass uptake vs. the deposition time of the sample series CMnEC, CMnG and CMn S,M,L. The lines act as guide to the eye, however represent a $\sqrt{t}$-fit, as discussed in Section 4.1.1.

At given deposition time, the samples, e.g. series CMnEC, take up different relative amounts of MnO_2, although subjected to the same infiltration conditions (1 M $NaMnO_4$ for 4 h, see also Section 3.1.2). The relative mass uptake strongly correlates with the particle size, with the small particles showing the highest MnO_2 uptake of up to about $\Delta m_C = 1.5$, whereas for the sample CMnEC L a value of 0.02 is found. These results provide strong evidence for the assumption of MnO_2 being mainly deposited on the external surface area of the carbon scaffold.

As already mentioned in Section 5.1.4, the particles in the L samples of series CMn EC/G are about 1.8 fold larger than the ones in the series CMn L. Consequently, the MnO_2 mass uptake for sample CMn EC/G L is significantly lower than for sample CMn L 4 h. It was also shown that the external surface area of series CMn S and CMn M is comparable, which leads to a comparable MnO_2 mass uptake: Within the range of experimental error, the samples CMn S and CMn M show the same MnO_2 mass uptake over all measured deposition times. An exemption to his behavior is sample CMn M 48, where the mass uptake is significantly lower than for CMn S 48. Most likely, a depletion of the $NaMnO_4$ precursor solution occurred. If a molar conversion from $NaMnO_4$ to MnO_2 is considered, all Mn atoms available in the precursor solution will have been consumed for the samples CMn S 48 and CMn M 48.

Within each particle size series, the relative mass uptake as function of deposition time is comparable to series CMnT discussed in Chapter 4, with a steep increase in mass uptake for short deposition times $t_{\mathrm{dep}} < 4$ h and a monotonous uptake rate for longer times, that can be fit with a $\sqrt{t_{\mathrm{dep}}}$ behavior.

Using the data from the gas sorption measurements presented in Section 5.1.4, the MnO_2 mass uptake can be plotted vs. the external surface area of the carbon scaffold. This is exemplarily done for the series CMnG in Figure 5.10. The blue curve confirms a strong correlation of the MnO_2 mass uptake with the external surface area and therefore particle size. The large particles, having the smallest S_{ext}, show the lowest MnO_2 uptake and vice versa. However, the ratio $\mathrm{m}_{\mathrm{MnO_2}}/S_{\mathrm{ext}}$ is not constant, as would be expected for a purely self-limiting process.

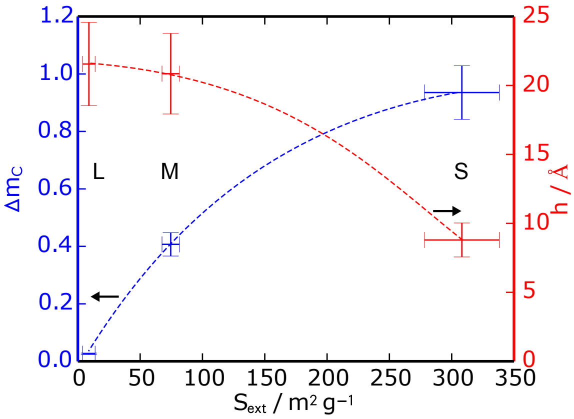

Figure 5.10: MnO_2 mass uptake of series CMnG (blue) and calculated MnO_2 layer thickness (red) vs. the external surface area. The dashed lines represent a guide to the eye.

Assuming that the entire mass of MnO_2 introduced into the system is deposited on the external surface area of the carbon xerogel scaffold, the MnO_2-layer thickness h_{m} can be estimated using the MnO_2 bulk density $\rho_{\mathrm{MnO_2}} = 3.00\ \mathrm{gcm^{-3}}$ [151]:

$$h_{\mathrm{m}} = \frac{m_{\mathrm{MnO_2}}}{m_{\mathrm{C}}} \cdot \frac{1}{\rho_{\mathrm{MnO_2}} \cdot S_{\mathrm{ext}}}. \qquad (5.1)$$

The resulting layer thickness is represented by the red curve in Figure 5.10. As one can see, the L-sample taking up the least MnO_2, yields the thickest MnO_2 layer of about 21 Å. SEM analysis (Section 5.1.1) of samples with a deposition time of 48 h confirms thicker layers of MnO_2 with increasing particle diameter. The hypothesis of MnO_2 deposition on the external surface area of the carbon backbone with the calculated layer thickness therefore seems reasonable. However, for the samples with a deposition time of 4 h, no MnO_2 layer is visible in the SEM images, presumably because of the limited resolution of the SEM. The ASAXS-investigation presented in Section 5.3 provides an alternative experimental approach to determine the thickness of the MnO_2 layer. The results of the electrochemical characterization (Section 5.4) will show the influence of the MnO_2 layer on the electrode performance.

5.2.2 Chemical Composition of MnO_2 Phase

XPS spectra were recorded in order to verify a comparable chemical composition of the different composite samples. Spectra were recorded for samples CMnEC S, CMnEC M and CMnEC L, the same samples that were used for electrochemical measurements, and for the bare carbon CEC S. The structural data for this series are compiled in Table 5.1. Figure 5.11 shows the overview spectra for CEC S, CMnEC S and CMnEC M. The intensity of the spectra is normalized to the C 1s peak and shifted vertically for clarity. For the pure carbon, only the O 1s and the C 1s peaks are visible at 532 and 285 eV, respectively. The oxygen contribution is related to surface groups on the surface of the carbon xerogel backbone.

The spectra of the composite samples are all very similar. The positions of corresponding peaks are found at the same energy, indicating identical chemical composition for both samples. However, the Mn-related peaks are higher for sample CMnEC S, correlating with the higher relative mass uptake for this sample.

Both XPS spectra of the composite samples exhibit a pronounced Na 1s peak at 1072 eV, indicating residual sodium that has not been washed out in the cleansing step after MnO_2 deposition. A series of peaks around 980 and 855 eV originates from O KLL and Mn LMM Auger-electrons, respectively. The bump at 775 eV can be identified as the Mn 2s level. The Mn 2p level between 600 and 700 eV shows a strong splitting because of spin-orbit coupling: since the total momentum j is the sum of orbital angular momentum l and electron spin s: $j = l + s$, there are two possible states for j if $l > 0$ [107]. Therefore, for Mn 2p one finds $j = 1 - 1/2 = 1/2$ at 655 eV and $j = 1 + 1/2 = 3/2$ at 643 eV. The O 1s peak at 530 eV shows a dramatic increase compared to the pure carbon sample. However, this is not surprising, since the deposition of MnO_2 from $NaMnO_4$ introduced additional oxygen atoms. The inset shows higher discrete energy states, for manganese up to 3p. The valence states of Mn 3d and O 2p vanish in the valence band at energies above 10 eV.

Figure 5.12 (a) shows a detailed measurement of the $Mn2p_{3/2}$-peak for the three composite samples investigated. The individual peaks are normalized to the respective maximum value. In the range of experimental error, the curves are identical. As a consequence, the samples can be

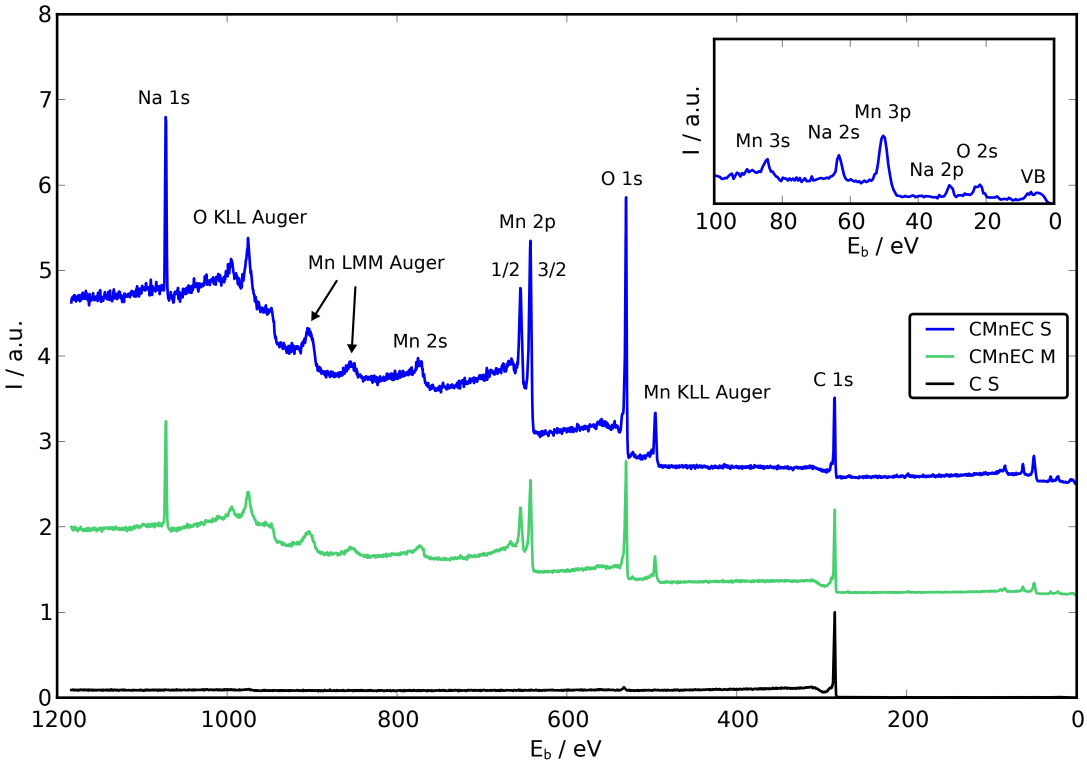

Figure 5.11: Overview of the XPS spectra for untreated carbon CEC S and composite samples CMnEC S and CMnEC M, as a function of the electron binding Energy E_b. Intensities are normalized to the C1s peak and shifted for clarity. The inset shows the magnified range from 100 to 0 eV for sample CMnEC S with states up to the valence band (VB). The peaks are identified according to the values in [153, 154].

regarded as chemically identical.

In order to evaluate the chemical composition of the Mn-containing phase, the $Mn2p_{3/2}$ peak was fitted with four Gauss-peaks according to Equation 3.18. The fit is shown exemplarily for CMnEC M in Figure 5.12 (b). The four Gauss-contributions were identified to represent $NaMnO_4$, Na_2MnO_4, MnO_2 and Mn_2O_3 [153, 155, 156].

Figure 5.13 shows the fraction of the four Mn-containing species in the $Mn2p_{3/2}$-peak. Sample CMnEC S was measured twice and therefore the difference in results provides a measure for the experimental error, which can be estimated to be about 5 %. In the range of this error, all samples show the same composition with regard to $NaMnO_4$, Na_2MnO_4, MnO_2 and Mn_2O_3.

As described in Section 2.2, only Mn(IV) is electrochemically active, Mn in other oxidation states is increasing the mass of the resulting electrode without contributing to charge storage [61]. Figure 5.13 reveals that at a deposition time of 4 h, the samples prepared only contain 50 % of the electrochemically active species MnO_2. For future applications it is therefore necessary to remove the residual $NaMnO_4$ and Na_2MnO_4 during the cleansing step more efficiently. Furthermore, changing the deposition approach can lead to very pure manganese oxide deposits: electrodeposition offers the opportunity to control the oxidation state of the MnO_x deposited [58, 157, 158].

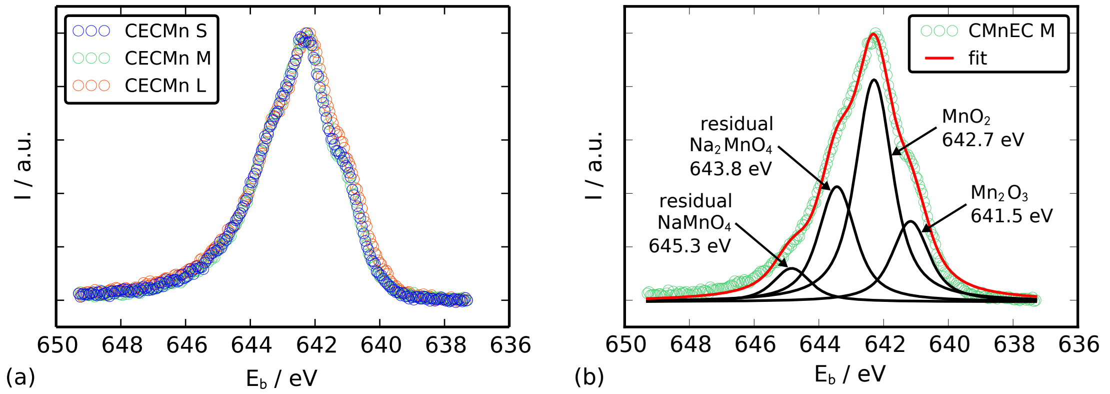

Figure 5.12: (a) Detailed XPS analysis of the $Mn2p_{3/2}$-peak for the different composite samples of series CMnEC. The data are normalized to the maximum value for each measurement.
(b) Modeling of the peak of sample CMnEC M, according to [155, 156].

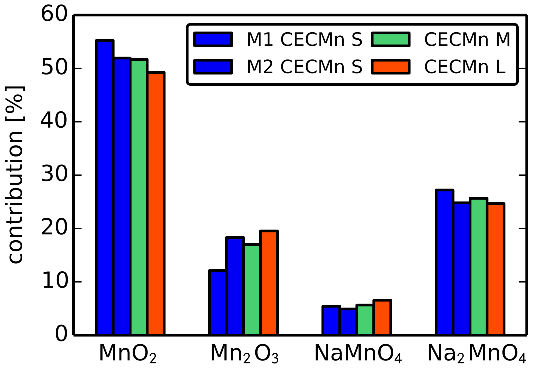

Figure 5.13: Contribution of Mn oxidation states to the Mn2p peak in the XPS spectra. Sample CMnEC S was measured twice in order to get an estimate for the reproducibility of the values.

5.3 Hollow Sphere Model and MnO$_2$ Layer Thickness

In order to further quantitatively resolve the microscopic structure of the CMn hybrid samples, small angle X-ray scattering (SAXS) and anomalous small angle X-ray scattering (ASAXS) measurements were performed. For these measurements, monolithic carbon xerogel samples were prepared and infiltrated with MnO$_2$ according to the steps described in Section 3.1.2 (sample series CMn S,M,L).

Figure 5.14 (a) shows the differential scattering cross section of the bare carbon xerogel monoliths at an energy of the incident beam of 12 keV. For all samples, the scattering cross section decays at low q-values ($q < 1$ nm^{-1}) according to a power-law with an exponent of about 4 (see also Figure 5.14 (b), scattering cross section multiplied by q^4). This region is referred to as "Porod-region", which generally is attributed to a smooth external surface area of the carbon scaffold [93, 159]. At q-values larger than 1 nm^{-1}, a distinct "micropore-shoulder" is visible [93].

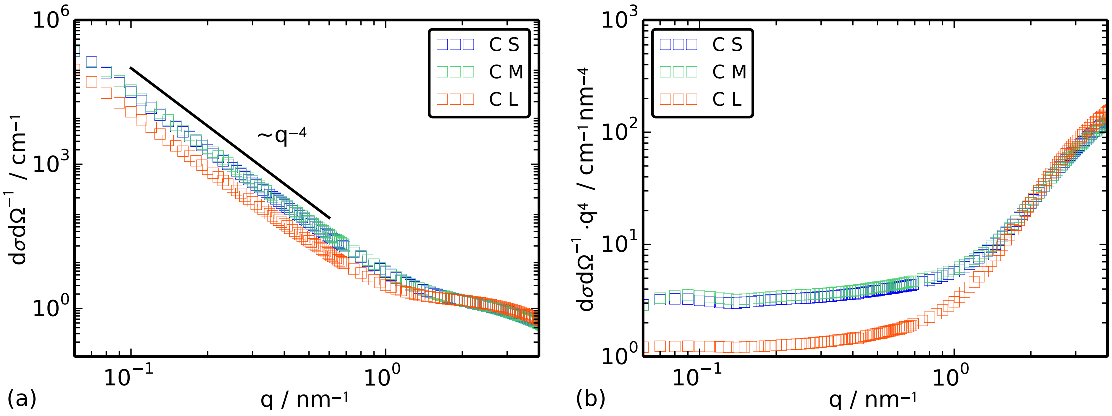

Figure 5.14: (a) SAXS cross section for carbon samples C S, C M and C L. The data are normalized to the sample volume illuminated by the X-ray beam. (b) Same scattering cross section, however multiplied by q^4.

This plot reveals that the samples C S and C M show a very similar scattering curve, indicating identical micro-structural properties and thus confirms the results for S_{ext} and V_{mic} deduced from N$_2$-gas sorption measurements (Section 5.1.4, Table 5.2). Therefore, in the following, the ASAXS results will be discussed focusing on the sample series CMn M and CMn L. The scattering curves of the sample series CMn S can be found in Appendix A.

The evaluation of the Mn scattering form factor $S_{\text{Mn}}(q)$ from ASAXS measurements is exemplarily shown for sample CMn L 48. Figure 5.15 shows the total (SAXS) cross section of the hybrid sample. Compared to the respective carbon scaffold (see Figure 5.14), oscillations appear in the Porod-region around $q_0 = 0.25$ nm^{-1}, hinting at an additional structure with a size of about $2/q_0 = 8$ nm [93]. In addition, the separated intensity $\Delta I(q, E_1, E_2)$ (see Section 3.2.4) is shown.

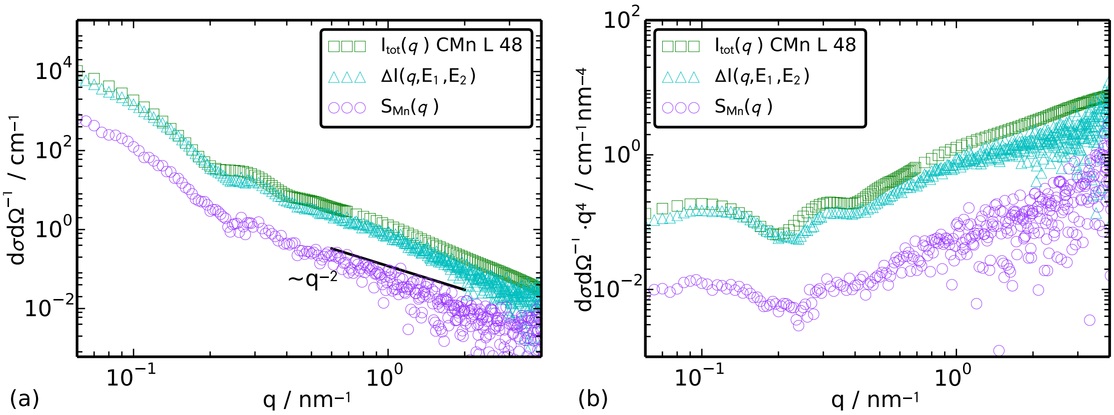

Figure 5.15: (a) Total scattering cross section $I_{\text{tot}}(q)$ for hybrid sample CMn L 48, its respective separated intensity $\Delta I(q, E_1, E_2)$ and scattering form factor of Mn $S_{\text{Mn}}(q)$, according to Equation 3.32. The black line indicates a q^{-2} behavior.
(b) Same curves, however multiplied by q^4.

The oscillations already present in the total scattering curve of the hybrid material remain, however an influence of the carbon scaffold is still inherent in the separated intensity. This is due to a cross term that does not vanish in the separated intensity [124], an effect that shows whenever the phases present in the system are not completely separated but rather share common interfaces (here: MnO_2 on the carbon scaffold). To overcome this problem, the separated intensity has to be calculated for a third energy, then the form factor $S_{\text{Mn}}(q)$ of the Mn contribution can be calculated (Section 3.2.4, Equation 3.32). The result of this procedure is also plotted in Figure 5.15. For high q-values, the envelope of the data follows a power law with a q exponent close to -2 (see Figure 5.15 (a)).

The Mn structure factor $S_{\text{Mn}}(q)$ of the hybrid samples CMn M is shown in Figure 5.16, with respective relative MnO_2 mass uptakes ranging from 48 to 130 wt.% (compare Section 5.2.1). The graph reveals the evolution of oscillations in the region from 0.2 to 0.5 nm^{-1}, shifting to lower q with increasing relative MnO_2 mass uptake. Obviously, the deposition mainly affects a region in q below 0.5 nm^{-1}, while in the region $q > 0.5$ nm^{-1}, the curves are identical within the range of experimental error. This again hints towards a manganese deposition mainly on S_{ext}, since no change in the scattering curve in the q-range > 1 nm^{-1} that is generally attributed to micropores is observed (compare Figure 5.14).

In the following, the shift in the oscillations will be compared to a core-shell model, corresponding to a MnO_2 layer around the carbon particles. For the structure factor $S_{\text{Mn}}(q)$ however, the core-shell model translates into a hollow-sphere model, since only contributions of the scattering originating from Mn survive (see Section 3.2.4 and the exemplarily evaluation of the structure factor for sample CMn L 48 above).

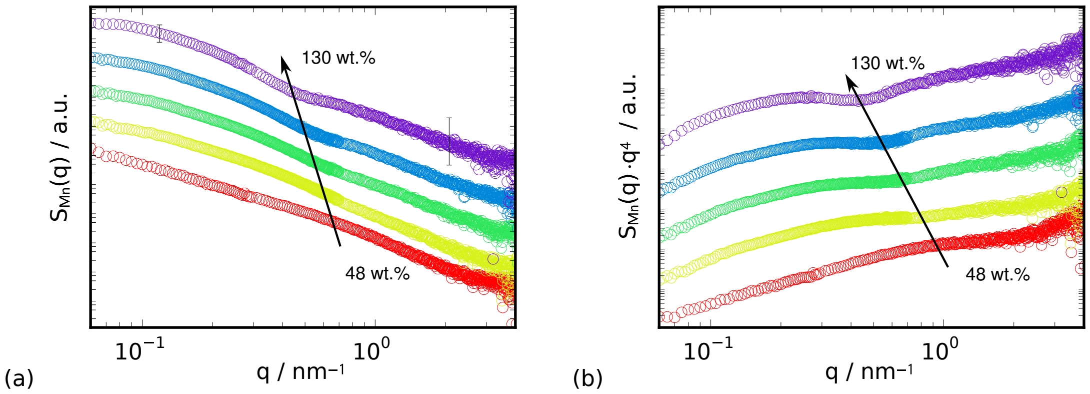

Figure 5.16: Structure factor $S_{\mathrm{Mn}}(q)$ (a) and $S_{\mathrm{Mn}}(q) \cdot q^4$ (b) for hybrid samples CMn M, loaded with different weight % of Mn. The data are shifted vertically for clarity. The error bars are plotted exemplarily and are evaluated using error propagation.

Figure 5.17 shows the theoretical scattering intensities of a sphere with a radius of 27 nm and hollow spheres, calculated from Equations 3.34 and 3.33, respectively. The oscillations for the sphere decay according to a q^{-4} power law. By adding a shell to the particle, additional oscillations in the envelope of the curve appear. Nevertheless, at large q-values, the envelope still exhibits a q^{-4} decay, indicating a smooth surface of the shell. Increasing the layer thickness from 3 to 9 nm at a constant inner radius R_{i} causes a shift of the modulation to smaller q-values. The same trend is observed in the experimental data presented in Figure 5.16.

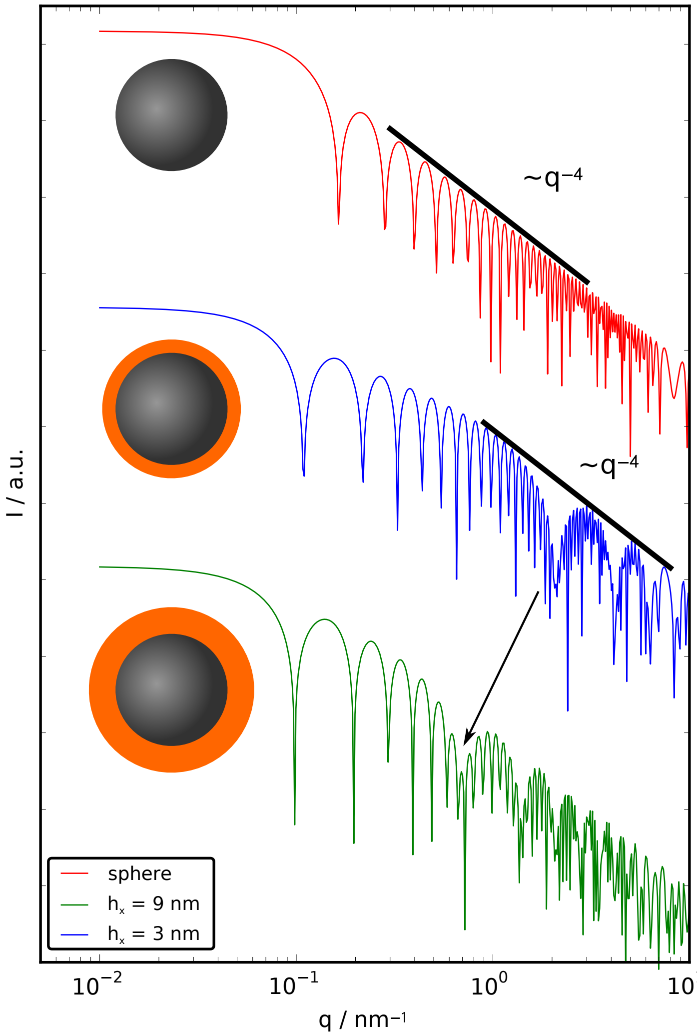

Figure 5.17: Scattering intensity calculated for a sphere of radius 27 nm (top) and from hollow sphere model, Equation 3.33, for the same core radius and a shell thickness h_x of 3 nm (middle) and 9 nm (bottom). The curves are shifted vertically for clarity.

In order to determine the layer thickness of MnO_2 enclosing the carbon particles in the hybrid samples prepared, the first minimum in the form factor of a hollow sphere (HS) is fitted to the experimentally derived form factor $S_{\mathrm{Mn}}(q)$, calculated according to Equation 3.32. For the model function, the inner radius R_i and the scattering contrast were kept constant and only $R_\mathrm{a} = R_\mathrm{i} + h_\mathrm{x}$ was varied. This variation is shown exemplarily in Figure 5.18, where the experimental form factor (purple circles), also multiplied by q^4 for better resolution of the minimum, is plotted vs. the scattering vector q. The first minimum in the modulation of the model function (Equation 3.33) fits well to the data for a fixed inner radius of 130 nm and an outer radius of 158 nm, leading to a MnO_2 layer thickness h_x of (28±2) nm.

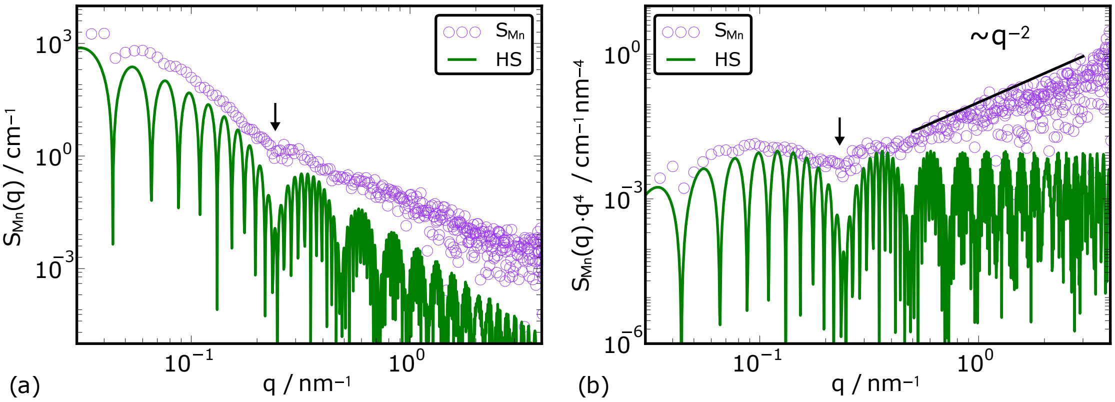

Figure 5.18: (a) $S_{\mathrm{Mn}}(q)$ of sample CMn L 48 (open circles) and hollow sphere model (line, Equation 3.33) with R_i = 130 nm and a shell thickness of h_x = 28 nm.
(b) Respective intensities multiplied by q^4, with a black line showing a q^{-2} behavior for the envelope.
In both figures, the black arrow marks the location of the minimum in the measured data.1

For larger q-values, the experimental data differ from the model function (see Figure 5.18), exhibiting a q^{-2} behavior, indicating a rough (fractal) surface structure [115]. This effect can be attributed to typical MnO_2 morphologies like flakes and needles on the layer surface, as they are visible in the SEM images in Figure 5.2 [74, 142]. As a consequence, the density of the MnO_2 shell is expected to be lower than the bulk value of 3.0 gcm^{-3} [141, 151].

The fit of the hollow sphere model to the experimental form factor $S_{\mathrm{Mn}}(q)$ was performed for all samples of the series CMn S,M,L. For the series CMn M and CMn L, Figure 5.19 (a) shows the MnO_2 layer thickness h_x vs. the relative MnO_2 mass uptake.

The series CMn M and CMn L both reveal a linear increase of h_x with increasing mass uptake. The series with the larger particles shows a steeper increase, which can be explained by the smaller external surface area on which the MnO_2 is deposited, thus resulting in a thicker MnO_2 layer at a

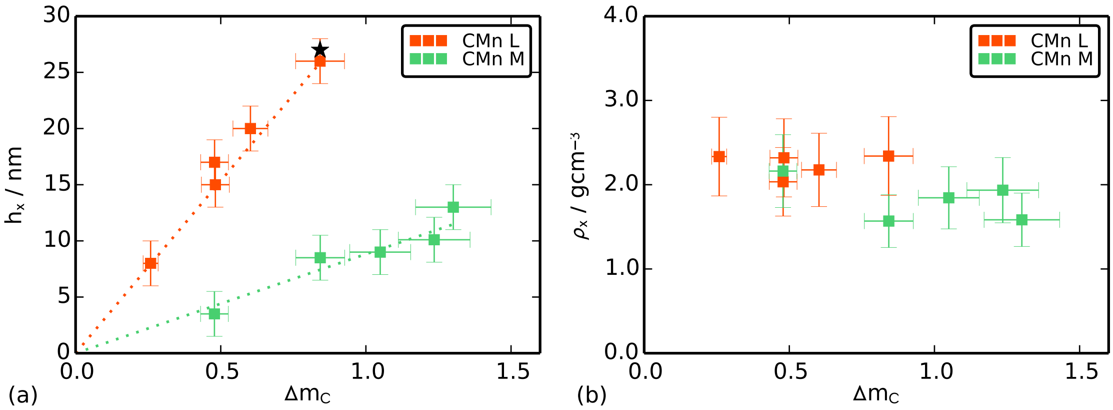

Figure 5.19: (a) Layer thickness h_x determined from hollow sphere model (square-marker) vs. the relative MnO_2 mass uptake. The dotted lines represent a linear fit of the data and extrapolation to the origin. The MnO_2 layer thickness found in the SEM observation (Figure 5.2) is represented as a black star-marker. (b) Effective shell density ρ_x vs. the relative mass uptake Δm_C. Error bars are calculated via error propagation. This data are presented in [141].

given relative mass uptake. For example, at a MnO_2 mass uptake of about 0.8, the layer thickness is about three times higher for CMn L than for CMn S. Comparing the value of h_x for sample CMn L 48 to the value found in the SEM observation in Figure 5.2, a very good agreement is obvious [141].

Assuming all MnO_2 mass being deposited on the external surface area S_{ext} of the monolithic carbon xerogel and forming a shell coating the carbon particle, an effective shell density ρ_x can be calculated from the layer thickness h_x by solving Equation 5.1 for the density ρ_{MnO_2}:

$$\rho_x = \frac{m_{Mn}}{S_{ext} \cdot m_C \cdot h_x} = \frac{\Delta m_C}{S_{ext} \cdot h_x}. \tag{5.2}$$

The resulting effective densities ρ_x are lower than the MnO_2 bulk density of 3.0 g/cm^3 [151]. Within sample series CMn L, the density is nearly constant around a value of 2.2±0.4 g/cm^3, whereas for series CMn S a mean value of 1.8±0.4 g/cm^3 is found. A general trend of a reduction in density with increasing mass uptake can be observed [141].

As already noted in Section 5.2.1, due to the high relative mass uptake in the process, the precursor solution becomes highly diluted (see also Figure 5.9). More than 50 % of $NaMnO_4$ are consumed at a relative mass uptake of 0.6 to 0.9, depending on whether a full conversion of $NaMnO_4$ to MnO_2 or a composition of MnO_2, Mn_2O_3, $NaMnO_4$ and Na_2MnO_4 is taken into account. The respective contributions to the composition were identified in the XPS-study presented in Section 5.2.2. The slight decline in the effective density ρ_x is therefore likely to be caused by dilution of the precursor solution.

The effective density ρ_x represents an average value of the density of the shell. Therefore, for thicker layers, a gradient in the shell structure can not be excluded. Furthermore, the q^{-2}-dependence in Figure 5.15 confirms that hypothesis, as it hints for a rough structure of the deposited MnO_2 layer and therefore a less dense structure of the manganese oxide layer.

The strong correlation of the deposition process with the specific external surface area S_{ext} of the carbon scaffold is supported further when examining the shell densities at a relative MnO_2 mass uptake of 0.46 (see Figure 5.19): Although the underlying three samples exhibit about the same shell density ρ_x, their shell thickness differs by a factor of about 4, which in turn corresponds about to the ratio of the external surface area between sample series CMn S and CMn L (Section 5.1.4).

5.4 Electrochemical Performance

5.4.1 Capacitance

The gravimetric capacitance at a potential scan rate of 2 mVs^{-1} for the bare carbon xerogel and hybrid electrodes of sample series CMnEC, respectively are shown in Figure 5.20. The sample CEC S exhibits a butterfly-shaped CV curve with a pronounced minimum at 0.02 V vs. Ag/AgCl. This characteristic shape is well known for microporous carbons [33, 160]. The minimum is referred to as the potential of zero charge (PZC), which in neutral electrolyte solutions equals the immersion potential of the electrode [160]. At potentials lower than the PZC, mainly Na^+ ions are adsorbed in the electrochemical double layer, whereas at potentials higher than the PZC mainly SO_4^{2-} ions contribute to the current.

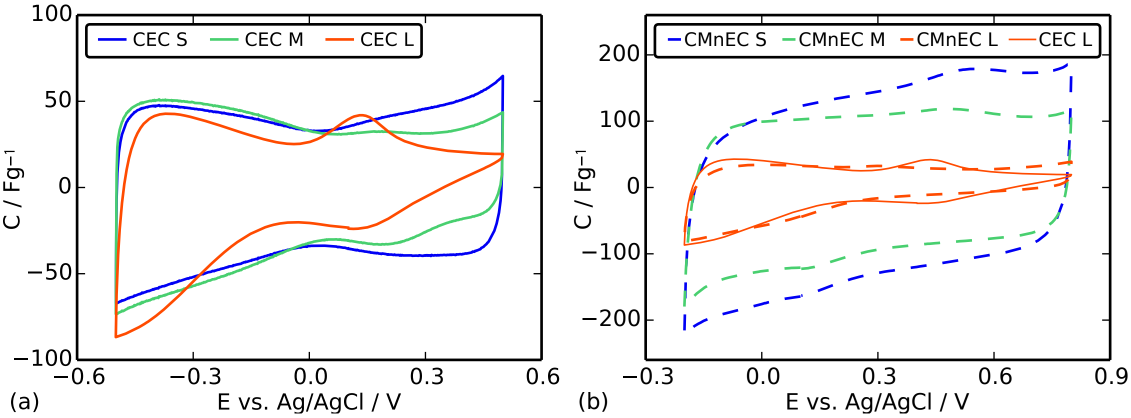

Figure 5.20: Cyclic voltammogram at 2 mVs^{-1} for the samples of series CMn EC in 1 M Na_2SO_4 electrolyte solution. The full lines represent the CV curves of the bare carbon xerogel (a), the dashed lines the corresponding curves for the hybrid electrodes (b). The capacitance values are normalized to the electrode mass. In Figure 5.20 (b), the CV of C L is shifted along the x-axis by +0.3 V for better comparison.

With increasing particle size (C S to C L), the current (and thus C) at the positive vertex potential (i.e. 0.5 V vs. Ag/AgCl) ceases and a bump arises around 0.15 V vs. Ag/AgCl. It was shown by Lorrmann *et al.*, that the decrease in the anodic current is caused by a sieving effect, since at given scan rate the fraction of micropores accessible (i.e. micropores close to the particle surface) to the SO_4^{2-} ions is strongly decreasing with increasing particle size [34].

The bump is generally attributed to redox reactions of quinone/hydroquinone groups on the carbon surface [40]. However, the carbon xerogels of this series were prepared under identical chemical conditions and subjected to the same pyrolysis step (see Section 3.1.1), therefore identical surface groups are expected in all samples. Furthermore, XPS studies evaluated for the PhD thesis of Volker Lorrmann showed identical surface groups with respect to their valency for all carbon xerogels investigated, regardless of particle size [161].

A different mechanism is therefore suggested for the rise of this bump with increasing particle size: at voltages higher than the PZC, SO_4^{2-} ions are forced into the micropores of the carbon xerogel, until all accessible storage sites (close to the particle surface) are occupied. At even higher voltages, no more ions can be stored and therefore the current ceases, resulting in the broad peak around 0.15 V vs. Ag/AgCl. Figure A.3 in Appendix A shows the CV of sample CEC L for different potential scan rates. For higher scan rates such as 50 $\mathrm{mVs^{-1}}$, the release-bump in the discharge branch disappears. This behavior is in contrast to the characteristics found for redox-peaks, for which the potential distance of the red- and ox-peak increases with increasing potential scan rate, while both peaks still remain visible in the CV-plot [19]. Thus, the scan rate dependence of the bump rather confirms the accessibility scenario.

Figure 5.20 (b) shows the CV for the hybrid electrodes of the series CMnEC, the respective integrated capacitance values are compiled in Table 5.4. The samples CMnEC S and CMnEC M show a strong increase in capacitance whilst maintaining an almost rectangular shape. For sample CMnEC S the rectangle is clearly tilted, originating from an increased contact resistance of the electrode. This behavior will be discussed in detail in Section 5.4.2. The slope of the curve at the vertex potentials is very steep, hinting for little influence of the low intrinsic electrical conductivity of the MnO_2 layer covering the carbon scaffold. Around 0.1 and 0.5 V vs. Ag/AgCl weak bumps appear, that already have been identified to originate from proton- or ion intercalation into the manganese oxide layer (see Section 4.2.1).

For sample CMnEC L with a relative MnO_2 mass uptake of only 2 wt.%, the infiltration with MnO_2 did not lead to an enhancement of the capacitance, however interesting conclusions can be drawn from the behavior of this electrode (see also the zoom into the curves in Figure A.4 (a) and A.4 (b) in Appendix A). Clearly, the bump in the CV of C L vanishes with the MnO_2 deposition. Trapping of SO_4^{2-} ions is therefore no longer a dominating effect, presumably because the micropore access for large SO_4^{2-} ions is blocked by the MnO_2 layer. Around the positive vertex potential, an increase in the differential capacitance due to pseudocapacitive storage, compared to the pure

Table 5.4: Capacitance values for the sample series CMnEC, evaluated from the charging half-cycle CV measurements at 2 $\mathrm{mVs^{-1}}$, normalized to total electrode mass (C_{grav}) and volume (C_{vol}), respectively.

	C S	C M	C L	CMnEC S	CMnEC M	CMnEC L
C_{grav} $[\mathrm{Fg^{-1}}]$	43±4	39±4	32±3	141±10	104±10	31±3
C_{vol} $[\mathrm{gcm^{-3}}]$	16±1	11±1	7±1	92±1	46±1	7±1

double layer capacitance, becomes evident. At the negative vertex potential, the sieving effect is still visible, indicating that small Na^+ ions may pass through the MnO_2 layer. The contribution of Na^+ double layer storage is slightly lower than in the carbon electrode, the reason is likely to be found in hindered diffusion of the ions due to the manganese layer, an effect that is not fully compensated by the additional pseudocapacitance.

The integrated capacitance is plotted vs. the MnO_2 mass uptake in Figure 5.21. Obviously, the sample CMn S with the largest external surface area and therefore highest MnO_2 mass uptake shows the highest specific capacitance. The gravimetric capacitance shows a linear dependence on the MnO_2 mass uptake, therefore a very efficient use of the MnO_2 in charge storage was accomplished (compare Section 4.2.1). Compared to the respective capacitance of the bare carbon xerogel electrode, the gravimetric capacitance of sample CMn S increased by a factor 3, the volumetric capacitance even by a factor 6 (see Table 5.4).

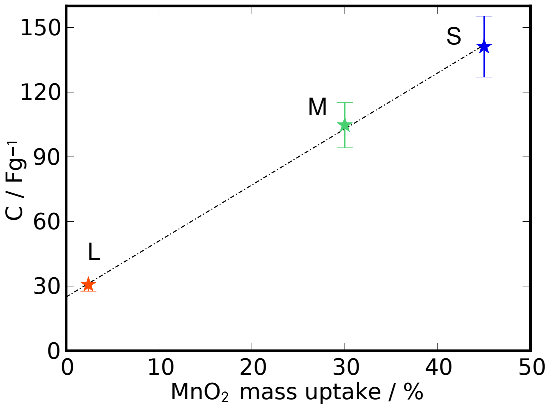

Figure 5.21: Gravimetric capacitance (per total mass of electrode) for series CMnEC vs. the MnO_2 mass uptake, derived from the CV curves at 2 mVs^{-1}, normalized to total electrode mass. The error bars mainly origin from the error in the determination of the electrode mass. The dashed line represents a linear fit of the data.

5.4.2 Dynamic Behavior

The dynamic behavior of the electrodes of the series CMnEC was investigated analyzing composite fiber electrodes in a sandwich cell and powder material in cavity micro electrode-measurements (CME). At first, the behavior of the fiber reinforced electrode will be discussed.

Figure 5.22 (a) shows the integrated gravimetric capacitance, C_{grav}, as a function of the potential scan rate $\mathrm{d}E/\mathrm{d}t$. The graph clearly reveals that the dependence of the capacitance on the scan rate is less pronounced for the bare carbon xerogel electrodes than for the hybrid samples. At a scan rate of 100 mVs^{-1}, the capacitance of the carbon electrode C S drops to about 70 % of its initial value, whereas the corresponding hybrid electrode CMnEC S only retains 42 % at the same conditions. However, with a factor of 2, the absolute value of the capacitance even at 200 mVs^{-1} is still significantly improved compared to the bare carbon xerogel.

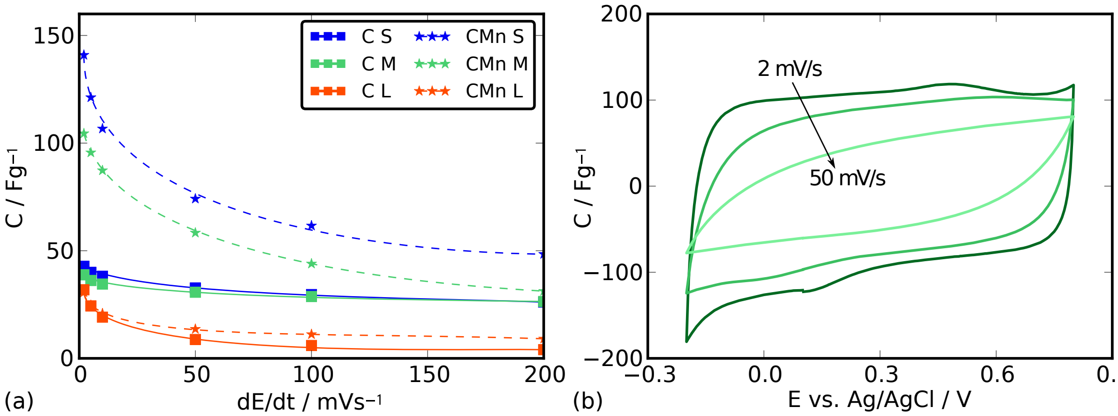

Figure 5.22: (a) Gravimetric capacitance vs. applied scan rate. The lines are drawn as a guide to the eye. Solid lines: bare carbon electrodes, dashed lines: hybrid electrodes.
(b) Cyclic voltammogram for the sample CMnEC M with varying scan rate.

The reason for the decreasing performance of the hybrid electrodes at high scan rates can be enlightened by analyzing the CV at various scan rates, as shown in Figure 5.22 (b). The rectangular shape of the curve at 2 mVs^{-1} gets more and more disturbed with increasing scan rate. As already mentioned in Section 4.2.2, the increased ESR of the electrode due to the MnO_2 deposition is responsible for this behavior.

Further insight into the dynamic behavior can be derived from CME measurements, exemplarily shown in Figure 5.23 for the samples C S and CMnEC S. For the bare carbon electrode (Figure 5.23 (a)), the typical butterfly shape persists at all scan rates applied. Solely at the positive vertex potential, the capacitance strongly decreases with increasing scan rate. This effect is due to the size of the SO_4^{2-} ions, which for high scan rates are moving too slowly into the carbon particle (see also

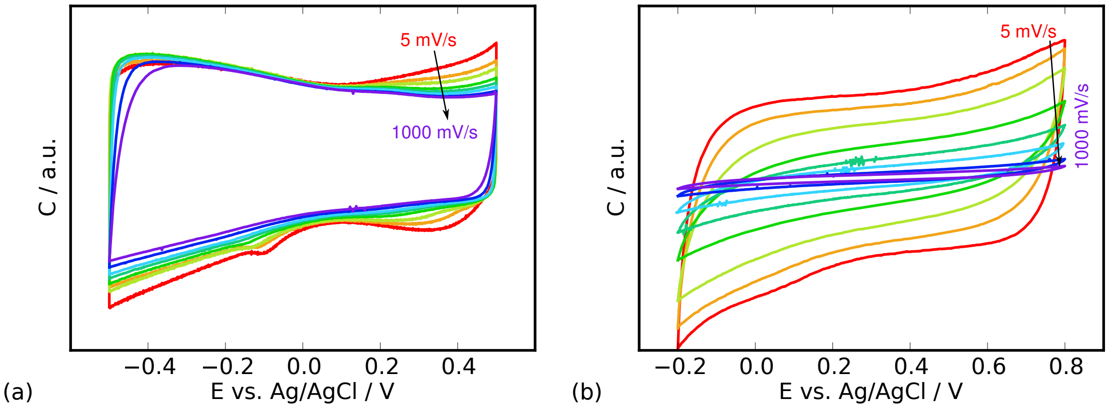

Figure 5.23: Cyclic voltammogram (CV) for sample C S (a) and CMnEC S (b), measured with a cavity micro electrode (CME). The potential scan rate ranges from 5 to 1000 mVs^{-1}. Since only the shape of the CV curve is discussed, the unit of the capacitance is arbitrary.

Lorrmann *et al.*, [34]).

An utterly different behavior is observed in the CV of the CMnEC S powder shown in Figure 5.23 (b). The shape of the curve strongly depends on the applied scan rate and for a scan rate of 1000 mVs^{-1}, the capacitance has faded nearly completely. At this point, only the double layer capacitance of the external surface area of the electrode is contributing to the capacitance.

The red curve in Figure 5.23 (b) shows the capacitance at a scan rate of 5 mVs^{-1}. Whilst still rectangular, the rectangle is tilted, as already mentioned earlier in this chapter for the fiber electrode. This behavior origins from the contact resistance of the electrode. Figure 5.24 compares the capacitance retention of the fiber electrodes with the one of the respective hybrid powder measured with the CME. The plot reveals that the capacitance always drops faster in the CME measurement. The reason for this behavior is best explained with the cartoon in Figure 5.25: The powder measured in the CME exhibits many contact points between the individual particles, increasing the contact resistance over the MnO_2 layer between the particles. In contrast, in the fiber electrode, the carbon scaffold is well interconnected, once directly through the growth of the xerogel, additionally through the carbon fibers contributing to the transversal conductivity. The tilt of the CV-curve results from the increased contact resistance of the electrode with the current collector, due to the homogeneous coating of the carbon particles. For electrode CMnEC S there are more contact points (covered with MnO_2) than for the electrode CMnEC M and CMnEC L, therefore the behavior is more pronounced for that electrode. Here also lies one of the major possibilities to improve the hybrid electrodes: For optimal performance, interparticular contact resistance as well as the contact resistance between current collector and hybrid electrode has to be minimized, in order to access the storage capacity even at high scan rates.

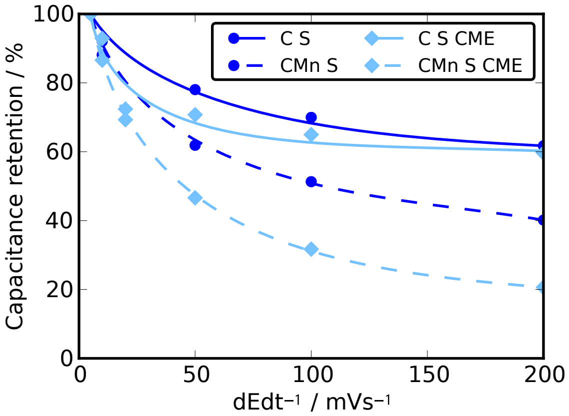

Figure 5.24: Capacitance vs. applied potential scan rate for sample CMnEC S. The circular markers represent measurements in the sandwich cell, the diamond markers show CME measurements. For each set, full lines represent the bare carbon xerogel C S, whereas dashed lines represent the hybrid sample CMnEC S. The lines are drawn as guides to the eye.

The use of fiber reinforced monolithic carbons as a scaffold is a first step in that direction, since the transversal electrical conductivity is improved, both, through the interconnected particles and the carbon fibers. As already mentioned, this is the reason for the superior performance of the fiber electrodes compared to the powder (see Figure 5.24). An additional benefit would be to avoid the MnO_2 phase at the current collector-electrode interface, as shown in Figure 5.25c). The direct contact of the carbon scaffold with the current collector will reduce the contact resistance and therefore significantly improve the dynamic behavior of the hybrid electrode. The MnO_2 at the interface could either be removed after deposition, e.g. via etching with HCl. A more practical way, however, is to avoid deposition at the backside of the electrode. This can be realized by applying electrodeposition approaches, as described by Donne *et al.* [162].

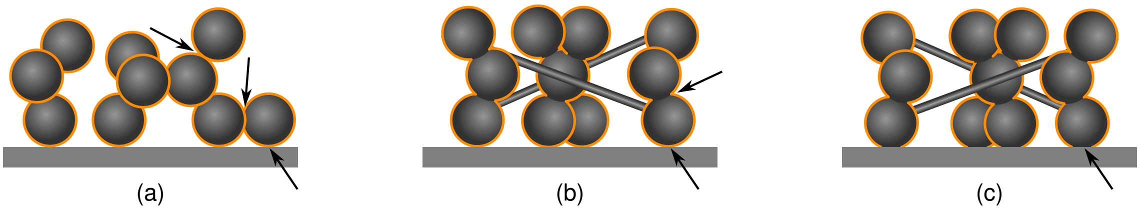

Figure 5.25: Cartoon of MnO_2 coated carbon particles (a) as measured in the CME and a coated, carbon fiber reinforced xerogel (b) as measured in the sandwich cell. Sketch (c) shows an improved electrode with the carbon in direct contact with the current collector. The arrows mark points of interest mentioned in the text. Note that the sketch is not true to scale.

5.5 Conclusion

The carbon xerogels prepared for the series CMnEC S,M,L showed a successful variation of the particle size and therefore the specific external surface area S_{ext}. From samples C S to C L, the external surface area was varied by a factor 4. The SEM investigation showed a homogeneous coating of the carbon scaffold, with a thickness of up to 27 nm. Whilst no separated domains of isolated MnO_2 clusters were found in the majority of the samples, thicker layers exhibit a flake- or petal-like structure, that is decreasing the density of the MnO_2 layer, when compared to the bulk value.

The macroscopic distribution of MnO_2 throughout the electrode showed no gradient for samples thinner than 1 mm. Gas sorption measurements revealed that no substantial amount of micropores was filled or secluded due to the deposition process. A strong correlation of the relative MnO_2 mass uptake with the specific external surface area was shown. Using ASAXS measurements in combination with a core-shell-model, the MnO_2 layer thickness was found to range between 3 and 26 nm. ASAXS proved to be a powerful tool to investigate the structure of the hybrid material and the model can be transferred to similar material systems.

The electrochemical characterization showed a strong correlation of the capacitance with the MnO_2 mass uptake, and therefore once again with the S_{ext}. CME measurements proved the approach of coating a carbon scaffold superior to the powder approach, where inter-particular connections increase the internal resistance of the electrode.

Chapter 6

Summary and Outlook

In this thesis, an electroless deposition approach of manganese oxide on a micro- and mesoporous carbon scaffold was investigated intensively, with special focus on the location of the active material in the hybrid electrode. To reach this goal, a variation of the carbon backbone structure was performed and an ASAXS model was developed.

In the first part of the thesis, hybrid electrodes prepared via a systematic variation of manganese oxide deposition time with a Na_2SO_4 precursor concentration of 0.05 M were analyzed (Chapter 4). MnO_2 mass uptakes reached up to 58 wt.%, leading to an increase of volumetric capacitance by a factor 5. However, this increased occurred on the cost of increasing the time constant for charging the electrode by a factor 4, when compared to the bare carbon xerogel electrode. The structural characterization gave hints for a deposition of the MnO_2 either in the micropores of the carbon particles, or on their external surface area.

In order to comprehensively investigate the location of the active material within the carbon scaffold, the carbon particle size and thereby the external surface area was varied systematically, while keeping the micropore volume of the xerogel constant (Chapter 5).

Monitoring the MnO_2 mass uptake upon deposition, it was shown that the sample with small carbon particles take up the highest amount of MnO_2. SEM images show a layer of MnO_2 around the carbon particles, reaching thicknesses up to 27 nm for samples with very high MnO_2 mass uptakes of up to 130 %. Thick layers also exhibited a flake- and petal-like sub-structure, that is often found for manganese oxides. The crystalline state of the deposit was determined to resemble birnessite structures. The chemical state of the manganese oxide was probed applying XPS measurements, showing similar chemical composition throughout all samples investigated. The main active species of Mn was found to be MnO_2, however large amounts of precursor residues were found.

ASAXS was applied for the first time on porous composite electrodes consisting of MnO_2-

carbon xerogel. The ASAXS model developed proved to be a powerful method for the analysis of the structural features of these hybrid electrodes, allowing integral and quantitative structural characterization of the sample on the microscopic scale. MnO_2 layer thicknesses ranging from 3 to 26 nm were found, with a very narrow distribution within the sample. The results obtained with the hollow sphere model are in good agreement with indications from other methods, such as the direct local evidence from SEM imaging.

The electrochemical characterization of the hybrid electrodes with different carbon particle sizes confirmed a correlation of capacitance with amount of manganese oxide in the electrode: The samples with small particles, taking up the highest amount of active material, also showed the highest capacitance.

From the findings, the different scenarios that were presented in the introduction (see Chapter 1, Figure 1.2) were eliminated, leaving scenario 2, a homogeneous coating of the external surface area of the carbon scaffold as the dominating process.

It was shown that coating a carbon scaffold with the active material leads to superior charging behavior, compared to powder approaches, since the number of contact sites and therefore the internal resistance of the electrode is reduced (Chapter 5.4.2). Therefore, the coating approach should be further investigated. Monitoring the precursor pH concentration during deposition will allow a more accurate determination of the deposition stage, and ultimately reduce the amount of MnO_2 that introduced as “dead mass”, not contributing to charge storage. Furthermore, alternative deposition methods such as electrochemical deposition should be further investigated. Approaches presented e.g. by Pang *et al.* point the way, and varying the carbon scaffold will help to control the deposition even further [58].

Long-term measurements will give insight in the stability of the coatings, however first the cell design has to be optimized, carefully balancing the two electrodes in the supercapacitor in terms of capacitance. In this scope, asymmetric devices of one electrode containing an active material, while the other electrode consists of carbon, should also be investigated, since they will allow higher cell voltages and therefore higher specific energies [62, 64].

The ASAXS method developed in the scope of this thesis should be further promoted and applied on other material systems, since this technique allows to draw important conclusions and allows to deduce integral and quantitative information towards a rational design of high performance electrodes.

Appendix A

Additional Graphs

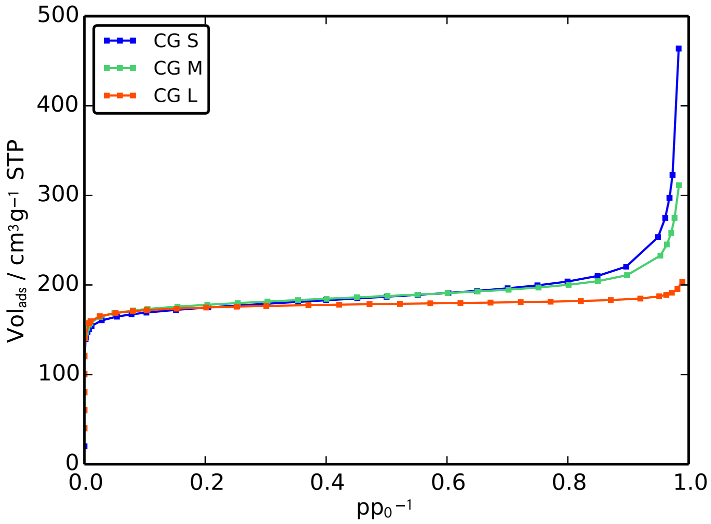

Figure A.1: N_2 gas sorption isotherms of the carbon backbone for the three different particle sizes small (S), medium (M) and large (L) used for the ASAXS measurements. Only the adsorption branch of the isotherm was measured. The data are normalized to the carbon xerogel mass.

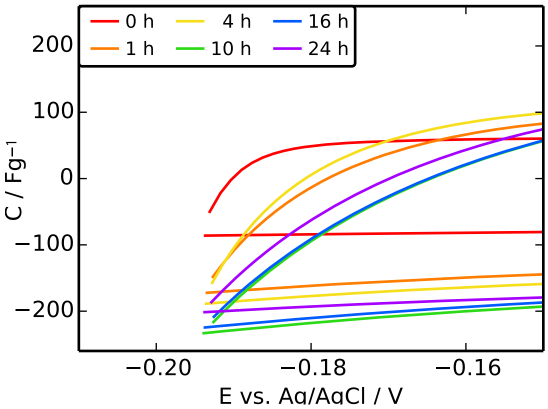

Figure A.2: Detail of Figure 4.5, a cyclic voltammogram at 1 mV/s of the sample series CMnT, with capacitance values normalized to electrode mass.

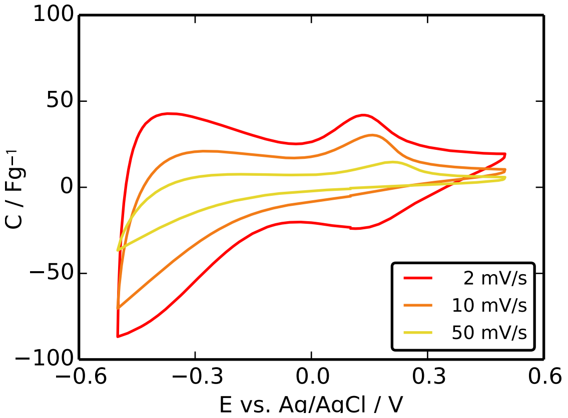

Figure A.3: Additional graph to Figure 5.20: CV of sample C L at various potential scan rates.

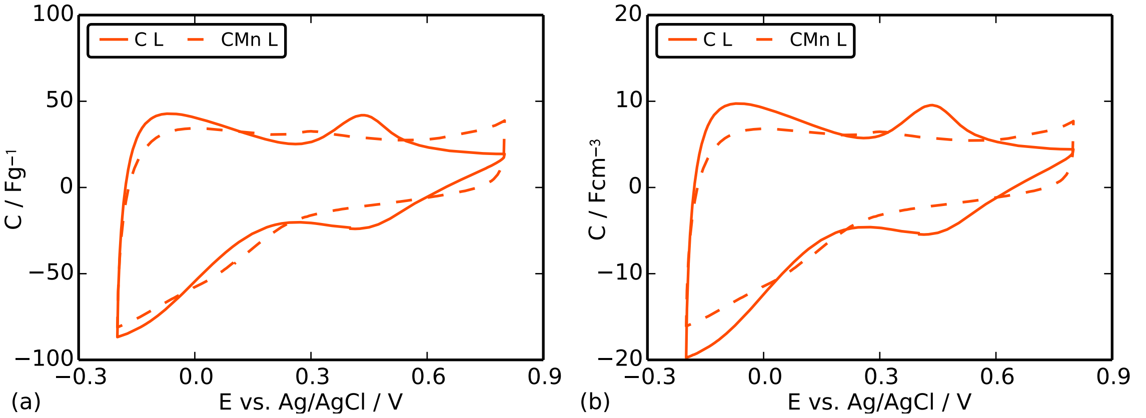

Figure A.4: Cyclic voltammogram at 2 mVs^{-1} of the electrodes C L and CMn L, normalized to electrode mass (a) and electrode volume (b). The CV for C L is shifted by +0.3 V for comparison.

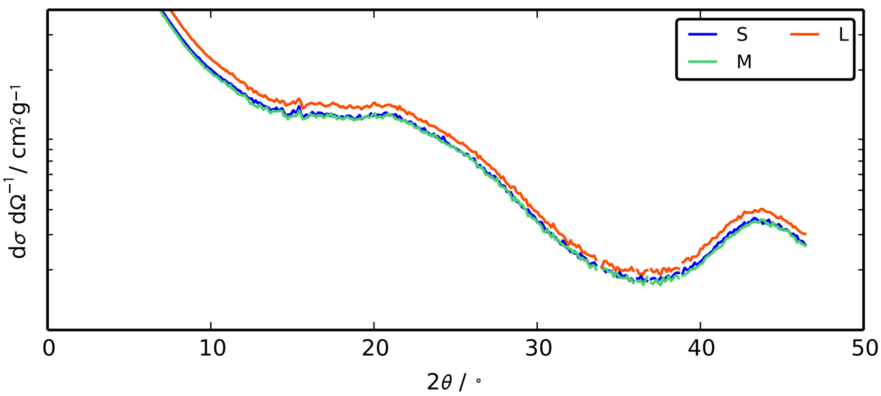

Figure A.5: Semilogarithmic plot of the WAXS cross section of the carbon xerogels for the series CMn. Data discussed in Section 5.1.3.

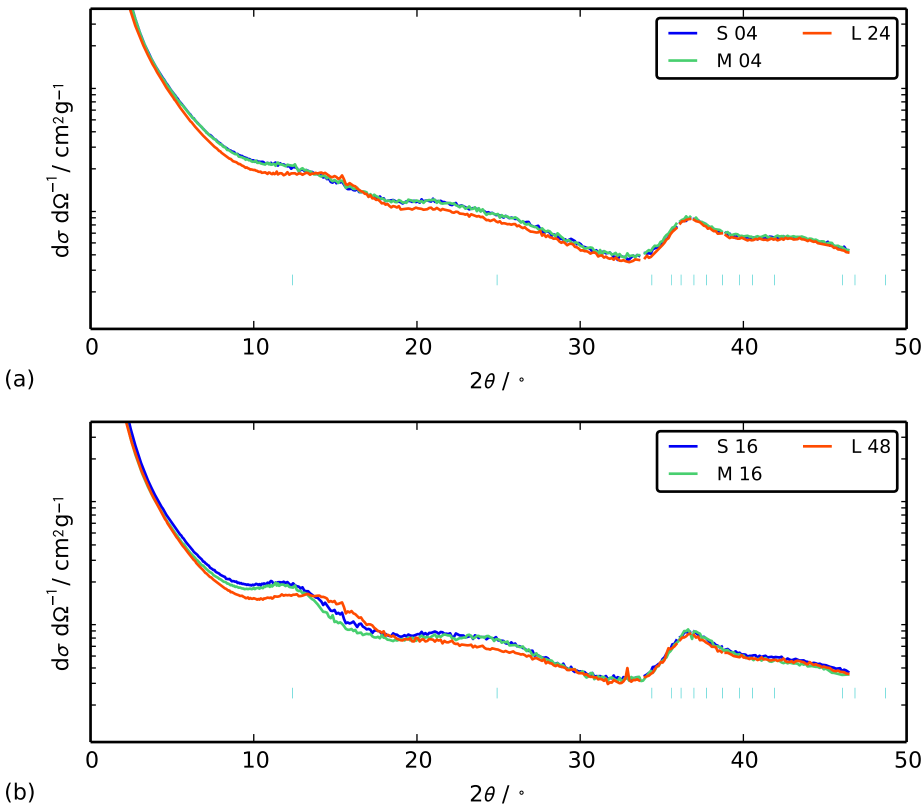

Figure A.6: Semilogarithmic plot of the WAXS cross section of the carbon xerogels for samples containing 32 wt.% and 46 wt.% in Figures (a) and (b), respectively. Data discussed in Section 5.1.3.

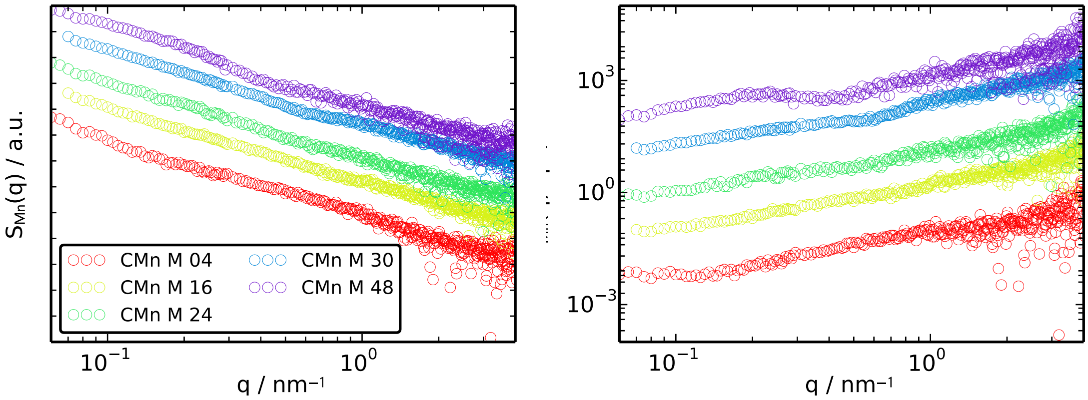

Figure A.7: Structure factor $S_{\mathrm{Mn}}(q)$ and $S_{\mathrm{Mn}}(q) \cdot q^4$ for hybrid samples CMn S, loaded with different weight % of Mn. The data are shifted by vertically for clarity.

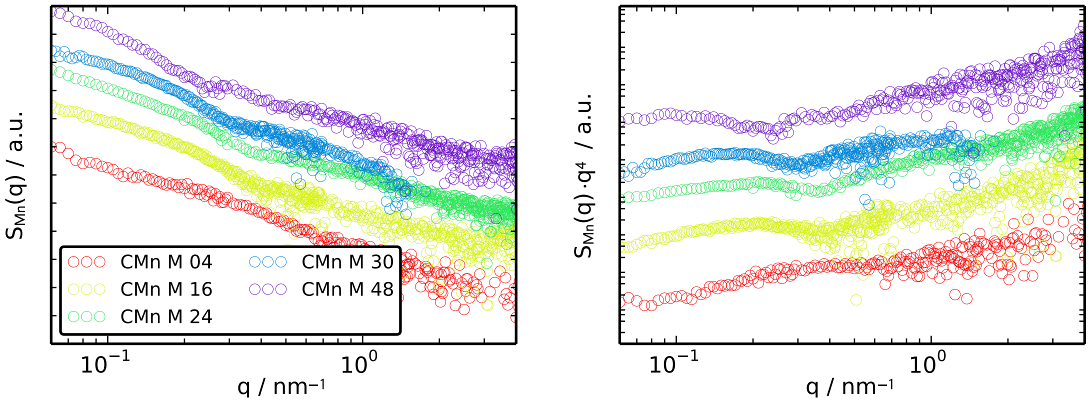

Figure A.8: Structure factor $S_{\mathrm{Mn}}(q)$ and $S_{\mathrm{Mn}}(q) \cdot q^4$ for hybrid samples CMn L, loaded with different weight % of Mn. The data are shifted by vertically for clarity.

Appendix B

Tabulated Data

B.1 Tabulated Data of Sample Series CMnT

B.2 Tabulated Data of Sample Series CMnEC and CMnG

B.3 Tabulated Data of Sample Series CMn S,M,L

Table B.1: Sample name, deposition time, t_{dep}, carbon mass, m_{C}, MnO_2 mass, m_{MnO_2}, relative mass uptake normalized to carbon mass, Δm_{C}, and normalized to total mass, Δm_1, for sample series CMnT used for electrochemical measurements (Section 4.2.1) and graphs for mass-uptake (Section 4.1.1).

sample	t_{dep} [h]	m_{C} [g]	m_{MnO_2} [g]	Δm_{C} [%]	Δm_1 [%]
ref3	0	0.022	0.0	0	0
31	1	0.0218	0.0082	38	27
32	4	0.0213	0.0147	69	41
33	10	0.0219	0.0221	101	50
34	16	0.0245	0.0275	112	53
35	24	0.0231	0.0319	138	58

Table B.2: Sample name, deposition time, t_{dep}, carbon mass, m_{C}, MnO_2 mass, m_{MnO_2}, relative mass uptake normalized to carbon mass, Δm_{C}, and normalized to total mass, Δm_1, for sample series CMnT used for gas sorption analysis (Section 4.1.3).

sample	t_{dep} [h]	m_{C} [g]	m_{MnO_2} [g]	Δm_{C} [%]	Δm_1 [%]
P30_0	0	0.1389	0.0	0	0
P30_4	4	0.1413	0.0893	63	39
P30_10	10	0.1343	0.1203	90	47
P30_16	16	0.138	0.163	118	54

Table B.3: MnO_2 mass uptake, sample density and structural data derived via N_2 sorption for series CMnT. All mass specific values (S_{BET}, S_{ext}, V_{mic}) are being presented normalized to the mass of the carbon xerogel. The density ρ includes fibers and structural inhomogeneities of the electrodes.

sample	MnO_2 [wt.%]	ρ [gcm^{-3}]	S_{BET} [m^{2}g^{-1}]	S_{ext} [m^{2}g^{-1}]	V_{mic} [cm^{3}g^{-1}]
P30_0	0	0.31±0.03	786±79	191±19	0.25±0.03
P30_4	39±4	0.51±0.05	595±60	195±20	0.18±0.02
P30_10	47±5	0.62±0.06	404±40	207±21	0.09±0.01
P30_16	54±5	0.73±0.07	357±36	190±20	0.08±0.01

Table B.4: Sample name, deposition time, t_{dep}, carbon mass, m_{C}, $\mathrm{MnO_2}$ mass, $m_{\mathrm{MnO_2}}$, relative mass uptake normalized to carbon mass, Δm_{C}, and normalized to total mass, Δm_{1}, for sample series CMnEC and CMnG.

sample	t_{dep} [h]	m_{C} [g]	$m_{\mathrm{MnO_2}}$ [g]	Δm_{C} [%]	Δm_{1} [%]
C S	0	0.2444	0.0	0	0
C M	0	0.1809	0.0	0	0
C L	0	0.1905	0.0	0	0
CMnEC S	4	0.149	0.121	81	45
CMnEC M	4	0.16	0.068	42	30
CMnEC L	4	0.1718	0.0032	2	2
CMnG S	4	0.0842	0.0788	94	48
CMnG M	4	0.0749	0.0305	41	28
CMnG L	4	0.0729	0.0019	3	3

Table B.5: Sample name, deposition time, t_{dep}, carbon mass, m_{C}, $\mathrm{MnO_2}$ mass, $m_{\mathrm{MnO_2}}$, relative mass uptake normalized to carbon mass, Δm_{C}, and normalized to total mass, Δm_1, for sample series CMn S,M,L.

sample	t_{dep} [h]	m_{C} [g]	$m_{\mathrm{MnO_2}}$ [g]	Δm_{C} [%]	Δm_1 [%]
C S	0	0.1048	0.0	0	0
CMn S 4	4	0.087	0.04	46	31
CMn S 16	17	0.088	0.076	86	46
CMn S 24	24	0.084	0.085	101	50
CMn S 30	30	0.083	0.099	119	54
CMn S 48	48	0.087	0.133	153	60
C M	0	0.1746	0.0	0	0
CMn M 4	4	0.092	0.044	48	32
CMn M 16	17	0.089	0.075	84	46
CMn M 24	24	0.081	0.085	105	51
CMn M 30	30	0.085	0.105	124	55
CMn M 48	49	0.093	0.121	130	56
C L	0	0.1601	0.0	0	0
CMn L 4	4	0.089	0.023	26	21
CMn L 16	17	0.081	0.039	48	32
CMn L 24	24	0.094	0.045	48	32
CMn L 30	30	0.088	0.053	60	38
CMn L 48	49	0.095	0.08	84	46

Appendix C

Thermodynamical Treatment of Pseudocapacitance

The following section is a summary of the theoretical treatment of pseudocapacitance, as published by Eucken and Weblus [37] and of Gileadi and Conway [38], following the derivation in [21].

At potentials E still far from H_2-gas evolution, the underpotential deposition of H on a metal electrode surface M takes place when a metal electrode is placed in aqueous acid solutions:

$$\mathrm{H_3O^+} + \mathrm{M} + e \leftrightharpoons \mathrm{MH_{ads}} + \mathrm{H_2O} \tag{C.1}$$

The fractional coverage θ of the electrode surface with H atoms rises monotoneously, and each H adsorbed requires one electron to pass over the interface. This can be expressed by a Langmuir-type isotherm of electrosorption

$$\frac{\theta}{1-\theta} = Kc_{H^+}\exp(EF/RT), \tag{C.2}$$

Which can also be written as

$$\theta = \frac{Kc_{H^+}\exp(EF/RT)}{1+Kc_{H^+}\exp(EF/RT)}. \tag{C.3}$$

Herein, θ is the fractional surface coverage and 1-θ is the fraction of unoccupied surface sites, K is a constant, c_{H^+} the concentration of H^+, F the Faraday constant, R the gas constant and T the temperature.
Adsorption will happen, if the Gibbs energy of M-H is lower than of the H-H bonding:

$$G_{\mathrm{MH_{ads}}} < G_{\frac{1}{2}\mathrm{H_2}} \tag{C.4}$$

or, in case of solvated Na ions in the Helmholtz double layer:

$$G_{\mathrm{MNa_{ads}}} < G_{\mathrm{Na_{solv}}} < G_{\frac{1}{x}\mathrm{Na}_x} \tag{C.5}$$

Therefore, it must be energetically more favorable for the ion to adsorb on the metal surface than to form H_2. In such systems, pseudocapacitance can occur and C_Φ can be derived from Equation C.3

as

$$\begin{aligned} C_\Phi &= q_1(\mathrm{d}\theta/\mathrm{d}E) && \text{(C.6)} \\ &= \frac{q_1 F}{RT}\frac{Kc_{H^+}\exp(EF/RT)}{[1+Kc_{H^+}\exp(EF/RT)]^2} && \text{(C.7)} \\ &= \frac{q_1 F}{RT}\,\theta(1-\theta) && \text{(C.8)} \end{aligned}$$

where the charge for formation of a monolayer of H on M is q_1.
The term "*pseudo*"-capacitance was chosen, since C.7 is of the form of Equation 1.1, the definition of the capacitance. However, due to the Faradaic charge transfer involved, it emanates from a completely different mechanism than the electrostatical double layer capacitance [21].

It can easily be seen that Equation C.8 has a maximum for $\theta = 0.5$, which explains the occurance of redox-peaks in the CV-diagram, since the derivation done here for surface adsorption can be applied for redox reactions of the form

$$\mathrm{Ox} + e \leftrightharpoons \mathrm{Red}. \qquad \text{(C.9)}$$

Then the Nernst-equation for the equilibrium can be written as

$$E = E^0 + (RT/F)\ln([Ox]/[Red]), \qquad \text{(C.10)}$$

where E^0 is the standard potential of the reaction and [Ox], [Red] the molar mass of the oxidized and reduced species, respectively.

Equation C.8 explains one relatively sharp redox peak in the CV-diagram. The expansion of this theoretical approach was made by Conway and Gileadi, including electronic repulsion in the adsorption process. This was done by introducing an additional energy term $g \cdot \theta$, causing the Langmuir isotherm to change into the Frumkin type [38]:

$$\frac{\theta}{1-\theta} = K\exp(-g\theta) \cdot Kc_{H^+}\exp(EF/RT). \qquad \text{(C.11)}$$

For $g = 0$ the Langmuir case is found. Positive values of g cause the maximum in the CV-diagram to broaden. It is also known, e.g. for Pt(100), even upon careful preparation, several peaks for one adsorption species can arise [21]. This and the very rough surface structure of MnO_2 cause the almost rectangular shape of the CV-diagram for MnO_2, with many redox-peaks overlapping each other (see also Figure 2.2).

Bibliography

[1] Jochen Fricke and Walter L. Borst. *Essentials of Energy Technology: Sources, Transport, Storage, Conservation*. Wiley-VCH, 1st edition, 2013.

[2] Hans-Jürgen Stephan Thomas Litt, Karl-Ernst Behre, Klaus-Dieter Meyer and Stefan Wansa. Stratigraphische Begriffe für das Quartär des norddeutschen Vereisungsgebietes. *E&G – Quaternary Science Journal*, 56(1), 2007.

[3] Ian McDougall, Francis H Brown, and John G Fleagle. Stratigraphic placement and age of modern humans from Kibish, Ethiopia. *Nature*, 433(7027):733–736, 2005.

[4] Ronen Steinke. Wasser bis zum Hals, http://www.sueddeutsche.de/politik/ klimawandel-fluechtlinge-wasser-bis-zum-hals-1.1798599, accessed 8.11.2013.

[5] Thomas Hummitzsch. Climate change and migration : The debate on causality and the legal position of affected persons. *focus Migration, Policy Brief*, (15), 2009.

[6] Nicholas Stern. The Economics of Climate Change - the Stern review: Summary of Conclusions. Technical report, 2007.

[7] David MacKay. *Sustainable energy systems with HVDC transmission*, volume 2. UIT Camebridge Ltd, Camebridge, 1st edition, 2009.

[8] Energie in Deutschland. Trends und Hintergründe zur Energieversorgung. *Bundesministerium für Wirtschaft und Technologie*, 2013.

[9] European Space Agency. Opening doors to space. *ESA - Our Activities*, 2014.

[10] MAN. Lion's City Hybrid http://www.mantruckandbus.com/com/en/Bus_Detail_150720.html, accessed 7.11.2013.

[11] Beverly Braga and Eric Booth. Mazda announces pricing, fuel economy of i-Eloop-equipped 2014 Mazda6. *Mazda North American Operations*, 2013.

[12] Marshall Fenn and Dustin Woods. Press Release Volvo Car Group makes conventional batteries a thing of the past. *Volvo Car Group*, (134659), 2013.

[13] Mathieu Toupin, Thierry Brousse, Daniel Bélanger, and D Belanger. Charge Storage Mechanism of MnO 2 Electrode Used in Aqueous Electrochemical Capacitor. *Chemistry of Materials*, 16(16):3184–3190, 2004.

[14] R. B. Rakhi, W. Chen, D. K. Cha, and H. N. Alshareef. *Nano Letters*, 12:2559, 2012.

[15] Anne E Fischer, Katherine A Pettigrew, Debra R Rolison, Rhonda M Stroud, and Jeffrey W Long. Incorporation of Homogeneous, Nanoscale MnO2 within Ultraporous Carbon Structures via Self-Limiting Electroless Deposition: Implications for Electrochemical Capacitors. *Nano Letters*, 7(2):281–286, 2007.

[16] Anne E. Fischer, Matthew P. Saunders, Katherine A. Pettigrew, Debra R. Rolison, and Jeffrey W. Long. Electroless Deposition of Nanoscale MnO2 on Ultraporous Carbon Nanoarchitectures: Correlation of Evolving Pore-Solid Structure and Electrochemical Performance. *Journal of The Electrochemical Society*, 155(3):A246–A252, 2008.

[17] J. Rouquerol, D. Avnir, C. W. Fairbridge, D. H. Everett, J. M. Haynes, N. Pernicone, J. D. F. Ramsay, K. S. W. Sing, and K. K. Unger. Recommendations for the characterization of porous solids (Technical Report). *Pure and Applied Chemistry*, 66(8):1739–1758, 1994.

[18] John David Jackson. *Classical Electrodynamics, 2nd Edition*. Wiley, 1975.

[19] Carl H. Hamann and Wolf Vielstich. *Elektrochemie (German Edition)*. Wiley, 3. edition, 1998.

[20] B E Conway. *Theory and Principles of Electrode Processes*. Ronald Press Co., New York, 1. edition, 1965.

[21] B. E. Conway. *Electrochemical Supercapacitors: Scientific Fundamentals and Technological Applications*. New York, 1999.

[22] H. Helmholtz. Studien über electrische Grenzschichten. *Annalen der Physik und Chemie*, 243(7):337–382, 1879.

[23] G. Gouy. Constitution of the Electric Charge at the Surface of an Electrolyte. *J. de Phys.*, 4:457, 1910.

[24] D. L. Chapman. A contribution to the theory of electrocapillarity. *Philos. Mag.*, 25:457, 1913.

[25] O Stern. *Zeit. Elektrochem.*, 30:508, 1924.

[26] N.F. Mott and R.J. Watts-Tobin. The interface between a metal and an electrolyte. *Electrochimica Acta*, 4(2-4):79–107, 1961.

[27] K. Muller J.OM. Bockris, M.A.V. Devanathan. On the Structure of Charge Interfaces. *Proceedings of the Royal Society*, A274:55, 1963.

[28] S. Levine, G. M. Bell, and A. L. Smith. *J Phys Chem*, 73:3534, 1969.

[29] N. D. Lang and W Kohn. *Phys. Rev. B*, B1:4555, 1971.

[30] W. Schmickler. No. *J. Electroanal. Chem.*, 176:383, 1984.

[31] S. Amorkane and J.P. Badiali. *J. Electroanal. Chem.*, 266:21, 1989.

[32] J. Chmiola, G. Yushin, Y. Gogotsi, C. Portet, P. Simon, and P. L. Taberna. Anomalous increase in carbon capacitance at pore sizes less than 1 nanometer. *Science*, 313:1760, 2006.

[33] Gregory Salitra, Abraham Soffer, Linoam Eliad, Yair Cohen, and Doron Aurbach. Carbon Electrodes for Double-Layer Capacitors I. Relations Between Ion and Pore Dimensions. *Journal of The Electrochemical Society*, 147(7):2486–2493, 2000.

[34] Volker Lorrmann, Gudrun Reichenauer, Christian Weber, and Jens Pflaum. Electrochemical double-layer charging of ultramicroporous synthetic carbons in aqueous electrolytes. *Electrochimica Acta*, 86:232–240, 2012.

[35] B. E. Conway, V Birss, and J Wojtowicz. The role and utilization of pseudocapacitance for energy storage by supercapacitors. *Journal of Power Sources*, 66:1–14, 1997.

[36] David C Grahame. The Electrical Double Layer and the Theory of Electrocapillarity. *Chemical Reviews*, 41(3):441–501, 1947.

[37] A. Eucken and B. Weblus. *Zeit. Elektrochem.*, 55:114, 1951.

[38] E. Gileadi and B.E. Conway. *J. Chem. Phys.*, 31:716, 1964.

[39] Patrice Simon and Yury Gogotsi. Materials for electrochemical capacitors. *Nature materials*, 7(11):845, 2008.

[40] Kinoshita K. *Carbon: electrochemical and physicochemical properties.* John Wiley & Sons, New York, 1998.

[41] T. Centeno and F. Stoeckli. The role of textural characteristics and oxygen-containing surface groups in the supercapacitor performances of activated carbons. *Electrochimica Acta*, 52(2):560–566, 2006.

[42] E. Raymundopinero, K. Kierzek, J. Machnikowski, and F. Beguin. Relationship between the nanoporous texture of activated carbons and their capacitance properties in different electrolytes. *Carbon*, 44(12):2498–2507, 2006.

[43] Andy Rudge, John Davey, Ian Raistrick, Shimshon Gottesfeld, and John P. Ferraris. Conducting polymers as active materials in electrochemical capacitors. *Journal of Power Sources*, 47(1-2):89–107, 1994.

[44] W. Li, G. Reichenauer, and J. Fricke. Carbon aerogels derived from cresol–resorcinol–formaldehyde for supercapacitors. *Carbon*, 40:2955, 2002.

[45] Masayuki Morita. Advanced Polymers as Active Materials and Electrolytes for Electrochemical Capacitors and Hybrid Capacitor Systems. *Electrochemical Society Interface*, (i), 2008.

[46] Hee Y. Lee and J. B. Goodenough. Supercapacitor Behavior with KCl Electrolyte. *Journal of Solid State Chemistry*, 144(1):220–223, 1999.

[47] Nae-Lih Wu. Nanocrystalline oxide supercapacitors. *Materials Chemistry and Physics*, 75(1-3):6–11, 2002.

[48] P. A. Nelson and J. R. Owen. *Journal of The Electrochemical Society*, 150:1313, 2003.

[49] S. G. Khandalkar, J. L. Gunjalkar, C. D. Lokhande, and O.-S. Joo. Synthesis of Cobalt Oxide Interconnected Flackes and Nano-Worms Structures Using Low Temperature Chemical Bath Deposition. *Journal of Alloys and Compounds*, 478:594, 2009.

[50] Guoping Wang, Lei Zhang, and Jiujun Zhang. A review of electrode materials for electrochemical supercapacitors. *Chemical Society reviews*, 41(2):797–828, 2012.

[51] K Kinoshita and J.A.S Bett. Electrochemical analysis of carbon surface oxides on Teflon-bonded carbon electrodes. *Carbon*, 11(6):682, 1973.

[52] K. S. Ryu, K. M. Kim, N.-G. Park, Y. J. Park, and S. H. Chang. *Journal of Power Sources*, 103:305, 2002.

[53] A. Clemente, S. Panero, E. Spila, and B. Scrosati. *Solid State Ionics*, 85:273, 1996.

[54] A. Laforgue, P. Simon, C. Sarrazin, and J.-F. Fauvarque. *Journal of Power Sources*, 80:142, 1999.

[55] G. Yu, W. Chen, Y. Zheng, J. Zhao, X. Li, and X. Xu. *Materials Letters*, 60:2453, 2006.

[56] Daniel Bélanger, Thierry Brousse, and Jeffrey W. Long. Manganese Oxides : Battery Materials Make the Leap to Electrochemical Capacitors. *Electrochemical Society Interface*, 2008.

[57] Mingjia Zhi, Chengcheng Xiang, Jiangtian Li, Ming Li, and Nianqiang Wu. Nanostructured carbon-metal oxide composite electrodes for supercapacitors: a review. *Nanoscale*, pages 72–88, 2012.

[58] Suh-Cem Pang and Marc a Anderson. Novel electrode materials for electrochemical capacitors: Part II. Material characterization of sol-gel-derived and electrodeposited manganese dioxide thin films. *Journal of Materials Research*, 15(10):2096–2106, 2000.

[59] Suk-Fun Chin, Suh-Cem Pang, and Marc A. Anderson. Material and Electrochemical Characterization of Tetrapropylammonium Manganese Oxide Thin Films as Novel Electrode Materials for Electrochemical Capacitors. *Journal of The Electrochemical Society*, 149(4):A379, 2002.

[60] Wesley M. Dose and Scott W. Donne. Thermal Treatment Effects on Manganese Dioxide Structure, Morphology and Electrochemical Performance. *Journal of The Electrochemical Society*, 158(8):A905, 2011.

[61] Shin-Liang Kuo and Nae-Lih Wu. Investigation of Pseudocapacitive Charge-Storage Reaction of MnO 2nH2O Supercapacitors in Aqueous Electrolytes. *Journal of The Electrochemical Society*, 153(7):A1317, 2006.

[62] Thierry Brousse, Pierre-louis Taberna, Olivier Crosnier, Romain Dugas, Philippe Guillemet, Yves Scudeller, Yingke Zhou, and Patrice Simon. Long-term cycling behavior of asymmetric activated carbon/MnO 2 aqueous electrochemical supercapacitor. *Journal of Power Sources*, 173:633–641, 2007.

[63] Alexander J. Roberts and Robert C.T. Slade. Effect of specific surface area on capacitance in asymmetric carbon/α-MnO2 supercapacitors. *Electrochimica Acta*, 55(25):7460–7469, 2010.

[64] L. Demarconnay, E. Raymundo-Piñero, and F. Béguin. Adjustment of electrodes potential window in an asymmetric carbon/MnO2 supercapacitor. *Journal of Power Sources*, 196(1):580–586, 2011.

[65] Suh-Cem Pang, Marc a. Anderson, and Thomas W. Chapman. Novel Electrode Materials for Thin-Film Ultracapacitors: Comparison of Electrochemical Properties of Sol-Gel-Derived and Electrodeposited Manganese Dioxide. *Journal of The Electrochemical Society*, 147(2):444, 2000.

[66] Mao-Sung Wu, Zong-Sin Guo, and Jiin-Jiang Jow. Highly Regulated Electrodeposition of Needle-Like Manganese Oxide Nanofibers on Carbon Fiber Fabric for Electrochemical Capacitors. *The Journal of Physical Chemistry C*, 114(49):21861–21867, 2010.

[67] N. Nagarajan, H. Humadi, and I. Zhitomirsky. Cathodic electrodeposition of MnOx films for electrochemical supercapacitors. *Electrochimica Acta*, 51(15):3039–3045, 2006.

[68] S. Devaraj and N. Munichandraiah. The Effect of Nonionic Surfactant Triton X-100 during Electrochemical Deposition of MnO2 on Its Capacitance Properties. *Journal of The Electrochemical Society*, 154(10):A901–A909, 2007.

[69] Jun Yan, Zhuangjun Fan, Tong Wei, Weizhong Qian, Milin Zhang, and Fei Wei. Fast and reversible surface redox reaction of graphene–MnO2 composites as supercapacitor electrodes. *Carbon*, 48(13):3825–3833, 2010.

[70] Sheng Chen, Junwu Zhu, Huajie Huang, Guiyu Zeng, Fude Nie, and Xin Wang. Facile solvothermal synthesis of graphene–MnOOH nanocomposites. *Journal of Solid State Chemistry*, 183(11):2552–2557, 2010.

[71] Mingjia Zhi, Ayyakkannu Manivannan, Fanke Meng, and Nianqiang Wu. Highly conductive electrospun carbon nanofiber/MnO2 coaxial nano-cables for high energy and power density supercapacitors. *Journal of Power Sources*, 208:345–353, 2012.

[72] Wei Chen, Zhongli Fan, Lin Gu, Xinhe Bao, and Chunlei Wang. Enhanced capacitance of manganese oxide via confinement inside carbon nanotubes. *Chemical communications (Cambridge, England)*, 46(22):3905–7, 2010.

[73] Hui Xia, Yu Wang, Jianyi Lin, and Li Lu. Hydrothermal synthesis of MnO2/CNT nanocomposite with a CNT core/porous MnO2 sheath hierarchy architecture for supercapacitors. *Nanoscale Research Letters*, 7(1):33, 2012.

[74] Fangyi Cheng, Jianzhi Zhao, Wene Song, Chunsheng Li, Hua Ma, Jun Chen, and Panwen Shen. Facile controlled synthesis of MnO2 nanostructures of novel shapes and their application in batteries. *Inorganic chemistry*, 45(5):2038–44, 2006.

[75] Weifeng Wei, Xinwei Cui, Weixing Chen, and Douglas G. Ivey. Manganese oxide-based materials as electrochemical supercapacitor electrodes. *Chemical Society reviews*, 40(3):1697–721, 2011.

[76] Dengyun Zhai, Baohua Li, Chengjun Xu, Hongda Du, Yanbing He, Chunguang Wei, and Feiyu Kang. A study on charge storage mechanism of a-MnO2 by occupying tunnels with metal cations (Ba2+, K+). *Journal of Power Sources*, 196(18):7860–7867, 2011.

[77] H. Pröbstle, M. Wiener, and J. Fricke. Carbon Aerogels for Electrochemical Double Layer Capacitors. *Journal of Porous Materials*, 10:213, 2003.

[78] R. W. Pekala. Low Density, Resorcinol-Formaldehyde Aerogels, US Patent No. 4997804, 1991.

[79] D. H. Everett, R. A. W. Haul, L. Moscou, R. A. Pierotti, J. Rouquerol, and T. Siemieniewska. Reporting Pysisorption Data for Gas/Solid Systems with Special Reference to the Determination of Surface Area and Porosity. *Pure Appl. Chem.*, 57:603, 1985.

[80] R. W. Pekala, C. T. Alviso, X. Lu, J. Gross, and J. Fricke. New organic aerogels based upon a phenolic-furfural reaction. *Journal of Non-Crystalline Solids*, 188:34, 1995.

[81] R. W. Pekala. Melanine-formaldehyde aerogels, US Patent No. 5086085, 1992.

[82] R. W. Pekala. Organic aerogels from the polycondensation of resorcinol with formaldehyde. *Journal of Materials Science*, 24:3221, 1989.

[83] R. Saliger, V. Bock, R. Petricevic, T. Tillotson, S. Geis, and J. Fricke. Carbon aerogels from dilute catalysis of resorcinol with formaldehyde. *Journal of Non-Crystalline Solids*, 221:144, 1997.

[84] M. Wiener, G. Reichenauer, T. Scherb, and J. Fricke. Accelerating the synthesis of carbon aerogel precursors. *Journal of Non-Crystalline Solids*, 350:126–130, 2004.

[85] Mitsuhiro Hibino, Hirokazu Kawaoka, Haoshen Zhou, and Itaru Honma. Two-step addition of acetylene black to hydrated sodium manganese oxide: its effect on the performance of rapid discharge cathode. *Journal of Power Sources*, 124(1):143–147, 2003.

[86] M Hibino, H Kawaoka, H Zhou, and I Honma. Rapid discharge performance of composite electrode of hydrated sodium manganese oxide and acetylene black. *Electrochimica Acta*, 49(28):5209–5216, 2004.

[87] Hirokazu Kawaoka, Mitsuhiro Hibino, Haoshen Zhou, and Itaru Honma. Sonochemical synthesis of amorphous manganese oxide coated on carbon and application to high power battery. *Journal of Power Sources*, 125(1):85–89, 2004.

[88] H. Kawaoka, M. Hibino, H. Zhou, and I. Honma. Nanostructure and high-rate discharge-charge property of manganese oxide/acetylene black nanocomposite synthesized by sonochemical method. *Solid State Ionics*, 176(5-6):621–627, 2005.

[89] D. Wu, R. Fu, and Z. Yu. Organic and Carbon Aerogels from the NaOH-Catalyzed Polycondensation of Resorcinol–Furfural and Supercritical Drying in Ethanol. *J. Appl. Polym. Sci.*, 96:698, 2004.

[90] Sang-Bok Ma, Young-Ho Lee, Kyun-Young Ahn, Chi-Myung Kim, Ki-Hwan Oh, and Kwang-Bum Kim. Spontaneously Deposited Manganese Oxide on Acetylene Black in an Aqueous Potassium Permanganate Solution. *Journal of The Electrochemical Society*, 153(1):C27, 2006.

[91] Hans Darmstadt and Christian Roy. Surface spectroscopic study of basic sites on carbon blacks. *Carbon*, 41(13):2662–2665, 2003.

[92] T.J. Fabish and D.E. Schleifer. Surface chemistry and the carbon black work function. *Carbon*, 22(1):19–38, 1984.

[93] Gudrun Reichenauer. Structural Characterization of Aerogels, in Aerogels Handbook. chapter Structural, pages 449–498. Springer Science+Business Media, New York, 1. edition, 2011.

[94] J. Goldstein. *Scanning Electron Microscopy and X-ray Microanalysis*, volume 44. Springer, 2003.

[95] F. Schüth, K. S. W. Sing, and J. Weitkamp, editors. *Handbook of Porous Solids*. Weinheim, band 1 edition, 2002.

[96] Daniel Abou-Ras, Thomas Kirchartz, and Uwe Rau, editors. *Advanced Characterization Techniques for Thin Film Solar Cells*. Wiley-VCH, Weinheim, 1. edition, 2011.

[97] P.A. Webb and C. Orr. *Analytical Methods in Fine Particle Technology*. Micromeritics Instrument Corp., 1997.

[98] G. Reichenauer, C. Stumpf, and J. Fricke. Characterization of SiO2, RF and carbon aerogels by dynamic gas expansion. *Journal of Non-Crystalline Solids*, 186:334–341, 1995.

[99] S. Brunauer, P. H. Emmett, and E. Teller. *J. Am. Chem. Soc.*, 60:309, 1938.

[100] S.J. Gregg and K.S.W. Sing. *Adsorption, Surface Area and Porosity*. London, second ed. edition, 1982.

[101] B. C. Lippens and J. H. de Boer. Studies on pore systems in catalysts : V. The t method. *J. Catal.*, 4(319), 1965.

[102] B. C. Lippens, B. G. Linsen, and J. H. D. E. Boer. Studies The Adsorption on Pore Systems in Catalysts and Calculation of Nitrogen ; Apparatus FOR MEASURING NITROGEK. 37:32–37, 1964.

[103] W. D. Harkins and G. Jura. Surfaces of Solids. XII. An Absolute Method for the Determination of the Area of a Finely Divided Crystalline Solid. *J. Amer. Chem. Soc.*, 66:1362, 1944.

[104] John R. Taylor. *Introduction to Error Analysis*. University Science Books, Sausalito, CA, 1st edition, 1997.

[105] H. Hertz. Ueber einen Einfluss des ultravioletten Lichtes auf die electrische Entladung. *Annalen der Physik*, 267(8):983–1000, 1887.

[106] A. Einstein. Über einen die Erzeugung und Verwandlung des Lichtes betreffenden heuristischen Gesichtspunkt. *Annalen der Physik*, 322(6):132–148, 1905.

[107] Thomas Moller. *Forschung mit Synchrotronstrahlung: Eine Einführung in die Grundlagen und Anwendungen (German Edition)*. Vieweg+Teubner Verlag, 2010.

[108] Wolfgang Demtröder. Experimentalphysik 3: Atome, Moleküle und Festkörper. *Moleküle und Festkörper Springer Verlag*, 3:1–647, 2010.

[109] F. Schwabel. *Quantenmechanik*. Springer, Berlin, 2004.

[110] G. Goerigk, H.G. Haubold, and O.Lyon. *J. Appl. Crystallogr.*, 36:425, 2003.

[111] Ulla Vainio. Characterisation of cellulose-and lignin-based materials using x-ray scattering methods. *PhD Thesis, University of Helsinki, Finnland*, 2007.

[112] C. Scherdel, T. Scherb, and G. Reichenauer. Spherical porous carbon particles derived from suspensions and sediments of resorcinol-formaldehyde particles. *Carbon*, 47(9):2244–2252, 2009.

[113] C. Scherdel and G. Reichenauer. The impact of residual adsorbate on the characterization of microporous carbons with small angle scattering. *Carbon*, 50(8):3074–3082, 2012.

[114] Claudine E Williams and Roland P May. Small-Angle Scattering of X-Rays and Neutrons. In Eric Lifshin, editor, *X-ray Characterization of Materials*, chapter 4. Wiley-VCH, Weinheim, 1st edition, 1999.

[115] O. Glatter and O. Kratky. *Small angle X-ray scattering*. Academic Press Inc. Ltd., London, 1. edition, 1982.

[116] Dragomir Tatchev. Structure analysis of multiphase systems by anomalous small-angle X-ray scattering. *Philosophical Magazine*, 88(12):1751–1772, 2008.

[117] C.T. Chantler. X-Ray Form Factor, Attenuation and Scattering Tables (version 2.1). *J. Phys. Chem. Ref. Data*, 29(4):597–1048, 2000.

[118] Don T. Cromer. Relativistic Calculation of Anomalous Scattering Factors for X Rays. *The Journal of Chemical Physics*, 53(5):1891, 1970.

[119] DT Cromer and DA Liberman. Anomalous dispersion calculations near to and on the long-wavelength side of an absorption edge. *Acta Crystallographica Section A: Crystal ...*, pages 267–268, 1981.

[120] G. Materlik, C.J. Sparks, and K. Fischer. *Resonant Anomalous X-Ray Scattering: Theory and Applications*. North Holland, 1 edition, 1994.

[121] P. A. Doyle and P. S. Turner. *Acta Crystallographica*, 24:390, 1968.

[122] D. Waasmaier and a. Kirfel. New analytical scattering-factor functions for free atoms and ions. *Acta Crystallographica Section A Foundations of Crystallography*, 51(3):416–431, 1995.

[123] P. J. Brown, A. G. Fox, E. N. Maslen, M. A. O'Keefe, and B. T. M. Willis. Intensity of diffracted intensities. *International Tables for Crystallography*, C:554, 2006.

[124] G. Goerigk, R. Schweins, K. Huber, and M. Ballauff. The distribution of Sr 2+ counterions around polyacrylate chains analyzed by anomalous small-angle X-ray scattering. *Europhysics Letters (EPL)*, 66(3):331–337, 2004.

[125] G. Goerigk, K. Huber, and R. Schweins. Probing the extent of the Sr2+ ion condensation to anionic polyacrylate coils: a quantitative anomalous small-angle x-ray scattering study. *The Journal of chemical physics*, 127(15):154908, 2007.

[126] Robert A. Scott and Charles M. Lukehart. *Applications of Physical Methods to Inorganic and Bioinorganic Chemistry*. John Wiley \& Sons, Ltd, 2 edition, 2007.

[127] Research Solutions & Resources LLC. The Ag/AgCl Reference Electrode. *consultrsr*, 2014.

[128] V. Vivier, B. L. Wu, C. S. Cha, and L. T. Yu. Cavity Microelectrode for Studying Powder Materials at a High Potential Scan Rate. *Electrochemical and Solid-State Letters*, 2(8):385–387, 1999.

[129] M.E. Orazem and Bernard Tribollet. *Electrochemical impedance spectroscopy*. John Wiley & Sons, New Jersey, 1 edition, 2008.

[130] A.J. Bard and L.R. Faulkner. *Electrochemical methods: fundamentals and applications*. John Wiley & Sons, New York, 2nd edition, 1980.

[131] R. DeLevie. On porous electrodes in electrolyte solutions. *Electrochimica Acta*, 8:751, 1964.

[132] Kenneth S. Cole and Robert H. Cole. Dispersion and Absorption in Dielectrics I. Alternating Current Characteristics. *The Journal of Chemical Physics*, 9(4):341, 1941.

[133] PL L. Taberna, P. Simon, and J. F. JF Fauvarque. Electrochemical Characteristics and Impedance Spectroscopy Studies of Carbon-Carbon Supercapacitors. *Journal of The Electrochemical Society*, 150(3):A292, 2003.

[134] John Miller. In *Proceedings of the 8th International Seminar on Double-Layor Capacitors and Similar Energy Storage Devices*, Deerfield Beach, FL, 1998.

[135] Christian Weber. Entwicklung elektrochemischer Energiespeicher Kompositelektroden auf Basis von Kohlenstoffaerogelen und Manganoxid. *Julius-Maximilians Universität Würzburg*, 2009.

[136] Xingkang Huang, Dongping Lv, Hongjun Yue, Adel Attia, and Yong Yang. Controllable synthesis of α- and β-MnO(2): cationic effect on hydrothermal crystallization. *Nanotechnology*, 19(22):225606–225606, 2008.

[137] Madelung (ed.) M., Rössler O., and Schulz U. *Non-Tetrahedrally Bonded Binary Compounds II*, volume 41D of *Landolt-Börnstein - Group III Condensed Matter*. Springer-Verlag, Berlin/Heidelberg, 2000.

[138] Hirofumi Kanoh, Weiping Tang, Yoji Makita, and Kenta Ooi. Electrochemical Intercalation of Alkali-Metal Ions into Birnessite-Type Manganese Oxide in Aqueous Solution. *Langmuir*, 13(25):6845–6849, 1997.

[139] Ph. Guillemet, Th. Brousse, O. Crosnier, Y. Dandeville, L. Athouel, and Y. Scudeller. Modeling pseudo capacitance of manganese dioxide. *Electrochimica Acta*, 67:41–49, 2012.

[140] B.E. Conway, J. OM. Bockris, and Ralph E. White, editors. *Modern Aspects of Electrochemistry*. Kluwer Academic Publishers, New York, 1 edition, 2002.

[141] Christian Weber, Gudrun Reichenauer, and Jens Pflaum. Electroless Preparation and ASAXS Microstructural Analysis of Pseudocapacitive Carbon Manganese Oxide Supercapacitor Electrodes. *Langmuir*, 2(31):782–788, 2015.

[142] E. Beaudrouet, A. Legallasalle, and D. Guyomard. Nanostructured manganese dioxides: Synthesis and properties as supercapacitor electrode materials. *Electrochimica Acta*, 54(4):1240–1248, 2009.

[143] Christian Weber, Volker Lorrmann, Gudrun Reichenauer, and Jens Pflaum. Structural and electrochemical properties of MnO2-Carbon based supercapacitor electrodes. *arXiv:1411.6278*, 2014.

[144] Ariana Cormie, Andrew Cross, Anthony. F. Hollenkamp, and Scott W. Donne. Cycle stability of birnessite manganese dioxide for electrochemical capacitors. *Electrochimica Acta*, 55(25):7470–7478, 2010.

[145] Matthias Wiener. *Synthese und Charakterisierung Sol-Gel- basierter Kohlenstoff-Materialien für die*. PhD thesis, Bayerische Julius-Maximilians Universität, Würzburg, 2009.

[146] J. Li, X. Wang, Q. Huang, S. Gamboa, and P. J. Sebastian. Studies on preparation and performances of carbon aerogel electrodes for the application of supercapacitor. *J. Power Sources*, 158:784, 2006.

[147] J. E. Post and D. R. Veblen. Crystal structure determinations of synthetic sodium, magnesium and potassium birnessite using TEM and the Rietveld method. *American Minderalogist*, 75:477–489, 1990.

[148] W. Kraus and G. Nolze. Powder Cell for Windows, 1999.

[149] Qing Lu and Yikai Zhou. Synthesis of mesoporous polythiophene/MnO2 nanocomposite and its enhanced pseudocapacitive properties. *Journal of Power Sources*, 196(8):4088–4094, 2011.

[150] Zhaoping Liu, Renzhi Ma, Yasuo Ebina, Kazunori Takada, and Takayoshi Sasaki. Synthesis and Delamination of Layered Manganese Oxide Nanobelts. *Chemistry of Materials*, 19(26):6504–6512, 2007.

[151] John W. Anthony, Richard A. Bideaux, Kenneth W. Bladh, and Monte C. Nichols. *Handbook of Mineralogy*. Mineral Data Publishing, Tucson Arizona, USA, 1990.

[152] Ouassim Ghodbane, Jean-Louis Pascal, and Frédéric Favier. Microstructural effects on charge-storage properties in MnO2-based electrochemical supercapacitors. *ACS applied materials & interfaces*, 1(5):1130–9, 2009.

[153] J. J. Yeh and I. Lindau. Atomic subshell photoionization cross sections and asymmetry parameters. *Atomic data and nuclear data tables*, 32:1–155, 1985.

[154] John F. Moulder, William F. Stickle, Peter E. Sobol, and Kenneth D. Bomben. *Handbook of X-ray Spectroscopy*. Perkin-Elmer, Minnesota, 1992.

[155] R. Iwanowski. X-ray photoelectron spectra of zinc-blende MnTe. *Chemical Physics Letters*, 387(1-3):110–115, 2004.

[156] Masaoki Oku, Hideyuki Matsuta, Kazuaki Wagatsuma, and Tokuzo Konishi. Simple correlation between Mn-Ka X-ray emission and Mn 2p X-ray photoelectron spectra for high oxidation number or low-spin manganese compounds. *Journal of the Chemical Society, Faraday Transactions*, 92(15):2759–2764, 1996.

[157] D. Das, P. Sen, and K. Das. Mechanism of potentiostatic deposition of MnO2 and electrochemical characteristics of the deposit in relation to carbohydrate oxidation. *Electrochimica Acta*, 54(2):289–295, 2008.

[158] Gao-Ren Li, Zhan-Ping Feng, Yan-Nan Ou, Dingcai Wu, Ruowen Fu, and Ye-Xiang Tong. Mesoporous MnO2/carbon aerogel composites as promising electrode materials for high-performance supercapacitors. *Langmuir : the ACS journal of surfaces and colloids*, 26(4):2209–13, 2010.

[159] O. Kratky and G. Porod. Diffuse small-angle scattering of X-rays in colloid systems. *Journal Of Colloid Science*, 4(1):35–70, 1949.

[160] H. Tobias and A. Soffer. The immersion potential of high surface electrodes. *Journal of Electroanalytical Chemistry and Interfacial Electrochemistry*, 148(2):221–232, 1983.

[161] Volker Lorrmann. *Electrochemical Characterization of Resorcinol-Formaldehyde derived Carbon Xerogels*. PhD thesis, Julius-Maximilians Universität Würzburg, 2013.

[162] S.W. Donne, A.F. Hollenkamp, and B.C. Jones. Structure, morphology and electrochemical behaviour of manganese oxides prepared by controlled decomposition of permanganate. *Journal of Power Sources*, 195(1):367–373, 2010.

Acknowledgements

Ich möchte mich bei Prof. Dr. Jens Pflaum für die Möglichkeit bedanken, die Dissertation am Lehrstuhl für experimentelle Physik VI durchzuführen. Darüber hinaus gab es natürlich noch eine ganze Liste an Leuten, die mich bei der Durchführung meiner Arbeiten unterstützt haben und bei denen ich mich hiermit recht herzlich bedanken möchte:

- Bei Dr. Gudrun Reichenauer, meiner wissenschaftlichen Betreuerin während der Arbeit, für endlose Diskussionen und geduldige Erklärungen, die stets neue fruchtbare Impulse für den Fortgang der Arbeit geliefert haben.
- Bei Prof. Dr. Geurts für die interessierte Begutachtung dieser Arbeit.
- En stor takk også til Michael Sørensen, min nye sjef i Transportøkonomisk Institutt, som ga meg frihet og støtte til å avslutte doktorgraden.
- Weiterhin möchte ich mich bei der Deutsche Bundesstiftung Umwelt für das Promotionsstipendium bedanken. Ohne diese Finanzierung hätte die Arbeit nicht durchgeführt werden können. Vielen Dank auch für die interessanten Seminare, bei denen sich Einblicke und spannende Diskussionen mit Doktoranden anderer Fachrichtungen ergeben haben.
- Bei Volker Lorrmann, für stets sehr gute Zusammenarbeit, für die Einführung in elektrochemische Messmethoden und nicht zuletzt in die Programmiersprache Python, die so vieles einfacher gemacht hat.
- An dieser Stelle dann auch noch gleich ein Dank an Jens Lorrmann, der mir bei später entstandenen Python-Fragen hilfreich zur Seite stand!
- Besonderer Dank gilt auch Dr. Matthias Wiener, Dr. Stephan Braxmeier und Christian Blazer für die Hilfe mit den ASAP-Messungen, tiefgehende Diskussionen um unkonventionelle Lösungen und ein stets gutes Arbeitsklima.
- Ebenfalls besonderer Dank an Dr. Christian Scherdel, für spannende SAXS-Marathon-Messungen am DESY und gute Tipps für kulinarische Highlights in HH.
- Dr. Ulla Vainio, für zahlreiche Hilfestellungen bei ASAXS-Fragen.
- Sebastian Meyer am Lehrstuhl für Experimentelle Physik IV für die Hilfe mit den XPS Messungen.
- Franziska Fuchs, meiner rechten Hand in Deutschland, für das Ausdrucken und Abgeben der Arbeit.
- Björn für die gute Büronachbarschaft und diversen Ohrenschmaus über die gesamte Zeit.
- Dem Rest der wechselnden Belegschaft von E011 für allzeit gute Unterhaltung und natürlich der gesamten Arbeitsgruppe der EP6 für ein stets kollegiales Arbeitsklima.
- Den “Jungs” für eine wirklich phantastische Studienzeit, Urlaube, Kneipenabende, endlose Stammtischdiskussionen mit munter wechselnden Fronten...
- Meiner Familie, die mir ermöglicht hat alles zu erreichen was ich mir in den Kopf gesetzt habe und mir immer den Rücken frei gehalten hat.
- Und schließlich Hanne, die mich immer unterstützt und manchmal auch angetrieben hat, wenn es mal nicht wie geplant voran ging. Ich freue mich auf unser Leben in Norwegen!